

Scattering from Stratified Media with a Rough Surface: Application to Sea Ice Ridges

by

©Pradeep Bobby

A Dissertation submitted to the School of Graduate Studies in partial fulfillment of
the requirements for the degree of

Ph.D.

Faculty of Engineering and Applied Science

Memorial University of Newfoundland

April 2020

St. John's

Newfoundland

Abstract

Sea ice ridging is the dominant factor contributing to sea ice thickness, which has impacts on climate change and transportation. It is important to know the age of sea ice ridges, since ice age affects the strength of the ice and its ability to persist through the summer melt season. However, information on the age of sea ice ridges is not commonly available. The goal of this thesis is to develop a method to distinguish between first year and multi-year sea ice ridges using simulations of scattering signatures in the range 100-500 MHz. This goal is achieved by modifying existing scattering models, developing a sea ice model and comparing simulation results.

The research is based on Walsh's scattering approach, which was originally developed to model high frequency (HF) radar propagation across a rough surface or through stratified media and three updates to the scattering model are made. In the first update, Walsh's method is modified from assuming the surface is a good conductor to be applicable to scattering from general dielectrics. Secondly, Walsh used a simplified scattering geometry, which implicitly assumed small surface slopes. By using the correct scattering geometry the method is extended to general surface slopes. The vertical component of the electric field is the most important for propagation across the surface, but the horizontal components of the field are relevant for penetration through the surface. The third update to the model is the derivation of the x -component of the electric field.

Sea ice ridges are modeled as having a rough surface over stratified media. The total scatter is the sum of the surface and subsurface scatter. The subsurface scatter is a function of the field transmitted through the surface, the scatter from the layers and the transmission up through the underside of the rough surface. The subsurface scatter is found by considering all the scattering events in terms of scattering coefficients.

The field transmitted down through the rough surface is found using a novel application of the boundary conditions at the surface. Due to the overlying rough surface, the scatter from the layers may be simplified to have the same structure as the Fresnel reflection coefficients for parallel and perpendicular radiation. Determining the field transmitted up through the underside of the surface may be found in a similar way as the first transmitted field, except that the underside of the surface has an inverted shape requiring that the rough surface scattering equations be rederived.

To this point in the research sea ice ridges have been described in a general manner as having a rough surface over stratified media. To justify this approach and provide sufficient details for comparing scattering behaviour, a model describing the structure and internal characteristics of sea ice ridges is developed. The objective is not to fully describe sea ice ridges, but to include the factors that contribute to scattering in the frequency range from 100–500 MHz. Both first year and multi-year ridges have three layers consisting of the top of sail, remainder of sail and consolidated layer.

Due to the lossy nature of sea ice, the salinity in the top layer of the ice dominates the scattering behaviour, but changes in the density, porosity and temperature of the ice also impact the scattered field. Since the ridge surface is assumed to have a sinusoidal profile with a long correlation length with respect to the radar wavelength, the surface and subsurface scatter may be separated spatially. However, simulations based on the characteristics of first year and multi-year ridges indicate that the to-

tal scatter is greater for multi-year ridges due to the subsurface contribution. This suggests that it should be possible to discriminate between first year and multi-year ridges for realistic surface geometries.

Acknowledgements

My inspiration to return to school at 38 years of age came from two sources. The first was a field survey of an ice island off the coast of Labrador where we collected ground penetrating radar and seismic data. Years later I am still fascinated by the squiggles of the data and the information they hold. The second motivating factor was a misremembered line from Salinger's *The Catcher in the Rye*. I thought the text said "The point of an education is...to let you know how big your mind is, and what kind of ideas it can take on." I started a PhD, not because I wanted to learn something, but because I wanted to know what I could learn, what I could contribute. From these ambiguous origins I am surprised to be concluding four years of research, with the help and support of numerous people and groups along the way.

First and foremost I would like to thank my supervisor, Dr. Eric W. Gill, for his constant support and encouragement. Without his guidance this thesis would not exist since I would have given up in my first year. Dr. Gill has been a great sounding board and let me figure out things for myself, which has helped me move closer towards my goal of becoming an independent researcher. I would like to thank my supervisory committee, which include Dr. Reza Shahidi and Dr. Igor Zakharov, who reviewed my papers and asked me the right kinds of questions. I would also like to thank Dr. Gill and Dr. Moloney for writing glowing recommendation letters that led to me being very well-funded for most of my degree. Even though I did not read

those letters it is good to know that people believed in me enough to think I deserved those awards. I would like to thank the radar research group at Memorial University for providing a forum in which I could receive feedback in a non-threatening way and discuss my work with mentors and peers.

I have received funding support from Memorial University, RDC (now InnovateNL) and NSERC. By the grace of God my funding support has been generous and has allowed me to focus exclusively on my studies without the distractions of part-time work or teaching assistantships.

I am grateful to C-CORE for granting me a leave of absence, which provided me a quiet place to do my work and parking on campus. Although it seems trivial, I would like to thank my running and gym buddies at C-CORE, ANE and Goodlife Fitness. It was great starting off the day or taking a break in the middle of the day being active with people who had a positive attitude. Several times following a fitness break, something I had been struggling with for days or weeks became clear.

Finally, I would like to thank my family. My parents have always supported and encouraged me even if they didn't understand why I would give up a job I liked to go back to school. My children are too young to remember a time when I wasn't in school and I am blessed to have them in my life for the joy they bring. My wife, Rebecca, always knew I would go back to school and she tolerated my work in the evenings, missed family trips and high stress levels. She also bore the burden of most of the school pick ups, after school activities and birthday parties. This journey has been worthwhile, but we are all looking forward to the next stage of life.

Table of Contents

Abstract	ii
Acknowledgments	v
List of Tables	xiii
List of Figures	xvi
List of Abbreviations	xvii
List of Symbols	xix
1 Introduction	1
1.1 Context and Motivation	1
1.2 Aim and Goals of the Research	4
1.3 Literature Review	5
1.3.1 Sea Ice Remote Sensing using EM Energy	5
1.3.2 Sea Ice Deformation	11
1.3.3 Rough Surface and Stratified Media Scattering	14
1.3.4 Walsh Scattering Approach	17
1.4 Research Contributions of Thesis	32
1.5 Contributions to the Literature	35

2	Generalizing Scattering Models for Rough Surfaces	36
2.1	Introduction	36
2.2	Scatter from a Rough Surface with General Permittivity	38
2.3	Removing the Small Slope Assumption	43
2.4	Deriving the x -Component of the Scattered Field	48
2.5	Summary	52
3	Modeling scatter from sea ice ridges represented as rough surfaces above stratified media	53
3.1	Introduction	53
3.2	Ridges as Rough Surfaces	54
3.2.1	Roughness Criteria	54
3.2.2	Sea Ice Ridge Roughness	56
3.3	Ridges as Stratified Media	58
3.4	Analysis Overview	61
3.5	Direct-Surface Scatter	63
3.6	Transmission Down through the Rough Surface	64
3.7	Scatter from Stratified Media	71
3.8	Scatter from the Underside of the Rough Surface	74
3.9	Transmission Upward Through Underside of Rough Surface	80
3.9.1	Combining Modes of Electric Field	80
3.9.2	Total Polarized Field	81
3.10	Possible Extensions	83
3.11	Summary	86
4	Modeling Sea Ice Ridges for Scattering at VHF	88
4.1	Introduction	88

4.2	Overview of Sea Ice Properties	90
4.2.1	Salinity	90
4.2.2	Density	92
4.2.3	Micro-porosity	94
4.2.4	Temperature	95
4.3	Sea Ice Ridge Structure	96
4.3.1	Sail	97
4.3.2	Consolidated Layer	101
4.3.3	Keel - Unconsolidated Rubble	104
4.4	Profile Measurements	106
4.4.1	FY Ridge Values	109
4.4.2	MY Ridge Values	110
4.5	Modeling Electrical Parameters	112
4.5.1	Pure Ice Parameters	113
4.5.2	Brine Parameters	113
4.5.3	Sea Water Parameters	116
4.5.4	Proportions of Sea ice Components	117
4.5.5	Mixture Model	119
4.5.6	Field Attenuation	121
4.5.7	Isotropy	122
4.5.8	Volume Scatter	122
4.5.9	Snow Cover	123
4.6	Sea Ice Ridge Models	124
4.7	Conclusions	126
5	Scattering Simulations for First Year and Multi-Year Ridges	129
5.1	Introduction	129

5.2	Simulations based on Variations of a Single Sea Ice Parameter	131
5.2.1	Impact of Salinity	131
5.2.2	Impact of Thickness	133
5.2.3	Impact of Temperature	134
5.2.4	Impact of Density	135
5.3	Simulations based on Variations of a Single Parameter of the Source and Surface	137
5.3.1	Impact of EM Frequency	137
5.3.2	Impact of Roughness Height	138
5.3.3	Impact of Roughness Scale	140
5.4	Simulations based on Variations of Ridge-Specific Parameters	141
5.4.1	Impact of FY Sail Macro-porosity	142
5.4.2	Impact of Top of MY Sail Thickness	142
5.5	Scattering Simulations of FY and MY Ridges over Ice Season	145
5.6	Factors that Affect Discrimination of FY and MY Ridges	147
5.6.1	Top of Sail Salinity	148
5.6.2	Top of Sail Density	148
5.6.3	Other Parameters	148
5.7	Summary and Conclusions	149
6	Conclusions	152
6.1	Summary	152
6.2	Limitations and Assumptions	154
6.2.1	Assumptions on Sea Ice Models	155
6.2.2	Assumptions on Scattering Mechanisms	156
6.2.3	Assumptions on Scattering Model	157
6.3	Future Directions	158

Appendices	160
A Bandlimited Fields and Gently Varying Surfaces	161
B Stratified Media Scattering Coefficients	165

List of Tables

4.1	Ice topography, summarized from [1]	98
4.2	Morphology of first year ridges, taken from [2]	98
4.3	Consolidation of FY ridge, from [3]. Standard deviations provided in parentheses where available	99
4.4	Summary of FY ridge density measurements	109
4.5	Summary of FY ridge salinity measurements	109
4.6	Summary of FY ridge porosity measurements	110
4.7	Summary of FY ridge temperature measurements	110
4.8	Summary of MY ridge density measurements	111
4.9	Summary of MY ridge salinity measurements	111
4.10	Summary of MY ridge temperature measurements	112
4.11	Summary of FY ridge characteristics	126
4.12	Summary of MY ridge characteristics	127
5.1	Parameters used for testing impact of sea ice salinity on scattering . .	133
5.2	Simulations showing impact of sea ice salinity on scattered field . . .	133
5.3	Parameters used for testing impact of sea ice thickness on scattering .	134
5.4	Simulations showing impact of sea ice thickness on scattered field (S = 0.25‰)	135

5.5	Simulations showing impact of sea ice thickness on scattered field ($S = 2\text{‰}$)	135
5.6	Parameters used for testing impact of sea ice temperature on scattering	136
5.7	Simulations showing impact of sea ice temperature on scattered field .	136
5.8	Parameters used for testing impact of sea ice density on scattering . .	137
5.9	Simulations showing impact of sea ice density on scattered field . . .	137
5.10	Parameters used for testing impact of EM frequency on scattering . .	138
5.11	Impact of EM frequency on scattered field, for $S = 0.25\text{‰}$, $t = 3$ m .	138
5.12	Impact of EM Frequency on scattered field, for $S = 2\text{‰}$, $t = 0.5$ m .	139
5.13	Parameters used for testing impact of roughness height on scattering	139
5.14	Impact of surface roughness height on scattered field, for $S = 0.25\text{‰}$	140
5.15	Parameters used for testing impact of rough surface wavelength on scattering	141
5.16	Impact of rough surface wavelength on scattered field, $S = 0.25\text{‰}$. .	141
5.17	Parameters for testing impact of FY sail macro-porosity	143
5.18	Impact of FY ridge macro-porosity on scattered field	143
5.19	Summary of MY ridge characteristics	144
5.20	Impact of height of porous layer of MY ridge on scattered field	144
5.21	Nominal FY ridge characteristics used for simulations	145
5.22	Nominal MY ridge characteristics used for simulations	146
5.23	Summary of scattering simulations from FY and MY ridges	146
5.24	Impact of salinity at top of sail for MY ridges, fall parameters	148
5.25	Impact of density at top of sail for MY ridges, fall parameters	149
5.26	Guide for discriminating between FY and MY ridges	151

List of Figures

1.1	Ground penetrating radar with field validation for a second year sea ice ridge taken from [4]	11
1.2	Illustration of main structure of a sea ice pressure ridge	14
1.3	Photos of first year (left) and multi-year (right) ridges	14
1.4	Geometry for two-layer media	18
1.5	Backscatter from stratified media with horizontal dipole source at 300 MHz	21
1.6	Geometry for rough surface	22
2.1	Geometry for Walsh scattering approach	38
2.2	Magnitude of co-polarized (left) and cross-polarized (right) fields for good conductor (top) and general surface (bottom). In both cases the simulation parameters are the same and the simulations are indistinguishable.	44
2.3	Magnitude of co-polarized (left) and cross-polarized (right) fields for general dielectric surface for $n_1 = 9$ (top) and $n_1 = 3$ (bottom) refractive index	45
2.4	Geometry of scattering angles	46
2.5	Field scattered from rough surface using small slope assumption	47
2.6	Field scattered from rough surface with small slope assumption removed	47

3.1	Surface roughness effect on Rayleigh roughness parameters	56
3.2	Salinity and brine volume for a second year ridge	59
3.3	Effective reflections from sea ice ridge	61
3.4	Rough surface over layers	61
3.5	Rough surface over layers	63
3.6	Scattering coefficients when $\Gamma = -0.5$ for a simple rough surface . . .	66
3.7	Co-polarized scatter when $\Gamma = -0.5$ (left) and $\Gamma = -0.99$ (right) . . .	67
3.8	Co-polarized modal scattering coefficients vs reflection coefficient ($ s_{yy}^q $ vs Γ). There is a separate trace for each value of q	68
3.9	Modal co-polarized scattering coefficients when $\Gamma = -0.5$ (scaled) and $\Gamma = -0.8$	69
3.10	Co-polarized scattered field may be scaled for Γ in linear range	70
3.11	Surface scattered field (left) and field transmitted through the surface (right)	70
3.12	Co-polarized scattering from the top and bottom of a rough surface .	82
3.13	Scattering components from the layers	84
3.14	Co-polarized and cross-polarized scatter from surface and layers . . .	85
3.15	Transmission line model for determining reflection and transmission coefficients	85
4.1	FY sea ice salinity vs depth, from [5]	92
4.2	Air volume vs density at a fixed temperature, from [6]	93
4.3	Density vs temperature for gas free ice, from [6]	94
4.4	Elevation profile from a FY ridge, from [7]	100
4.5	Cross section of FY ridge illustrating high macro-porosity, from [8] . .	102
4.6	Relative static dielectric permittivity for pure ice, from [9]	113
4.7	Relaxation time for pure ice, from [9]	114

4.8	General representation of FY (left) and MY (right) sea ice ridges . . .	127
4.9	Representation of FY (left) and MY (right) sea ice ridges for this research	128
5.1	Co-polarized and cross-polarized scatter from surface and layers . . .	131
5.2	Sea ice model for assessing impact of varying a single parameter . . .	132
5.3	Attenuation of 300 MHz EM signal in Sea Ice	134
A.1	Scattering coefficients for different correlation lengths	162
A.2	Rough surface over layers	163

List of Abbreviations

1D	one dimensional	22
2D	two dimensional	25
AIRSS	Arctic Ice Regime Shipping System	3
CIS	Canadian Ice Service	7
CRREL	Cold Regions Research and Engineering Laboratory	58
DC	direct current	112
EM	electromagnetic	5
FDTD	finite difference time domain	15
FY	first year	3
GNSS-R	Global Navigation Satellite Systems Reflectometry	8
HF	high frequency	33
IR	infrared	1
LIDAR	light detection and ranging	9
MY	multi-year	3
NIC	National Ice Center	2
NRC	National Research Council	107
PEC	perfect electric conductor	65
ppt	parts per thousand	90
psu	practical salinity units	90

S	salinity	90
S-EBCM	stabilized extended boundary condition method	16
SAR	synthetic aperture radar	1
SMOS	Soil Moisture and Ocean Salinity	6
SPM	small perturbation method	14
UHF	Very High Frequency	4
VHF	Very High Frequency	4
WMO	World Meteorological Organization	2

List of Symbols

M	total number of layers	17
∇	Del operator	17
\vec{E}	electric field	17
k	radar wavenumber	17
m	index for layer in stratified media	17
h_m	Heaviside function for interface between layers m and $m + 1$	17
n_m	refractive index for layer m	17
ω	radian frequency of source	17
μ_0	magnetic permeability of free space	17
\vec{J}_s	source current density	17
ϵ_m	dielectric permittivity of layer m	17
ϵ_0	dielectric permittivity of free space	17
μ_m	magnetic permeability of layer m	18
σ_m	conductivity of layer m	18
δ	Dirac delta function	18
E_z^{m+}	z component of electric field when approaching layer $m + 1$ from above	18
a_m	distance below surface to top of m th layer	18
γ	complex propagation constant	19

T_{SE}	electric source operator	19
E^{m+}	electric field when approaching layer $m + 1$ from above	19
E^{m-}	electric field when approaching layer $m + 1$ from below	19
I	antenna current	20
π_x, π_z	functions to calculate the field scattered from stratified media	20
R_0	position vector from centre of antenna to observation point	20
R_0	position vector from centre of antenna image to observation point	20
H	numerical integral for field scattered from stratified media	20
k_x, k_y	spatial wavenumbers	20
U_{1h}, U_{1z}	variables dependent on electrical characteristics of layers. Related to U_{mh}, U_{mz} introduced on page 71	20
u_0	$\sqrt{k_x^2 + k_y^2 - k^2}$	20
\vec{n}	surface normal	23
\vec{R}^+, \vec{R}^-	functions of the electric field and surface	23
\vec{E}_s	electric field of the source	23
K_{01}, K_{02}	Green's functions for above and below the rough surface, respectively	23
f_x, f_y	partial derivatives of surface with respect to x and y , respectively	24
r	position vector	23
u_1	$\sqrt{k_x^2 + k_y^2 - n_1^2 k^2}$	24
\vec{G}, \vec{F}	variables that are functions of \vec{E} and partial derivatives of \vec{E}	24
∇_{xy}	2D spatial gradient operator	25
g_1	spatially bandlimited electric field of source	25
G_{1L}	Fourier transform variable used to estimate bandlimited electric field of the source	25
k'_x, k'_y	spatial wavenumbers for g_1	25
A_n, A_q	Fourier transform coefficients	25, 28

k_0	wavenumber of sinusoidal surface	25
f	equation for the profile of the rough surface	26
a	amplitude of sinusoidal surface	26
b	offset for sinusoidal surface to ensure $f \geq 0$	26
q	mode in expansion of scattered field from rough surface	27
u_{0q}	q th mode of u_0 , i.e., $u_{0q} = \sqrt{k_x^2 + (k_y - qk_0)^2 - k^2}$	27
$\underline{E}_s^{z^-}$	Fourier transform of source electric field below the surface on the plane $z = z^-$	27
$\underline{E}_s^{z^+}$	Fourier transform of source electric field above the surface on the plane $z = z^+$	28
\underline{E}^{z^+}	Fourier transform of total electric field above the rough surface	28
\underline{E}^s	Fourier transform of scattered field	28
C_E	scaling term to simplify expression for scattered field	29
Σ	summation term used to represent source field as Neumann series	29
E_{syy}	contribution to y component of source field from y component of principal solution	29
p_q, r_q	scale factor on G_{1y} and G_{1z} , respectively, to calculate y component of scattered field	29
A, B	multipliers on \underline{G}_{1y} and \underline{G}_{1z} to determine y component of source field	30
C, D	multipliers on \underline{G}_{1y} and \underline{G}_{1z} to determine z component of source field	30
P, R	multipliers on \underline{G}_{1y} and \underline{G}_{1z} to determine y component of scattered field	30
V, S	multipliers on \underline{G}_{1y} and \underline{G}_{1z} to determine z component of scattered field	30
E_{0y}	magnitude of y component of incidence plane wave	30
E_{0z}	magnitude of z component of incidence plane wave	30

$T_q^{y,z}$	expression for G_{1y} and G_{1z} based on source term to calculate y component of scattered field	31
$U_q^{y,z}$	expression for G_{1y} and G_{1z} based on source term to calculate z component of scattered field	31
\circ	superscript is used to indicate delta function constraint is applied such that $k_x = -k_x^\circ$ and $k_y = -(k_y^\circ - qk_0)$ and $k_x^\circ = k \cos \theta_x$, $k_y^\circ = k \cos \theta_y$	32
θ_x, θ_y	incidence angle with respect to the normal of the average surface	32
f_{yy}	second partial derivative of surface f with respect to y	39
k_L	$k_L = e_L^{-f(x',y')u_0} e^{-jk_x x' - jk_y y'}$	39
Γ	reflection coefficient	46
$\alpha_{\beta\eta}$	multipliers on $\underline{G}_{1\eta}$ to calculate \underline{E}_s^β , where β and η can be x , y or z	49
$\rho_{x,y,z}$	multipliers on \underline{G}_{1x} , \underline{G}_{1y} , \underline{G}_{1z} , respectively	50
s_{xx}^q	modal co-polarized scattering coefficient	51
s_{xy}^q, s_{xz}^q	modal cross polarized scattering coefficient	51
σ_h	standard deviation of surface height	54
l_c	surface correlation length	54
$\Delta\phi$	path difference between incidence waves on a rough surface	54
Ra_r	Rayleigh roughness parameter for reflection	54
Ra_t	Rayleigh roughness parameter for transmission	54
C_R	variable to indicate surface roughness	55
k_1	radar wavenumber in medium below rough surface	55
θ_i	incidence angle of electric field on surface	55
θ_t	angle of electric field transmitted through the surface	55
n_{upper}	refractive index of upper layer	60
n_{lower}	refractive index of lower layer	60
\mathcal{T}	transmission coefficient through the rough surface	64

Γ_{PEC}	reflection coefficient from a perfect electric conductor	65
$\Gamma_{q,PEC}$	modal reflection coefficient from a perfect electric conductor	65
$s_{x_1x_2}^q _{PEC}$	modal reflection coefficient from perfect electric conductor for any x_1x_2 polarization combination	68
ν_1, ν_m	recursively calculated variables that depend on electrical properties of layers	71
$N_{10}, N_{(m+1)m}$	variable that is a function of the permittivity of layers 1 and 0 or $m + 1$ and m , respectively	71
r_H	reflection coefficient for horizontally polarized fields	72
r_V	reflection coefficient for vertically polarized fields	72
Γ_{Ly}, Γ_{Lz}	scattering coefficients from stratified media for the y and z compo- nents, respectively	73
u	superscript (u) indicates that variables are calculated with respect to the underside of the rough surface	75
n_{ice}	refractive index for top layer of ice, equivalent to n_1 . New variable introduced since considering scattering from underside of rough sur- face	75
K^+	$K^+ = e^{f(x',y')u_0} e^{-jk_x x' - jk_y y'}$	76
$\mathcal{T}_{x_o x_i 1}$	transmission coefficient for input polarization, x_i , to output polar- ization, x_o , for transmission down through the surface	82
$\mathcal{T}_{x_o x_i 2}$	transmission coefficient for input polarization, x_i , to output polar- ization, x_o , for transmission up through the surface	82
E_0	incident electric field	84
$\mathcal{T}_{L_1 L_2}$	transmission coefficient from layer L_1 to layer L_2	84
$\Gamma_{L_1 L_2}$	reflection coefficient from layer L_1 to layer L_2	84
E_2^s	field scattered from interface 2	84

ν_t	total sea ice micro-porosity	94
V_{br}	brine volume fraction	94
V_a	air volume fraction	94
H_k	keel depth	97
H_s	sail height	97
$\epsilon'_{r\infty}$	high frequency or optical limit of relative permittivity	112
ϵ'_{rs}	static or low frequency limit of relative permittivity	112
σ_{DC}	ionic conductivity	112
τ	relaxation time	112
i	subscript to indicate Debye parameters for pure ice	113
br	subscript to indicate Debye parameters for brine	113
sw	subscript to indicate Debye parameters for sea water	113
a	subscript to indicate Debye parameters for air pure ice	113
T	temperature	114
N	normality, gram equivalent weight of solute per liter of solution	114
S_{br}	brine salinity	114
σ_{br}	brine conductivity	116
Δ	25- T , measured in °C	116
S_{sw}	sea water salinity	116
δ_{sw}	skin depth of sea water	117
ρ	sea ice density (g/cm ³)	118
ρ_{br}	brine density (g/cm ³)	118
$F_1(T)$	piecewise polynomial used to calculate V_{br}	118
ρ_i	density of pure ice	118
$F_2(T)$	piecewise polynomial to account for solid salts when calculating V_a	118
ρ_i	density of pure ice	118

m_{ss}	mass of solid salts	119
m_{br}	mass of brine	119
C	scale factor relating m_{ss} to m_{br}	119
$\epsilon_{r,ia}$	relative permittivity of mixture of pure ice and air	119
$\epsilon_{r,m}$	relative permittivity of sea ice mixture	120
$\epsilon'_{r,m}$	real component of relative permittivity of sea ice mixture	120
$\epsilon''_{r,m}$	imaginary component of relative permittivity of sea ice mixture	120
n_p	depolarization factor due to sea ice structure and orientation of brine inclusions	120
$\epsilon_{r,MP}$	relative permittivity of ice accounting for macro-porosity	120
V_{MP}	volume fraction of air due to macro-porosity	120
σ_e	effective conductivity of sea ice	121
a	amplitude of sinusoidal surface variation	132
t	average thickness of single ice layer	132

“...an academic education will...begin to give you an idea what size mind you have. After a while you’ll have an idea what kind of thoughts your particular size mind should be wearing.”

—J. D. Salinger, *The Catcher in the Rye*

Chapter 1

Introduction

1.1 Context and Motivation

Canada is a northern nation whose culture, recreation and commercial endeavors are affected by sea ice. Canada also has the oldest, thickest and strongest sea ice in the world. Over recent decades the impacts of climate change on the areal extent of Arctic sea ice have been noted (e.g., [10]) and have been accompanied by reductions in ice thickness (e.g., [11]). Although the decline in Arctic sea ice has encouraged increases in marine traffic [12], the reduced ice is a factor in increased storm activity causing ice drift to be more dynamic and less predictable [13]. Even though there is less ice, the hazard posed by the ice has not reduced. Due to the dynamic nature of sea ice, knowledge of historical sea ice conditions is not sufficient and observation data are needed for accurate knowledge of ice conditions.

Fortunately, observation data are collected continually, primarily using polar orbiting satellites. Operational ice charts are based on the highest-quality data available starting with synthetic aperture radar (SAR) augmented by visible/infrared (IR) data and passive microwave when needed [14]. Typically nations with coastlines along ice-

prone regions map sea ice conditions close to their own borders, although some ice charting responsibilities are shared among countries that have interests in the same region [15]. In certain cases countries support ice charting in other regions as well. For example, the United States National Ice Center (NIC) generates regular ice charts for the entire Arctic and Antarctic [16]. Although charts produced in different regions will have slight differences from each other, efforts have been made to standardize terminology and data formats to facilitate information sharing between ice centres and promote understanding of ice conditions [15].

Standard sea ice charts provide information that conforms to the World Meteorological Organization (WMO) nomenclature using features that could be visually discerned in a qualitative manner at the time the nomenclature was developed in 1970 [17]. The original classification scheme has been updated based on information requirements and the availability of high resolution satellite data. Modern operational ice charts contain information that is of interest to marine operations: sea ice concentration, which is typically expressed in tenths; ice form, which specifies if it is landfast ice or indicates the floe size distribution; ice thickness, which is related to the stage of development of the ice; and ice movement. Regarding ice thickness, WMO standard classes place a strong emphasis on young ice types and information is provided in thickness categories. Although melting ice types may be described using WMO nomenclature [18], this information is not typically included on publicly available ice charts, possibly due to the challenges of identifying puddles, melt ponds and thaw holes using SAR data with resolution on the order of 100 m. More detailed sea ice thickness information is available in some areas. In the Baltic Sea, for example, new SAR data are combined with recent sea ice thickness charts to update the sea ice thickness information [19].

Although the stage of development affects the ice thickness, sea ice deformation

has a much larger impact on total sea ice thickness. Sea ice deformation occurs when there is a lead of thin ice or open water separating ice floes and compressive forces bring those floes together. Sea ice deformation typically occurs early in the ice season when the ice is thinner [20], since the forces required are generally not strong enough to break thicker floes [21]. It is estimated that 30-80% of the volume of sea ice is in ridged ice [22], but information on sea ice ridges is typically not provided on ice charts. Regions of heavy ridging may be indicated in special circumstances [23].

Ridging information is important for both climate change studies and navigation. Ridged ice is thicker than level ice and is more likely to survive the summer melt season. Multi-year (MY) ice is an important barrier to the loss of ice in the Arctic and is less prone to rapid deterioration as is thinner first year (FY) ice. Thus, the coverage of thicker, ridged ice is an important parameter for modeling the sea ice albedo feedback.

For navigation purposes, sea ice thickness is often used as a proxy for strength and vessels are assigned an ice class based on the severity of the ice conditions that can be handled, where the primary consideration is ice thickness and ice age (i.e., FY, second year and MY) [24], [12]. However, the structure and thermodynamic state of the ice also have a major impact on ice strength. The Arctic Ice Regime Shipping System (AIRSS) takes into account that cold ice is stronger than melting ice, MY level ice is stronger than FY level ice, ridged ice is stronger than level ice and MY ridged ice is stronger than FY ridged ice [25]. All that remains is to find a way to identify stronger ice types so they may be avoided and there are ways this can be done: air temperature may be used as a guide to determine when ice is melting, microwave signatures may be used to distinguish between FY and MY level ice (e.g., [26]) and SAR data have been used to separate ridged from level ice (e.g., [27]). However, limited attention has been paid to using remote sensing data to distinguish between FY and MY ridges.

1.2 Aim and Goals of the Research

The overall aim of the research is to determine if remote sensing data may be used to distinguish between FY and MY ridges. The approach taken in this study is to simulate the scatter from ridges using frequencies at Very High Frequency (VHF) and lower Ultra High Frequency (UHF) range from 100-500 MHz, which is a frequency band frequently used in impulse radars for sea ice thickness measurement (e.g., [4]). Since most of the simulations and analysis is conducted at 300 MHz, the work will refer to operating at VHF. The general tasks completed through the research are listed below:

- Develop or modify scattering equations that are suitable for modeling scatter from sea ice;
- Develop a sea ice ridge model that includes all relevant features for scattering at the frequencies of interest; and
- Use the scattering model with the sea ice model to assess the scattering differences between FY and MY ridges.

This research will help improve interpretation of radar data collected over sea ice so that more information may be extracted from field studies for better scientific understanding of sea ice and safer and more efficient operations in sea ice. Identifying hazardous MY ridges is important since ridges and MY ice are often embedded in FY sea ice. Since VHF sensors are often used for ice thickness measurement, the results of this research may be used to enrich the data set from those sensors by indicating if ridges are FY or MY features. The literature review in the following section provides context and background for the research.

1.3 Literature Review

This thesis spans the two fields of sea ice remote sensing and scattering from rough surfaces and stratified media. Hence, this literature review covers those two areas. This review begins with an overview of sea ice remote sensing using electromagnetic (EM) devices, with an emphasis on ice thickness measurement and estimation. A detailed description of relevant sea ice properties and how they affect the dielectric permittivity is addressed in Chapter 4 and a brief description of the various sea ice deformation types is given in Section 1.3.2. The following sections provide context for scattering from rough surfaces, stratified media and rough, layered media. The final section of the review provides an introduction to the Walsh scattering approach, which has been used for this research.

1.3.1 Sea Ice Remote Sensing using EM Energy

Observations of sea ice began centuries ago with the first polar explorations, but the emphasis was on avoiding the ice rather than studying it [21]. Sea ice observations using EM sensors have been conducted from shore, water, air and space over tactical, regional and hemispheric scales. Tactical data are collected over a localized area and provides detailed and timely information on individual ice features to support decision making. Mapping at regional and hemispheric scales covers much larger areas, but provides areal averages of ice conditions instead of detecting specific features and is important for route planning and climate studies. Since sea ice ridges are only a few metres wide it is important to collect data at tactical scales, but also to understand how coarser resolution data may be used.

Ice reconnaissance began from shore-based stations and vessels using visual observations over 100 years ago [5]. Today, marine radars are an important tool for

monitoring sea ice. Operating at X-band (8.0-12.0 GHz) and S-band (2-4 GHz), marine radar provides advanced notice of ice hazards. High scan rate antennas and scan to scan averaging improve the delineation of the coastline, ice floes and leads and enhance detection of small pieces of glacial ice at further ranges. Due to the imaging geometry, features with surface relief such as icebergs and ridges will have a shadow, making them easier to detect. It is expected that dual-polarized marine radar will improve the ability to discriminate between FY and MY ice [28].

Satellite surveillance of sea ice has been gaining importance since the 1970s and is presently the most important source for global sea ice information [29]. Since many satellites operate in a polar orbit, Arctic and Antarctic regions are covered more frequently than equatorial latitudes. Initial optical and IR satellite sensors were successfully used for mapping sea ice coverage and structure and thermal data are able to estimate ice thickness up to 0.5 m [30].

Microwave sensors were developed to allow operation at nighttime and through cloud cover. The first passive microwave device was launched in 1972 and was used to generate coarse resolution (30 km) sea ice concentration maps, but resolution improved with future devices [29]. Passive microwave data are collected in the range 19-91 GHz and may be analyzed to assess sea ice concentration, discriminate between FY and MY ice and detect melt onset. Accurate measurements by passive microwave are hindered by snow cover and melt ponds. There are tradeoffs for using different frequencies. Passive microwave data have resulted in a daily, global, continuous data record that spans decades [14], [31].

Passive microwave data at the typical frequencies of 19 and 37 GHz may be used to retrieve sea ice thickness up to 20 cm, but the retrieval is based on known relationships between surface properties and sea ice thickness [32]. The Soil Moisture and Ocean Salinity (SMOS) sensor receives radiation emitted at 1.4 GHz and may be used to

estimate sea ice thickness for thin sea ice less than 0.5 m thick and uncertainty in the measurement increases for greater ice thickness [33]. In both cases the retrieval is not possible during the melt season.

Scatterometer data have been available continuously since 1992 and have also been used to determine sea ice coverage. Scatterometers are active devices often operating at two frequencies in the GHz range. Coarse resolution data are collected at different azimuth angles to support their primary application of measuring winds over the ocean [17]. Scatterometers provide an excellent independent check on sea ice extent derived from passive microwave sensors during fall and winter. Scatterometer signals respond more sensitively to melting ice and lower concentration ice present during spring and summer. This provides a correction to passive microwave data that are rendered less accurate by melt ponds [34].

Satellite SAR data first became available in 1978, but it wasn't until 1991 that a large volume of SAR images became available regularly. SAR images can be collected at nighttime and through cloud cover and are relatively insensitive to atmospheric conditions. Images used for ice charting have a swath width of up to 500 km and spatial resolution around 100 m. For these reasons, satellite SAR is the most important tool for sea ice charting [14]. Charts produced by national ice centres such as the Canadian Ice Service (CIS) generate regional and daily ice charts populated with information on total ice concentration and the main ice types along with their partial concentrations and dominant floe sizes. The ability to discriminate between sea ice types, including FY and MY ice, is hindered during the melt season when wet snow or melt ponds cover the ice. However, dual-frequency data sets collected at C-band (~ 5 GHz) and L-band (~ 1 GHz) are able to discriminate between ice types [35].

Although C-band sensors are very popular in satellite SAR systems (e.g., ERS-1/2, RADARSAT-1/2, ENVISAT, SENTINEL-1), L-band SAR data have only been

collected using JERS-1, PALSAR and PALSAR-2. However, multi-frequency data, including L-band, may be collected from aircraft using sensors such as AIRSAR, EMISAR, E-SAR and Pi-SAR. When sufficiently high resolution is used, individual ridges are visible in satellite SAR [36] and ridge frequency has been related to the backscatter coefficient [27], but to the author’s knowledge no work has been conducted on discriminating between FY and MY ridges.

The laser altimeter of ICESat collected measurements every 170 m with a spatial footprint of 70 m. ICESat-2 was launched in 2018 with an improved sensor that uses three pairs of lasers to better measure surface slope and provides better spatial coverage [37]. Space-borne radar altimeters have been available since the launch of GEOSAT in 1985 [38] and data continue to be available through satellites such as CryoSat-2 [39] and Sentinel-3 [40]. Data are collected in a narrow swath and are assimilated with charts of sea ice extent and concentration to produce monthly ice thickness maps [41]. Laser signals reflect from the snow surface allowing total freeboard to be measured and radar altimeter signals reflect from the ice surface allowing ice freeboard to be measured. Due to the buoyancy of ice, freeboard measurements may be extrapolated to estimate total ice thickness and a small error in freeboard translates into a larger error for overall ice thickness. Snow cover can weigh down the ice and estimates of the snow depth and snow density are taken from model data or climatology. Uncertainty in snow parameters is the biggest source of error for altimeter measurements of sea ice thickness [41], [42].

Global Navigation Satellite Systems Reflectometry (GNSS-R) has recently been emerging as a new tool for sea ice monitoring. GNSS-R uses reflected L-band geosynchronous satellite signals used for navigation and has been applied to a wide range of applications [43]. The data have been used to detect sea ice [43], [44], determine sea ice concentration [45] and estimate sea ice thickness [46].

Aerial surveillance of sea ice began after World War II and remained prominent until the 1980s when satellite data became more prevalent [17]. Aerial data were a critical factor in the transition from airborne to spaceborne since satellite mission concepts and sensor suites could be evaluated more quickly and cost effectively from the air. Aircraft can carry a wide range of sensors that are responsible for sea ice monitoring around the world to support exploration, operations and science [47], [48].

Aircraft may also carry additional sensors very useful for sea ice thickness measurement. Light detection and ranging (LIDAR) has been used to measure surface roughness and surface height [49]. When used with a radar altimeter, it is possible to determine snow thickness and sea ice freeboard. Using knowledge of aircraft motion and the earth geoid along with assumptions on snow and sea ice density, it is possible to estimate sea ice thickness. Successful aircraft missions were a driver of satellite-based altimetry for sea ice thickness [50].

EM sounding has also been carried out from fixed wing and helicopter platforms. An EM field is generated, which induces eddy currents in the conductive sea water. These eddy currents generate a secondary magnetic field which can be detected by the EM receiver. The magnitude of the detected field is proportional to the total snow and ice thickness [51]. The thickness accuracy is approximately 0.1 m for level ice, but errors of 30% are expected for deformed ice, partly because water may be present between blocks of ice. The horizontal dimensions of area on the ice illuminated by the EM field footprint are similar to the height of the device above the surface [52]. EM sensors may also be dragged over the ice to measure thickness (e.g., [53]).

It is also possible to estimate the thickness of thin sea ice using aerial SAR. Ratios of multi-polarization L-band data were used to mitigate the impact of surface roughness. The ratios were found to be a function of the dielectric properties of the ice. Since the salinity and permittivity of thin, growing ice changes in a well understood

manner it was possible to correlate the multi-polarization scattering ratio to be a function of ice thickness [54].

Impulse radar, operating around VHF frequencies, has been used to measure sea ice thickness from aircraft. During initial studies it was difficult to determine thickness for MY and deformed ice [55], but accuracies over thick MY floes in a later study were accurate to within 10% [56]. An early Russian system [57] was used to successfully measure ice thickness for freshwater and MY ice. It was noted that it is possible to discriminate between FY and MY ice and the shape of the scattered signal varied with the ice type as a function of the salinity, age, structure and temperature of the ice. An example of penetrating radar collected over a sea ice ridge is given in Figure 1.1. Impulse radar systems have also been dragged over the ice to measure ice thickness (e.g., [4], [58]). The accuracy of ice thickness measurements was hindered when moist ice was encountered and internal features such as brine or air pockets resulted in a strong reflection, but field sampling was needed to determine the nature of the inclusion. Similarly, impulse radar data collected over ice roads revealed cracks that are a normal part of the construction process [59]. It has also been noticed that there are layers in FY and MY level ice and that the layers are less ordered for MY ice [60], but ridges were avoided due to their more complex structures. Extensive impulse radar data have also been collected over glaciers and been used to assess glacier structure (e.g., [61]). It is clear that impulse radar may be used to measure ice thickness and detect anomalies in level ice, but to the author's knowledge work has not been devoted to comparing the scattering differences between FY and MY ridges using penetrating radar. The research reported in this thesis is not directly based on any of the remote sensing technologies described in this section, but takes a more fundamental approach of modeling how EM fields scatter from a model representation of sea ice ridges. However, the geometry and EM frequencies used for the research

are most similar to impulse radar. For this research sea ice ridges are considered to have a rough surface over layers.

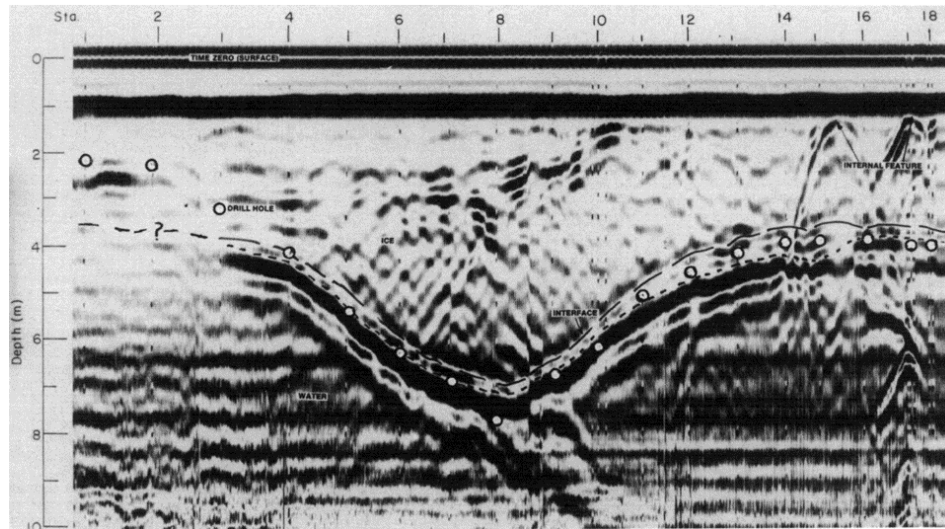


Figure 1.1: Ground penetrating radar with field validation for a second year sea ice ridge taken from [4]

1.3.2 Sea Ice Deformation

Sea ice is always changing. From a macroscopic perspective we can observe sea ice growing and ablating, but the accompanying internal changes have a significant impact on the ice strength and how EM fields will interact with it. Young sea ice is very saline, but as it grows brine is expelled into the sea water and onto the ice surface. The salinity profile over depth has a characteristic ‘C’ shape with higher salinities at the top and bottom of the ice [5]. Ice crystals are initially small and randomly oriented, but as sea ice grows the ice crystals elongate and become aligned with each other and with the direction of the current. Brine is not included in the ice crystal structure, but is present in inclusions between crystals. As the temperature drops the brine becomes more concentrated as some of the water freezes. At specific, cold temperatures, hydrous salts begin to precipitate from the ice and cause step changes

in the electrical characteristics of the ice. As temperatures warm, the brine volume increases as the ice melts. Surface meltwater flushes brine from the ice and the top 0.1-1 m of the ice may become virtually brine-free. If the ice survives the summer melt season the old ice (ice that has survived at least one melt season) may have portions of freshwater ice from refrozen melt ponds and the pre-existing ice will be retextured with rounded, instead of sharp, boundaries between crystals [21], [62], [63].

Not only are the internal structure and characteristics of sea ice always changing, but environmental forces cause ice to be redistributed as deformed ice features. Ice deformation may begin when there is a lead or crack in the ice and, when ice sheets with differing thickness are present, the thinner ice deforms first. Evidence of this is found in numerous field studies that showed that ice blocks in ridges are typically only a few tens of centimeters thick (e.g., [8], [20], [64]). Although this research focuses on pressure ridges, a brief description of the major types of deformation is provided below.

Rafting generally occurs for flexible ice less than 10 cm thick. A thin elastic crust of ice called nilas forms in a new lead or crack. When the bounding ice sheets move slightly, the nilas cracks. Further movement of the thicker ice can force one sheet over the other and this may occur in an alternating pattern known as finger rafting. Although the ice is not thick enough to support its own weight, it is able to slide over itself for up to 100 m without breaking since brine draining from the upper sheet provides lubrication [21].

Another way thin ice may deform is by folding. Folding occurs when there is a compressive or shearing force on either side of a recently frozen lead. For compressive forces, the fold will be perpendicular to the axis of the lead and for shear forces a set of diagonal folds will occur [21].

Shear ridges are formed when the forces are parallel to the original lead. They

can extend for tens of kilometers and appear as a vertical wall at the seaward side. Shear ridges frequently form around grounded ice [21] and consist of finely ground and compacted ice instead of ice blocks [65].

A stamukha (plural stamukhi) is a pile of grounded ice that forms along coastlines with relatively shallow continental shelves. Stamukhi have been found with sail heights of 30 m [66] with areal coverage of tens of square kilometers [21].

Rubble fields are large areas characterized by broken sea ice. Rubble fields do not extend far above the water, but are very rough. As with other deformed ice classes, rubble fields are formed from relatively thin ice.

Pressure ridges are created when ice floes collide with each other, fast ice or land. The pressure of the impact breaks the ice and forces most of the broken blocks downwards to form the keel and some of the blocks upwards to form the sail. Over time, the ice blocks in the keel and bottom of the sail will refreeze to form the consolidated layer. An illustration of the main components of the ridge is given in Figure 1.2. Maximum ridge height depends on ice thickness and strength and once the maximum height is reached the ridge grows wider [67]. FY ridges have a curvilinear shape and may extend for several kilometers. The sails of FY ridges have a blocky appearance since the blocks have not weathered. When FY ridges survive one melt season they are known as second year ridges and after two melt seasons they become MY ridges. FY and MY ridges are the subject of this research, although some data on second year ridges will be used as required. Figure 1.3 shows photos of a FY and a MY ridge and illustrates that it is easy to distinguish between these ridges based on the appearance of their surface texture. It is apparent that optical data will be useful for identifying MY ridges, but EM data can be collected in all weather conditions and is a proven method to measure ice thickness when configured as an impulse radar. This research seeks to augment the information that can be collected on sea ice ridges using VHF

remote sensing.

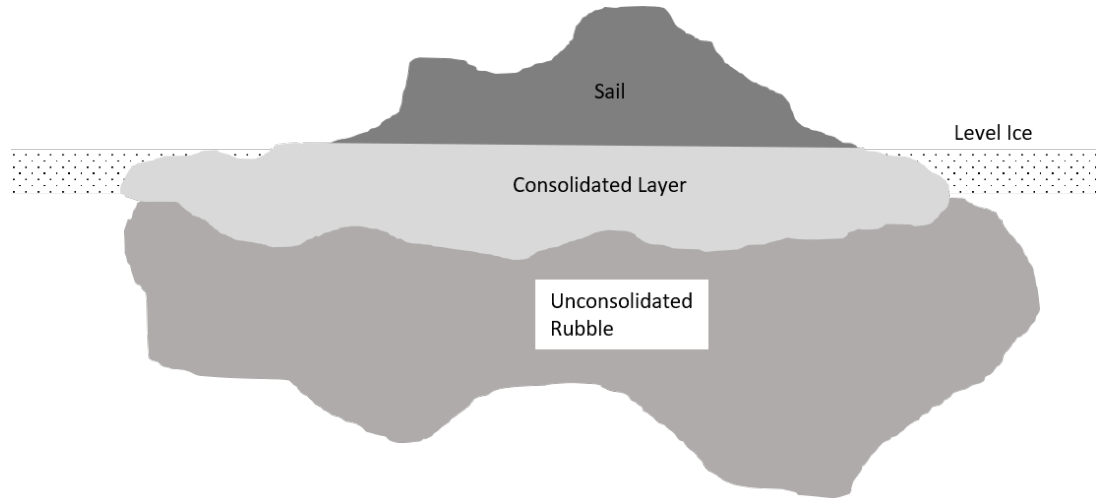


Figure 1.2: Illustration of main structure of a sea ice pressure ridge



Figure 1.3: Photos of first year (left) and multi-year (right) ridges

1.3.3 Rough Surface and Stratified Media Scattering

This research brings together the areas of EM scattering from rough surfaces and scattering from stratified media, both of which are mature areas. Rough surface scattering has received considerable attention since the 1950s [68], [69] and was initially focused on analytical methods. The small perturbation method (SPM) may be used

to simplify the analytical equations when the surface heights and slopes are assumed to be small and involves expressing the surface field as a perturbation series. The perturbation expansion may be truncated since surface variations are assumed to be small and result in the scattered wave being only a slight deviation from the wave scattered from a smooth surface [68], [70]. The Kirchoff approximation [71] is useful when the radar wavelength is small with respect to the surface undulations, in which case it is assumed that the scattering may be modeled as reflection from a plane oriented at the local slope of the surface. Thus, it can be seen that the small perturbation method is better suited for when the EM wavelength is on the order of the surface variation and Kirchoff's method may be applied when the EM wavelength is much smaller than the surface variation. Other analytical approaches are often referred to as unifying theories, since they aim to describe scattering behaviour when the surface variation is shorter and longer, with respect to the EM wavelength. Some unified methods include the phase perturbation method, small slope approximation and unified perturbation method and there are several approximate analytical methods as well [72].

There is a broad range of numerical methods that may be used to solve approximations to Maxwell's equations in integral or differential form. Method of moments can be used for both integral and differential equation methods and yields accurate results without requiring the entire domain to be discretized since only values at the boundaries are needed [73]. Of all the numerical methods the Finite Difference Time Domain (FDTD) method, which provides a direct solution of Maxwell's equations, is the most straight forward to implement [74]. While analytical methods result in equations that yield solutions rapidly and provide insight on how the EM wave interacts with the surface, it may be difficult to assess the impacts of the approximations. Numerical methods, on the other hand, can achieve almost exact results, but can have long computation times and may be unstable.

Wait [75] prepared a seminal text on scattering from stratified media whose properties vary in one specific direction. He initially considered discretely stratified media consisting of parallel homogeneous layers with the incident wave in the form of a plane wave, cylindrical wave or spherical wave for normal or oblique incidence with the emphasis on propagation across the surface. The analysis assumes that there is no reflection from the bottom of the lowest layer as it is semi-infinite. To determine the scattered fields above the surface the boundary conditions are solved for each layer iteratively. Continuously-stratified media are also considered when the electrical parameters follow specific profiles.

Analytical scattering models have also been developed when the medium is sinusoidally stratified, provided the variations in the dielectric constant are small [76]. Chen [77] analyzed scattering involving random media under specific profiles and suggested increasing the number of layers for very inhomogeneous media.

Research combining scattering from rough surfaces and stratified media is also a mature area. Kubik [78] developed the scattering equations for two-layered media when the top surface is rough. More recently, scattering from rough layers has been approached by extending the small perturbation method. Imperatore *et al.* [79] developed a closed form solution using rough layers. This work was further advanced by considering rough layers and inhomogeneous media [80] and was applied to the problem of radar wave propagation across snow-covered ice. Duan [81] developed a semi-analytical method referred to as the stabilized extended boundary condition method (S-EBCM) for scattering from rough surfaces and inhomogeneous media. The S-EBCM was applied to soil remote sensing and shown to be valid for 3D domains with roughness scales beyond those which analytical methods can usually handle.

1.3.4 Walsh Scattering Approach

This research builds on the rough surface [82] and stratified media [83], [84] analysis developed by Walsh. A more detailed description of his approach is provided in this section as a background to the research described in the remainder of this thesis.

Walsh Approach - Stratified Media Scatter

Walsh develops the equations for scattering from a simple two layer case and expresses the results in a way so that it is possible by inspection to generalize to M layers. The geometry for the $M = 2$ layer case is illustrated in Figure 1.4. Beginning with Maxwell's equations, the Helmholtz equation is derived as

$$\nabla^2 \vec{E} + k^2[(1 - h_1)n_2^2 + (h_1 - h_0)n_1^2 + h_0]\vec{E} = j\omega\mu_0\vec{J}_s + \nabla(\nabla \cdot \vec{E}), \quad (1.1)$$

where \vec{E} is the electric field intensity,

∇ is the 'Del' operator,

k is the radar wavenumber,

h_0 is the Heaviside function for the interface between free space and the top layer of the ice and h_1 and h_2 are similarly defined,

n_1 and n_2 are the refractive indices for the first and second layers below free space, respectively,

μ_0 is the magnetic permeability of free space, as well as for sea ice and sea water,

ω is the radian frequency of the source and

\vec{J}_s is the source current density above the layers centred at $x = y = 0$.

The refractive index of the m th layer is related to the permittivity of that layer as

$$n_m = \sqrt{\epsilon_m/\epsilon_0} \quad (1.2)$$

where ϵ_m is the permittivity of the m th layer and ϵ_0 is the permittivity of free space.

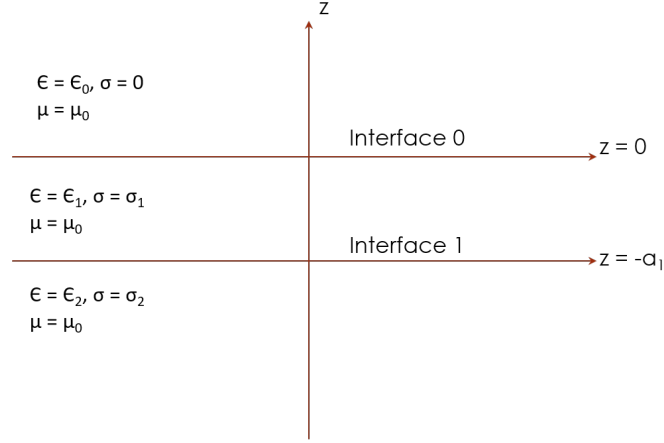


Figure 1.4: Geometry for two-layer media

The final term, $\nabla(\nabla \cdot \vec{E})$, in (1.1) is found to be

$$\begin{aligned} \nabla(\nabla \cdot \vec{E}) = & -\frac{1}{j\omega\epsilon_0} \nabla(\nabla \cdot \vec{J}_s) + \left(\frac{n_2^2 - n_1^2}{n_2^2} \right) \nabla(E_z^{1+} \delta(z + a_1)) + \\ & \left(\frac{n_1^2 - 1}{n_1^2} \right) \nabla(E_z^{0+} \delta(z)), \end{aligned} \quad (1.3)$$

where E_z^{m+} is the z -component of the electric field when approaching layer $m + 1$ from above, a_1 is the depth below the surface to the first interface and $\delta()$ is the Dirac-delta function. Noting the structure of (1.3) it is possible to write the expression for M layers by inspection as

$$\nabla(\nabla \cdot \vec{E}) = -\frac{1}{j\omega\epsilon_0} \nabla(\nabla \cdot \vec{J}_s) + \sum_{m=0}^{M-1} \left(\frac{n_{m+1}^2 - n_m^2}{n_{m+1}^2} \right) \nabla(E_z^{m+} \delta(z + a_m)). \quad (1.4)$$

Since for free space $n_0 = 1$, the Helmholtz equation for M layers is

$$\nabla^2 \vec{E} + \gamma^2 \vec{E} = -T_{SE}(\vec{J}_s) + \sum_{m=0}^{M-1} \left(\frac{n_{m+1}^2 - n_m^2}{n_{m+1}^2} \right) \nabla(E_z^{m+} \delta(z + a_m)), \quad (1.5)$$

where T_{SE} is the electric source operator defined as $\frac{1}{j\omega\epsilon_0}[\nabla(\nabla \cdot) + k^2]$,

a_m is the distance below the surface to the m th interface and

$\gamma = k\sqrt{\sum_{m=0}^{M-1} n_m^2 [h(z + a_m) - h(z + a_{m-1})]}$ is the complex propagation constant with $a_{-1} = \infty, a_{M-1} = -\infty, a_0 = 0$.

Returning to the two-layer case it is possible to write the Helmholtz equation for the upper half space (1.6), the first layer (1.7), the second layer (1.8) and the boundary conditions at the bottom layer (1.9) and top layer (1.10):

$$h_0[\nabla^2 \vec{E} + k^2 \vec{E}] = -T_{SE}(\vec{J}_s) \quad (1.6)$$

$$(h_1 - h_0)[\nabla^2 \vec{E} + n_1^2 k^2 \vec{E}] = 0 \quad (1.7)$$

$$(1 - h_1)[\nabla^2 \vec{E} + n_2^2 k^2 \vec{E}] = 0 \quad (1.8)$$

$$[\vec{E}^{1+} - \vec{E}^{1-}] \delta'(z + a_1) + \left[\frac{\partial \vec{E}^{1+}}{\partial z} - \frac{\partial \vec{E}^{1-}}{\partial z} \right] \delta(z + a_1) = \frac{n_2^2 - n_1^2}{n_2^2} \nabla[E_z^{1+} \delta(z + a_1)] \quad (1.9)$$

$$[\vec{E}^{0+} - \vec{E}^{0-}] \delta'(z) + \left[\frac{\partial \vec{E}^{0+}}{\partial z} - \frac{\partial \vec{E}^{0-}}{\partial z} \right] \delta(z) = \frac{n_1^2 - 1}{n_1^2} \nabla[E_z^{0+} \delta(z)] \quad (1.10)$$

The boundary condition expressions include the variables for the electric field approaching layer 1 from above and below that surface ($\vec{E}^{1+}, \vec{E}^{1-}$) and approaching layer 0 from above and below that surface ($\vec{E}^{0+}, \vec{E}^{0-}$). Note that the boundary con-

ditions proceed naturally from the analysis and are not externally imposed. Next, Green's solutions, a vector identity and a Fourier transform are then used to transform the three equations for each layer. By selecting a plane above and below each interface, four new equations are generated, which may be used to solve for the unknown values of the electric field and its vertical derivative above each interface. The solution is generated using a matrix equation. Walsh [84] then generalizes the solution to M layers. The equation must be calculated recursively and is valid for any source. Walsh provides examples for vertical and horizontal infinitesimal dipoles. For an infinitesimal horizontal dipole of length dl with current I at a height h above the surface the source current density is

$$\vec{J}_s = Idl\delta(x)\delta(y)\delta(z - h)\hat{x}. \quad (1.11)$$

After inverse Fourier transformation the scattered electric field for the two-layer case may be simply expressed as

$$\vec{E} = T_{SE}(\pi_x\hat{x} + \pi_z\hat{z}). \quad (1.12)$$

The expressions for π_x may be partially inverted in closed form, but π_z must be computed numerically. The spatial-domain expressions are

$$\pi_x = \frac{Idl}{4\pi} \left[\frac{e^{-jkR_0}}{R_0} - \frac{e^{-jkR_1}}{R_1} \right] + 2H \quad (1.13)$$

$$\pi_z = \frac{Idl}{4\pi^2} \iint \frac{jk_x \left(1 - \frac{1}{n_1^2}\right) e^{-(z^++h)u_0}}{(u_0 + U_{1h}) \left(u_0 + \frac{1}{n_1^2}U_{1z}\right)} e^{jk_x x + jk_y y} dk_x dk_y \quad (1.14)$$

where $H = \frac{1}{2\pi} \iint \frac{e^{-(z^++h)u_0}}{u_0 + u_{1h}} e^{jk_x x + jk_y y} dk_x dk_y$,

U_{1h} and U_{1z} are a function of the electrical characteristics of the layers,

$$R_0 = \sqrt{x^2 + y^2 + (z^+ - h)^2},$$

$$R_1 = \sqrt{x^2 + y^2 + (z^+ + h)^2},$$

$$u_0 = \sqrt{k_x^2 + k_y^2 - k^2} \text{ and}$$

k_x and k_y are the spatial wavenumbers.

Walsh [84] simplified the double integrals of (1.13) and (1.14) to single integrals involving Bessel functions, but in this study the resulting fields have been simulated as part of this research by numerically solving the double integral and an example is shown in Figure 1.5. It should be noted that the equations are for the far field case and the application of this technique cannot assume the case of an EM source placed directly on or just above the ice.

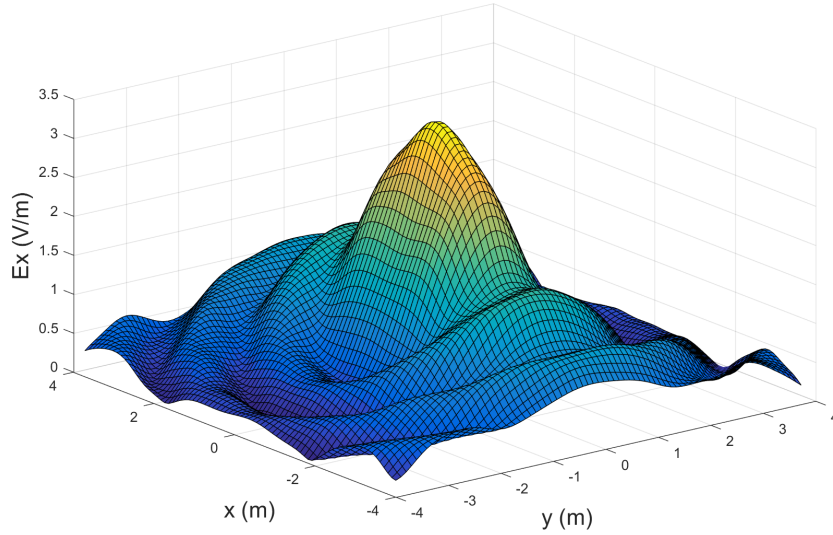


Figure 1.5: Backscatter from stratified media with horizontal dipole source at 300 MHz

Walsh Approach - Rough Surface Scatter

Walsh's scattering methodology has been developed for scattering from random, rough surfaces [85], but an earlier iteration of his work [82] has been considered for this

research where the surface is assumed to be bounded to a maximum height and the surface has a one dimensional (1D) sinusoidal variation in the y direction only.

Walsh's approach to rough surface backscatter [82] involves solving integral equations above and below the surface along with a boundary condition. When the incident radiation is a plane wave and the rough surface is periodic it is possible to obtain a closed form approximation. For all other situations numeric solutions are possible. Initial development of the equations is similar to the stratified media case and will not be repeated here. The geometry is illustrated in Figure 1.6.

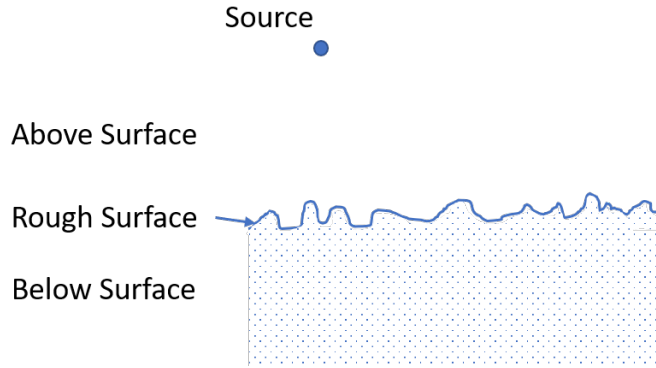


Figure 1.6: Geometry for rough surface

The equations above and below the surface along with the boundary conditions are found to be

$$h[\nabla^2 \vec{E} + k^2 \vec{E}] = -T_{SE}(\vec{J}_s), \quad (1.15)$$

$$(1 - h)[\nabla^2 \vec{E} + \gamma^2 \vec{E}] = 0, \quad (1.16)$$

and

$$\begin{aligned}
|\vec{n}| \left[\left(\frac{\partial \vec{E}}{\partial |\vec{n}|} \right)^+ - \left(\frac{\partial \vec{E}}{\partial |\vec{n}|} \right)^- \right] \delta(z-f) + \nabla \cdot \left[\vec{n} (E_x^+ - E_x^-) \delta(z-f) \right] \hat{x} \\
+ \nabla \cdot \left[\vec{n} (E_y^+ - E_y^-) \delta(z-f) \right] \hat{y} + \nabla \cdot \left[\vec{n} (E_z^+ - E_z^-) \delta(z-f) \right] \hat{z} \\
= (n_1^2 - 1) \nabla [\vec{n} \cdot \vec{E}^- \delta(z-f)]. \tag{1.17}
\end{aligned}$$

Unlike for the stratified media case there are only two semi-infinite half spaces. Here the Heaviside function is zero below the rough surface, $f = f(x, y)$, and unity above it and \vec{n} is the surface normal. The expressions

$$\frac{\partial \vec{E}^+}{\partial |\vec{n}|} \text{ and } \frac{\partial \vec{E}^-}{\partial |\vec{n}|}$$

are the derivatives of the electric field with respect to the surface normal as the surface is approached from above and below, respectively.

By applying Green's function and vector identities it is possible to use the boundary condition to re-express the electric field in each layer as a function of the above-surface quantities alone, since this is of greatest interest. The result is

$$h\vec{E} = \vec{E}_s + \left[\vec{R}^+ \delta - |\vec{n}|^2 \vec{E}^+ \delta' \right] * K_{01}, \tag{1.18}$$

and

$$(1-h)\vec{E} = \left[-\vec{R}^- \delta + |\vec{n}|^2 \vec{E}^- \delta' \right] * K_{02}, \tag{1.19}$$

where \vec{E}_s is the source component of the electric field and $K_{01} = e^{-jkr}/4\pi r$ and $K_{02} = e^{-j\gamma r}/4\pi r$. K_{01} and K_{02} are Green's functions for above and below the surface, respectively, $r = \sqrt{x^2 + y^2 + z^2}$ is the distance to the observation point and γ is the

propagation constant below the surface. The notation in these equations has been simplified by defining new vectors

$$\vec{R}^+(x, y) = f_x \left(\frac{\partial \vec{E}^+}{\partial x} \right) + f_y \left(\frac{\partial \vec{E}^+}{\partial y} \right) - \left(\frac{\partial \vec{E}^+}{\partial z} \right)^+ + \frac{\partial}{\partial x}[f_x \vec{E}^+] + \frac{\partial}{\partial y}[f_y \vec{E}^+]$$

and

$$\vec{R}^-(x, y) = f_x \left(\frac{\partial \vec{E}^-}{\partial x} \right) + f_y \left(\frac{\partial \vec{E}^-}{\partial y} \right) - \left(\frac{\partial \vec{E}^-}{\partial z} \right)^- + \frac{\partial}{\partial x}[f_x \vec{E}^-] + \frac{\partial}{\partial y}[f_y \vec{E}^-],$$

where $\delta(z - f)$ is simplified as δ since there is only one interface, f_x and f_y are the partial derivatives of the surface with respect to x and y , respectively. Once the convolutions of (1.18) and (1.19) are carried out, the equations are converted to the spatial frequency domain. After changing the order of the integrals and doing a change of variables it is possible to come up with the two equations that must be solved to determine R^+ and E^+ , the field quantities at the surface when approached from above

$$\int_{x'} \int_{y'} \left[\vec{G}(x', y') + \frac{\vec{F}(x', y')}{u_1} \right] e^{f(x', y')u_1} e^{-jk_x x' - jk_y y'} dy' dx' = 0, z < 0, \quad (1.20)$$

and

$$2u_0 \underline{\vec{E}}_s^{z^-} e^{-z^- u_0} = \int_{x'} \int_{y'} \left[(|\bar{n}|^2 \vec{E}(x', y')) - \frac{\vec{R}^+(x', y')}{u_0} \right] e^{-f(x', y')u_0} e^{-jk_x x' - jk_y y'} dy' dx' = 0, z > 0, \quad (1.21)$$

where $u_1 = \sqrt{k_x^2 + k_y^2 - n_1^2 k^2}$ and the underbar indicates Fourier transform quantities.

To simplify the notation, the expressions $\vec{G}(x', y') = |\vec{n}|^2 \vec{E}^+ - \frac{n_1^2 - 1}{n_1^2} (\vec{n} \cdot \vec{E}^+) \vec{n}$ and $\vec{F}(x', y') = \vec{R}^+ + \frac{n_1^2 - 1}{n_1^2} \nabla_{xy} (\vec{n} \cdot \vec{E}^+)$ have been used and ∇_{xy} is the two dimensional (2D) spatial gradient operator. To solve these equations, Walsh introduces some approximations that require the solution to be bandlimited,

$$|k_x^2 + k_y^2| < k^2, \quad (1.22)$$

and that the refractive index, n_1 , be large with respect to k . The approximation on n_1 is valid for propagation of high frequency (3-30 MHz) radiation across the ocean surface, which was the original application of the research and allows the simplification $u_1 = jkn_1$. To explicitly account for the bandwidth restriction the exponential will be denoted with a subscript L as $e_L^{-f(x', y')u_0}$.

The focus is on finding the principal solution of (1.20) and (1.21), which corresponds to the bandlimited solution. To simplify the notation, we let the lower frequency components of the source, i.e., E_{sx}^+ , E_{sy}^+ , E_{sz}^+ , be represented as g_1 . The expression for g_1 may be expressed as a bandlimited inverse Fourier transform as

$$g_1(x', y') = \frac{1}{4\pi^2} \int_{k'_x} \int_{k'_y} G_{1L}(k'_x, k'_y) e_L^{f(x', y')u'_0} e^{jk_x x' + jk_y y'} dk'_x dk'_y \quad (1.23)$$

where the primed coordinates of the transform variables, k'_x and k'_y are also bandlimited (i.e. $k_x'^2 + k_y'^2 < k^2$). Next, the term within the square brackets of (1.21) is replaced by (1.23). Without loss of generality it is possible to assume the surface roughness $f(x, y)$ is periodic and can be expressed as a Fourier series. Substituting the expression for g_1 into (1.20) and (1.21) results in the term $e_L^{-f(x', y')(u'_0 - u_0)}$. This term will also be periodic and can be expanded as

$$e_L^{-f(x', y')(u'_0 - u_0)} = \sum_n A_n(u'_0 - u_0) e^{jnk_0 y'}. \quad (1.24)$$

This analysis may be extended to random rough surfaces if the Fourier series coefficients, A_n , are taken to be random variables in two spatial dimensions with the period extending to infinity.

From this point on, Walsh [82] notes that the y - and z - components of the scattered field are coupled for a surface only varying in the y direction and only works with those two components. For the original application of propagation across the ocean only the vertical component (i.e., z -component) is significant and the y -component is provided as an example of the horizontal component of the wave. This research considers both scattering from and penetration through the surface and both the y - and z - components of the field are necessary.

The surface has been assumed to have the form

$$f(x, y) = b + a \cos(k_0 y) \tag{1.25}$$

such that f is bounded, but of infinite horizontal extent and $f \geq 0$. Once the surface is defined it is possible to expand (1.24) to find the y - and z - components of the electric field of the source below the surface as

$$\begin{aligned}
2\underline{E}_{sy}^{z^-} e^{-z^- u_0} u_0 &= \sum_q \left\{ \left[u_0 + jkn_1 + \frac{(ak_0)^2}{2} \left(u_0 - \left(\frac{n_1^2 - 1}{n_1^2} \right) u_{0q} \right. \right. \right. \\
&\quad \left. \left. \left. + j \frac{k}{n_1} \right) \right] A_q(u_{0q} - u_0) \right. \\
&\quad + \left(\frac{n_1^2 - 1}{n_1^2} \right) \left(\frac{ak_0}{2} \right) [k_y - (q - 1)k_0] A_{q-1}(u_{0q} - u_0) \\
&\quad - \left(\frac{n_1^2 - 1}{n_1^2} \right) \left(\frac{ak_0}{2} \right) [k_y - (q + 1)k_0] A_{q+1}(u_{0q} - u_0) \\
&\quad + \frac{(ak_0)^2}{4} \left[\left(\frac{n_1^2 - 1}{n_1^2} \right) u_{0q} - \left(u_0 + j \frac{k}{n_1} \right) \right] [A_{q-2}(u_{0q} - u_0) \\
&\quad \left. \left. + A_{q+2}(u_{0q} - u_0) \right] \right\} G_{1y}(k_x, k_y - qk_0) \\
&\quad + \sum_q \left\{ j \left(\frac{n_1^2 - 1}{n_1^2} \right) (k_y - qk_0) A_q(u_{0q} - u_0) \right. \\
&\quad + \left(\frac{n_1^2 - 1}{n_1^2} \right) \left(\frac{ak_0}{2} \right) [ju_{0q} - kn_1] [A_{q-1}(u_{0q} - u_0) \\
&\quad \left. \left. - A_{q+1}(u_{0q} - u_0) \right] \right\} G_{1z}(k_x, k_y - qk_0) \tag{1.26}
\end{aligned}$$

and

$$\begin{aligned}
2\underline{E}_{sz}^{z^-} e^{-z^- u_0} u_0 &= \sum_q \left\{ \left[u_0 + j \frac{k}{n_1} + \frac{(ak_0)^2}{2} (u_0 + jkn_1) \right] \right. \\
&\quad \left. - (u_0 + jkn_1) \frac{(ak_0)^2}{4} (A_{q-2}(u_{0q} - u_0) + A_{q+2}(u_{0q} - u_0)) \right\} G_{1z}(k_x, k_y - qk_0) \\
&\quad + \sum_q \left\{ -kn_1 \left(\frac{n_1^2 - 1}{n_1^2} \right) \left(\frac{ak_0}{2} \right) (A_{q-1}(u_{0q} - u_0) - A_{q+1}(u_{0q} - u_0)) \right\} G_{1y}(k_x, k_y - qk_0), \tag{1.27}
\end{aligned}$$

where $\underline{E}_{sy}^{z^-}$ and $\underline{E}_{sz}^{z^-}$ are the y - and z - components, respectively, of the transforms of the electric field below the surface on the plane $z = z^-$ and the bounds on q are determined by the inequality $k_x^2 + (k_y - qk_0)^2 \leq k^2$. A similar process can be followed

for the scattered fields starting from the transform of the total field above the surface from (1.18), which yields

$$\underline{\vec{E}}^{z^+} = \underline{\vec{E}}_s^{z^+} + \frac{e^{z^+u_0}}{2} \int_{x'} \int_{y'} \left[|\vec{n}|^2 \vec{E} + \frac{\vec{R}^+}{u_0} \right] \cdot e^{fu_0} e^{-jk_x x' - jk_y y'} dy' dx', \quad (1.28)$$

where $\underline{\vec{E}}^{z^+}$ is the total electric field above the surface at $z = z^+$ and $\underline{\vec{E}}_s^{z^+}$ is the electric field of the source above the surface. After some algebra the y - and z - components of the source may be found as

$$\begin{aligned} \underline{E}_y^s = & \frac{e^{-z^+u_0}}{2u_0} \left[\sum_q \left\{ \left[u_0 - jkn_1 + \left(\frac{ak_0}{2} \right) \left(u_0 + \left(\frac{n_1^2 - 1}{n_1^2} \right) u_{0q} - j \frac{k}{n_1} \right) \right] A_q(u_{0q} + u_0) \right. \right. \\ & + \left(\frac{n_1^2 - 1}{n_1^2} \right) \left(\frac{ak_0}{2} \right) [(k_y - (q+1)k_0) A_{q+1}(u_{0q} + u_0) \\ & - (k_y - (q-1)k_0) A_{q-1}(u_{0q} + u_0)] \\ & - \left(\frac{(ak_0)^2}{4} \right) \left[u_0 + \left(\frac{n_1^2 - 1}{n_1^2} \right) u_{0q} - j \frac{k}{n_1} \right] [A_{q-2}(u_{0q} + u_0) \\ & \left. \left. + A_{q+2}(u_{0q} + u_0)] \right\} G_{1y}(k_x, k_y - qk_0) \right. \\ & + \sum_q \left\{ -j \left(\frac{n_1^2 - 1}{n_1^2} \right) (k_y - qk_0) A_q(u_{0q} + u_0) \right. \\ & + \left(\frac{n_1^2 - 1}{n_1^2} \right) \left(\frac{ak_0}{2} \right) (-ju_{0q} + kn_1) [A_{q-1}(u_{0q} + u_0) \\ & \left. \left. - A_{q+1}(u_{0q} + u_0)] \right\} G_{1z}(k_x, k_y - qk_0) \right] \end{aligned} \quad (1.29)$$

and

$$\begin{aligned}
\underline{E}_z^s &= \frac{e^{-z+u_0}}{2u_0} \left[\sum_q \left\{ \left[u_0 - j\frac{k}{n_1} + \left(\frac{(ak_0)^2}{2} \right) (u_0 - jkn_1) \right] A_q(u_{0q} + u_0) \right. \right. \\
&\quad \left. \left. - (u_0 - jkn_1) \left(\frac{(ak_0)^2}{4} \right) [A_{q-2}(u_{0q} + u_0) + A_{q+2}(u_{0q} + u_0)] \right\} G_{1z}(k_x, k_y - qk_0) \right. \\
&\quad \left. + \sum_q \left\{ kn_1 \left(\frac{ak_0}{2} \right) \left(\frac{n_1^2 - 1}{n_1^2} \right) [A_{q-1}(u_{0q} + u_0) \right. \right. \\
&\quad \left. \left. + A_{q+1}(u_{0q} + u_0)] \right\} G_{1y}(k_x, k_y - qk_0) \right], \tag{1.30}
\end{aligned}$$

where \underline{E}_y^s and \underline{E}_z^s are the y - and z - components of the transforms of the scattered field. Although the Fourier series expansion is summed over n terms as per (1.24), the previously listed equations are summed over q using a change of variables to simplify the notation. It can be shown that $A_q(0) = 1$ when $q = 0$ and is zero otherwise. The y -component of the expression for the scattered field from (1.29) may be simplified as

$$\underline{E}_y^s = \frac{e^{-z+u_0}}{2u_0} C_E \left[\sum_q p_q(k_x, k_y) G_{1y}(k_x, k_y - qk_0) + \sum_q r_q(k_x, k_y) G_{1z}(k_x, k_y - qk_0) \right], \tag{1.31}$$

where C_E is a scaling term consisting of the terms u, n_1, k and k_0 , p_q and r_q are the multipliers on components of the principal solution, G_{1y} and G_{1z} , respectively. Next we can consider from (1.26), the contribution from the y -component of the source field, denoted as \underline{E}_{syy} and expressed in terms of the y -component of the principal solution. The summation may be reorganized by pulling out the $q = 0$ term to rewrite as

$$\underline{E}_{syy} = (I + \Sigma)G_{1y}, \tag{1.32}$$

where I is the identity operator and Σ is the summation over all $q \neq 0$. This may be used to set up a Neumann series expansion that is limited to N terms so that the

bandlimiting criterion imposed earlier may be maintained. The equations were also normalized by Walsh, so that some of the matrices involved in the solution will have unity main diagonal entries. By expressing the source and scattered fields in this way, the resulting equations to be solved are

$$\begin{bmatrix} \underline{E}_{sy} \\ \underline{E}_{sz} \end{bmatrix} = \begin{bmatrix} A & B \\ C & D \end{bmatrix} \begin{bmatrix} G_{1y} \\ G_{1z} \end{bmatrix}, \quad (1.33)$$

$$\underline{E}_y^s = \frac{e^{-z^+u_0}}{2u_0} \left[u_0 - jkn_1 + \frac{(ak_0)^2}{2} \left[\left(\frac{2n_1^2 - 1}{n_1^2} \right) u_0 - j\frac{k}{n_1} \right] \right] \begin{bmatrix} G_{1y} \\ G_{1z} \end{bmatrix}^\top \begin{bmatrix} P \\ R \end{bmatrix}, \quad (1.34)$$

and

$$\underline{E}_z^s = \frac{e^{-z^+u_0}}{2u_0} \left[u_0 - j\left(\frac{k}{n_1}\right) + \frac{(ak_0)^2}{2} (u_0 - jkn_1) \right] \begin{bmatrix} G_{1y} \\ G_{1z} \end{bmatrix}^\top \begin{bmatrix} V \\ S \end{bmatrix}, \quad (1.35)$$

where \top indicates transpose. These equations are simplifications of ones presented earlier ((1.26), (1.27), (1.29) and (1.30)) where A , B , C and D are matrices that are the multipliers on G_{1y} and G_{1z} for the source field and P , R , V and S are the multipliers on G_{1y} and G_{1z} for the scattered fields. These equations are valid for any realizable source, but the solutions must be determined numerically. If a plane wave source is assumed as

$$\vec{E}_s = (E_{0y}\hat{y} + E_{0z}\hat{z})e^{-jk_x^\circ - jk_y^\circ - u_0^\circ z} \quad (1.36)$$

it is possible to find a closed form approximation of the scattered fields as

$$\begin{aligned}
E_y^s &= E_{0y} \sum_{q=q^-}^{q=q^+} \left[\frac{u_{0q}^\circ - jkn_1 + \frac{(ak_0)^2}{2} \left(u_{0q}^\circ - \frac{jk}{n_1} \right)}{(u_0^\circ + jkn_1) \left(1 + \frac{(ak_0)^2}{2n_1^2} \right)} \right] \frac{u_0^\circ}{u_{0q}^\circ} \\
&\quad T_q^y[-k_x^\circ, -(k_y^\circ - qk_0)] e^{-jk_x^\circ x - j(k_y^\circ - qk_0)y - ju_{0q}^\circ z^+} \\
&+ E_{0z} \sum_{q=q^-}^{q=q^+} \left[\frac{u_{0q}^\circ - jkn_1 + \frac{(ak_0)^2}{2} \left(\frac{2n_1^2 - 1}{n_1^2} \right) u_{0q}^\circ - \frac{jk}{n_1}}{(u_0^\circ + \frac{jk}{n_1}) + \frac{(ak_0)^2}{2} (u_0^\circ + jkn_1)} \right] \frac{u_0^\circ}{u_{0q}^\circ} \\
&\quad T_q^z[-k_x^\circ, -(k_y^\circ - qk_0)] e^{-jk_x^\circ x - j(k_y^\circ - qk_0)y - ju_{0q}^\circ z^+}, \tag{1.37}
\end{aligned}$$

and

$$\begin{aligned}
E_z^s &= E_{0y} \sum_{q=q^-}^{q=q^+} \left[\frac{u_{0q}^\circ - \frac{jk}{n_1} + \frac{(ak_0)^2}{2} (u_{0q}^\circ - jkn_1)}{(u_0 + kn_1) \left(1 + \frac{(ak_0)^2}{2n_1^2} \right)} \right] \frac{u_0}{u_{0q}^\circ} \\
&\quad U_q^y[-k_x^\circ, -(k_y^\circ - qk_0)] e^{-jk_x^\circ x - j(k_y^\circ - qk_0)y - ju_{0q}^\circ z^+} \\
&+ E_{0z} \sum_{q=q^-}^{q=q^+} \left[\frac{u_{0q}^\circ - \frac{jk}{n_1} + \frac{(ak_0)^2}{2} (u_{0q}^\circ - jkn_1)}{(u_0 + \frac{jk}{n_1}) + \frac{(ak_0)^2}{2} (u_0 + jkn_1)} \right] \frac{u_0}{u_{0q}^\circ} \\
&\quad U_q^z[-k_x^\circ, -(k_y^\circ - qk_0)] e^{-jk_x^\circ x - j(k_y^\circ - qk_0)y - ju_{0q}^\circ z^+}. \tag{1.38}
\end{aligned}$$

In (1.37) the multiplier on E_{0y} is the co-polarized scattering coefficient and the multiplier on E_{0z} is the cross-polarized component and similar statements may be made regarding (1.38). Here T_q^y and T_q^z are symbols used in place of the matrix multiplication of (1.34) and U_q^y and U_q^z are used in place of the matrix multiplication of (1.35). These equations are valid for a single wavenumber pair

$$k_x^\circ = k \cos \theta_x \tag{1.39}$$

and

$$k_y^\circ = k \cos \theta_y \quad (1.40)$$

where the angles θ_x and θ_y are for incidence with respect to the normal to the average surface. As well, $u_{0q}^\circ = \sqrt{(-k_x^\circ)^2 + (-k_y^\circ + qk_0)^2 - k^2}$ and $u_0^\circ = \sqrt{(-k_x^\circ)^2 + (-k_y^\circ)^2 - k^2}$. The terms $T_q^{y,x}$ and $U_q^{y,z}$ are subject to the delta function constraint

$$\begin{aligned} k_x &= -k_x^\circ \\ k_y &= -(k_y^\circ - qk_0). \end{aligned} \quad (1.41)$$

For penetrating radar applications it is common for the radar to point straight downwards, which leads to $\theta_x = \theta_y = 90^\circ$ and $k_x^\circ = k_y^\circ = 0$.

Unlike other methods, Walsh's approach does not rely on assumptions of small surface slopes and small surface heights, however, the solutions for realizable sources (i.e., not plane wave) may require numerical integration. The main assumptions that are made are that the source and scattered field are bandlimited and that the surface has a simple sinusoidal profile. This version of Walsh's rough surface scattering approach also does not take into account path losses and the equations are specific for the chosen surface. The equations must be rederived when another surface is chosen.

1.4 Research Contributions of Thesis

This thesis describes how EM scattering models and sea ice ridge models may be used to distinguish between FY and MY sea ice ridges and each chapter describes developments towards that end. Unlike some theses which contain a collection of contributions in the same research area, this research is a progression towards a single

goal. Thus, each chapter will have only intermediate results and it is in the second last chapter (Chapter 5) that all the work is brought together to assess the feasibility of discriminating between FY and MY ridges. The main research contributions of the thesis are listed with respect to the chapter in which they are described.

Chapter 2 expands on Walsh's scattering approach [82] that was originally intended to model high frequency (HF) radar propagation across the ocean. The main contributions are:

- The rough surface scattering equations are generalized so they are valid for dielectric surfaces and not just good conducting surfaces. For a gently varying surface it may be confirmed that the magnitude of the scattered field is proportional to the refractive index of the surface.
- The rough surface equations are solved for general surface slopes. This was done by correctly accounting for the scattering geometry. It is shown that accounting for the surface slopes affects the shape of the scattered field, but does not have a noticeable impact on the magnitude of the scatter.
- Since the original application was for propagation across the rough surface, the emphasis was on finding the z -component of the scattered field and the y -component was also found as an illustration of the horizontal field. The x -component of the scattered field is derived using the same methodology as was used for the y - and z - components, but the form of the solution is more complicated for the surface considered.

Chapter 3 provides justification for representing sea ice ridges as having a rough surface over stratified media. It is shown to be reasonable to model the rough surface as having a long correlation length and the layers correspond with the physical structure of the ridge. The main developments are:

- The electric field transmitted through the surface is calculated by estimating the field reflected from a perfect electric conductor using an alternate interpretation of the boundary condition at the surface.
- For plane wave incidence, expressions for the Fourier transform and spatial domain scattering may be written in terms of reflection coefficients, once appropriate simplifications are made.
- The scattering equations were rederived for scattering from the underside of the rough surface and similarities with the original equations that simplify the analysis were highlighted.

Chapter 4 provides a background on sea ice and sea ice ridges relevant to scattering at VHF. The main contributions are

- Using existing literature (e.g., [9], [86], [87]), models that represent the structure and properties for FY and MY ridges relevant to scattering at VHF have been developed.
- Changes in ridge characteristics from fall to early spring are documented and used to present a range of parameters that describe FY and MY ridges at different times of year.

Chapter 5 is a synthesis of the previous chapters as the modified scattering models are applied to the developed sea ice ridge model to determine the scattering differences between FY and MY ridges. The main contributions of the research are:

- Simulations are used to show how the scattered field is affected by ice properties such as salinity, thickness, density, temperature, macro-porosity and surface roughness as well as radar frequency.

- Simulations are used to show how the signature of FY and MY ridges changes over time
- For the simple surface geometry chosen, the surface and subsurface scatter are spatially separated and this may be used to distinguish FY and MY ridges. However, due to the high salinity of FY ridges, the total scatter may be used to separate FY and MY ridges. This suggests that it is possible to discriminate between FY and MY ridges regardless of the ridge shape, provided that the surface is gently rough.

Chapter 6 summarizes the research and provides some ideas for future work.

1.5 Contributions to the Literature

Research completed for this thesis has been submitted for publication in journals and presented at international conferences. Conference publications include:

- [88], which covers a portion of Chapter 2;
- [89], which summarizes portions of Chapter 3 to 5; and
- [90], which will be presented in August 2020 and covers portions of Chapters 2, 4 and 5.

One journal paper has been published, [91], which contained material from Chapters 2 and 3. An additional journal paper has been submitted to the IEEE Journal of Oceanic Engineering [92] that is an extension of [89]. Another article has been submitted to MDPI Remote Sensing that is an expanded version of [90]. The journal publications have been prepared to intentionally cut across multiple chapters of the thesis so that some results may be presented in each paper.

Chapter 2

Generalizing Scattering Models for Rough Surfaces

2.1 Introduction

This chapter describes three modifications to the early Walsh approach to rough surface scattering to make the equations more relevant for scattering from sea ice instead of the ocean surface:

1. Sea ice is not a good conductor (the relative dielectric permittivity $\epsilon_r \approx 3 - 6$) and the equations are modified to accommodate scattering from general dielectric surfaces.
2. Sea ice ridges are inherently rough and the equations are updated to include scattering from general surface slopes.
3. The geometry for penetrating radar implies the horizontal components of the scattered field are relevant and the x -component of the field will be determined.

In Chapter 1 it was stated that an early version of Walsh's method [82] is being

used that assumes scattering from a 1D sinusoidal surface. This simplifies the equations considerably and makes it possible to find closed form approximations with a minimum of additional assumptions. Before delving into the details of how to extend Walsh's approach, it is reasonable to consider if the assumptions already made are also valid for scattering from sea ice.

The biggest assumption for this version of Walsh's method is that the surface may be represented by a 1D sinusoid. The results of Chapter 5 show this assumption does not limit the analysis. The second main assumption is that $k_x^2 + (k_y - qk_0)^2 \leq k^2$, which is the Neumann series version of the bandlimited constraint of (1.22). Walsh considers the geometry as shown in Figure 2.1. However, using (1.41) leads to the simplification that $qk_0 \leq |k|$, which may be satisfied by selecting the correct range of q . One of the main implications of this assumption is that it is sufficient to find the principal solution to the scattering, which corresponds to the bandlimited criterion of (1.22). This was justified for good conducting surfaces by considering (1.21) and noting that the integrand will be small when the expression $e^{-f(x',y')u_0}$ is small. Since $f(x, y)$ is bounded, the integrand will be small for large values of u_0 , which corresponds to higher frequency contributions. Thus, it is reasonable to assume the scattered fields are bandlimited, even when the surface permittivity is not large. A discussion of why the scattered field is bandlimited for gently rough surfaces is provided in Appendix A. The remainder of this chapter shows how the field equations have been modified to be more applicable for scattering from sea ice.

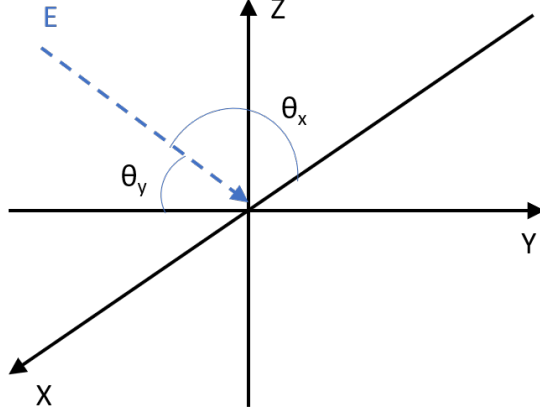


Figure 2.1: Geometry for Walsh scattering approach

2.2 Scatter from a Rough Surface with General Permittivity

Walsh [82] simplifies (1.20) for good conducting surfaces by assuming $u_1 \approx jkn_1$. If this assumption is not made, it is still fairly straight forward to derive the y - and z -components of the scattered field. Considering again (1.20), we know that the integral will be zero when

$$\vec{G}(x', y') + \frac{\vec{F}(x', y')}{u_1} = 0. \quad (2.1)$$

By substituting the values of G and F into (1.20) we can write

$$|\vec{n}|^2 \vec{E} - \frac{n_1^2 - 1}{n_1^2} (\vec{n} \cdot \vec{E}) \vec{n} - \frac{1}{u_1} \left[\vec{R}^+(x', y') + \frac{n_1^2 - 1}{n_1^2} \nabla_{xy} (\vec{n} \cdot \vec{E}) \right] = 0. \quad (2.2)$$

This may be rearranged to yield another expression for \vec{R}^+ , namely

$$\vec{R}^+ = -\frac{n_1^2 - 1}{n_1^2} \nabla_{xy} (\vec{n} \cdot \vec{E}) - u_1. \quad (2.3)$$

Since $\vec{n} = -f_x \hat{x} - f_y \hat{y} + \hat{z}$ and the surface derivatives with respect to x are zero, the

expansion of \vec{R}^+ into its components yields

$$\begin{aligned}
R_x^+ &= -\frac{n_1^2 - 1}{n_1^2} \left[-f_y \frac{\partial E_y^+}{\partial x} \frac{\partial E_z^+}{\partial x} \right] - u_1 [(f_y^2 - 1)E_x^+] \\
R_y^+ &= -\frac{n_1^2 - 1}{n_1^2} \left[f_{yy} E_y^+ - f_y \frac{\partial E_y^+}{\partial y} + \frac{\partial E_z^+}{\partial y} \right] - u_1 \left[\left(1 + \frac{f_y^2}{n_1^2} \right) e_y^+ + f_y \left(\frac{n_1^2 - 1}{n_1^2} \right) E_z^+ \right] \\
R_z^+ &= -u_1 \left[f_y \left(\frac{n_1^2 - 1}{n_1^2} \right) E_y^+ + E_z^+ \left(f_y^2 + \frac{1}{n_1^2} \right) \right]. \tag{2.4}
\end{aligned}$$

This allows us to rewrite (1.20) for the y - and z - components of the field as

$$\begin{aligned}
2u_0 \underline{E}_{sy}^{z-} e^{-z-u_0} &= (u_0 + u_1) \int_{y'} \int_{x'} E_y^+ k_L dx' dy' + \left(u_0 + \frac{u_1}{n_1^2} \right) \int_{y'} \int_{x'} f_y^2 E_y^+ k_L dx' dy' \\
&\quad - \frac{n_1^2 - 1}{n_1^2} \int_{y'} \int_{x'} f_{yy} E_y^+ k_L dx' dy' - \frac{n_1^2 - 1}{n_1^2} \int_{y'} \int_{x'} f_y \frac{\partial E_y^+}{\partial y} k_L dx' dy' \\
&\quad + u_1 \frac{n_1^2 - 1}{n_1^2} \int_{y'} \int_{x'} f_y E_z^+ k_L dx' dy' + \frac{n_1^2 - 1}{n_1^2} \int_{y'} \int_{x'} \frac{\partial E_z^+}{\partial y} k_L dx' dy' \tag{2.5}
\end{aligned}$$

and

$$\begin{aligned}
2u_0 \underline{E}_{sz}^{z-} e^{-z-u_0} &= \left(u_0 + \frac{u_1}{n_1^2} \right) \int_{y'} \int_{x'} E_z^+ k_L dx' dy' + (u_0 + u_1) \int_{y'} \int_{x'} f_{y'}^2 E_z^+ k_L dx' dy' \\
&\quad + u_1 \frac{n_1^2 - 1}{n_1^2} \int_{y'} \int_{x'} f_{y'} E_y^+ k_L dx' dy', \tag{2.6}
\end{aligned}$$

where $k_L = e_L^{-f(x',y')u_0} e^{-jk_x x' - jk_y y'}$ and the subscript L explicitly indicates that the frequencies are bandlimited.

The expressions in (2.5) and (2.6) may be rewritten using the Fourier series expansion of (1.24) with the surface as defined in (1.25). After some algebra, the equations may be simplified to

$$\begin{aligned}
2\underline{E}_{sy}^{z^-} e^{-z^-u_0} u_0 &= \sum_q \left\{ \left[u_0 + u_1 + \frac{(ak_0)^2}{2} \left(u_0 - \left(\frac{n_1^2 - 1}{n_1^2} \right) u_{0q} + \frac{u_1}{n_1^2} \right) \right] A_q(u_{0q} - u_0) \right. \\
&+ \left(\frac{n_1^2 - 1}{n_1^2} \right) \left(\frac{ak_0}{2} \right) [k_y - (q - 1)k_0] A_{q-1}(u_{0q} - u_0) \\
&- \left(\frac{n_1^2 - 1}{n_1^2} \right) \left(\frac{ak_0}{2} \right) [k_y - (q + 1)k_0] A_{q+1}(u_{0q} - u_0) \\
&+ \left. \frac{(ak_0)^2}{4} \left[\left(\frac{n_1^2 - 1}{n_1^2} \right) u_{0q} - \left(u_0 + \frac{u_1}{n_1^2} \right) \right] [A_{q-2}(u_{0q} - u_0) + A_{q+2}(u_{0q} - u_0)] \right\} \\
&G_{1y}(k_x, k_y - qk_0) \\
&+ \sum_q \left\{ j \left(\frac{n_1^2 - 1}{n_1^2} \right) (k_y - qk_0) A_q(u_{0q} - u_0) \right. \\
&+ \left. \left(\frac{n_1^2 - 1}{n_1^2} \right) \left(\frac{ak_0}{2} \right) [ju_{0q} + ju_1] [A_{q-1}(u_{0q} - u_0) - A_{q+1}(u_{0q} - u_0)] \right\} G_{1z}(k_x, k_y - qk_0)
\end{aligned} \tag{2.7}$$

and

$$\begin{aligned}
2\underline{E}_{sz}^{z^-} e^{-z^-u_0} u_0 &= \sum_q \left\{ \left[u_0 + \frac{u_1}{n_1^2} + \frac{(ak_0)^2}{2} (u_0 + u_1) \right] \right. \\
&- (u_0 + u_1) \frac{(ak_0)^2}{4} (A_{q-2}(u_{0q} - u_0) + A_{q+2}(u_{0q} - u_0)) \left. \right\} G_{1z}(k_x, k_y - qk_0) \\
&+ \sum_q \left\{ ju_1 \left(\frac{n_1^2 - 1}{n_1^2} \right) \left(\frac{ak_0}{2} \right) (A_{q-1}(u_{0q} - u_0) - A_{q+1}(u_{0q} - u_0)) \right\} G_{1y}(k_x, k_y - qk_0),
\end{aligned} \tag{2.8}$$

where the expressions G_{1y} and G_{1z} are defined as in (1.23). These expressions for the transform of the source below the surface have the same form as the equations derived by Walsh and are listed in (1.26) and (1.27), however, (2.7) and (2.8) are valid for surfaces with general permittivities. Following Walsh's approach and using (1.28) it

is possible, after some algebra, to find the expressions for the y - and z - components of the scattered field:

$$\begin{aligned}
\frac{E_y^s}{2u_0} &= \frac{e^{-z+u_0}}{2u_0} \left[\sum_q \left\{ \left[u_0 - u_1 + \left(\frac{ak_0}{2} \right) \left(u + \left(\frac{n_1^2 - 1}{n_1^2} \right) u_q - \frac{u_1}{n_1^2} \right) \right] A_q(u_q + u_0) \right. \right. \\
&+ \left(\frac{n_1^2 - 1}{n_1^2} \right) \left(\frac{ak_0}{2} \right) [(k_y - (q + 1)k_0)A_{q+1}(u_q + u_0) - (k_y - (q - 1)k_0)A_{q-1}(u_q + u_0)] \\
&- \left. \left. \left(\frac{(ak_0)^2}{4} \right) \left[u_0 + \left(\frac{n_1^2 - 1}{n_1^2} \right) u_q - \frac{u_1}{n_1^2} \right] [A_{q-2}(u_q + u_0) + A_{q+2}(u_q + u_0)] \right\} \right. \\
&G_{1y}(k_x, k_y - qk_0) \\
&+ \sum_q \left\{ -j \left(\frac{n_1^2 - 1}{n_1^2} \right) (k_y - qk_0) A_q(u_q + u_0) \right. \\
&+ \left. \left. \left(\frac{n_1^2 - 1}{n_1^2} \right) \left(\frac{ak_0}{2} \right) (-ju_q - ju_1) [A_{q-1}(u_q + u_0) - A_{q+1}(u_q + u_0)] \right\} G_{1z}(k_x, k_y - qk_0) \right] \\
&\tag{2.9}
\end{aligned}$$

and

$$\begin{aligned}
\frac{E_z^s}{2u_0} &= \frac{e^{-z+u_0}}{2u_0} \left[\sum_q \left\{ \left[u_0 - \frac{u_1}{n_1^2} + \left(\frac{(ak_0)^2}{2} \right) (u_0 - u_1) \right] A_q(u_q + u_0) \right. \right. \\
&- (u_0 - u_1) \left(\frac{(ak_0)^2}{4} \right) [A_{q-2}(u_q + u_0) + A_{q+2}(u_q + u_0)] \left. \right\} G_{1z}(k_x, k_y - qk_0) \\
&+ \sum_q \left\{ kn_1 \left(\frac{ak_0}{2} \right) \left(\frac{n_1^2 - 1}{n_1^2} \right) [A_{q-1}(u_q + u_0) + A_{q+1}(u_q + u_0)] \right\} G_{1y}(k_x, k_y - qk_0) \left. \right]. \\
&\tag{2.10}
\end{aligned}$$

Once again, the expressions for the scattered field for a general surface permittivity have the same structure as Walsh's expressions. It may be shown that the general expressions for the source and scattered fields may be found simply by replacing $jk n_1$

by u_1 , jk/n_1 by u_1/n_1^2 and $-kn_1$ by ju_1 . Substituting expressions for G_1 using the process outlined in (1.33) to (1.35) it is possible to find the scattering equations for a general source to be

$$\underline{E}_y^s = e^{-z^+u_0} \sum_{q=q^-}^{q=q^+} \left[\frac{u_0 - u_1 + \frac{(ak_0)^2}{2} \left(u_0 \frac{2n_1^2 - 1}{n_1^2} - \frac{u_1}{n_1^2} \right)}{(u_{0q} + u_{1q}) \left(1 + \frac{(ak_0)^2}{2} \frac{1}{n_1^2} \right)} \right] \frac{u_{0q}}{u_0} T_q^y(k_x, k_y) (\underline{E}_{sy}^{z^-} e^{-z^-u_0})^q \quad (2.11)$$

and

$$\underline{E}_z^s = e^{-z^+u_0} \sum_{q=q^-}^{q=q^+} \left[\frac{u_0 - \frac{u_1}{n_1^2} + \frac{(ak_0)^2}{2} (u_0 - u_1)}{(u_{0q} + u_{1q}) \left(1 + \frac{(ak_0)^2}{2} \frac{1}{n_1^2} \right)} \right] \frac{u_{0q}}{u_0} U_q^y(k_x, k_y) (\underline{E}_{sy}^{z^-} e^{-z^-u_0})^q, \quad (2.12)$$

where u_{0q} is the q th mode of u_0 or $u_{0q} = \sqrt{k_x^2 + (k_y - qk_0)^2 - k^2}$ and u_{1q} is the q th mode of u_1 . Following the same steps as Walsh [82] it is possible to determine an approximation to the scattered field for a plane wave source in closed form. To simplify the equations, the source is assumed to have only a y -component to make it easier to identify the co-polarized and cross-polarized fields. For a general dielectric surface the scattered field equations are:

$$E_y^s = E_{0y} \sum_{q=q^-}^{q=q^+} \left[\frac{u_{0q}^\circ - u_1^\circ + \frac{(ak_0)^2}{2} \left(u_{0q}^\circ - \frac{u_1^\circ}{n_1^2} \right)}{(u_0^\circ + u_1^\circ) \left(1 + \frac{(ak_0)^2}{2n_1^2} \right)} \right] \frac{u_0^\circ}{u_{0q}^\circ} T_q^y[-k_x^\circ, -(k_y^\circ - qk_0)] e^{-jk_x^\circ x - j(k_y^\circ - qk_0)y - ju_{0q}^\circ z^+} \quad (2.13)$$

and

$$E_z^s = E_{0y} \sum_{q=q^-}^{q=q^+} \left[\frac{u_{0q}^\circ - \frac{u_1^\circ}{n_1^2} + \frac{(ak_0)^2}{2}(u_{0q}^\circ - u_1^\circ)}{(u_0 + kn_1) \left(1 + \frac{(ak_0)^2}{2n_1^2}\right)} \right] \frac{u_0}{u_{0q}^\circ} U_q^y[-k_x^\circ, -(k_y^\circ - qk_0)] e^{-jk_x^\circ x - j(k_y^\circ - qk_0)y - ju_{0q}^\circ z^+}. \quad (2.14)$$

It may be observed that, due to the Neumann series expansion, the scattered field is now expressed as a sum of plane waves. These modified equations are valid for scattering from surfaces with general permittivities but may be used to reproduce the simulations for the good conductor case, as illustrated in Figure 2.2. As expected, the updated equations are not restricted to low permittivity surfaces and simulations of the more general method are equivalent with Walsh's results when the same parameters are used. Figure 2.3 shows simulations with two different refractive indices. It can be seen that a higher refractive index leads to greater scattering from the surface, which implies lower transmission through the surface. The relationship between the scattered and transmitted fields will be discussed further in Chapter 3. The simulations have been conducted with a 'gently rough' surface with a surface wavelength of 20 m. For very rough surfaces with short correlation lengths the surface roughness dominates the scattering behaviour and the refractive index does not have a noticeable impact [93]. Unless otherwise stated, all simulations and analysis from this point on will be based on slowly varying surfaces that have a general refractive index.

2.3 Removing the Small Slope Assumption

As stated earlier, Walsh's method does not intrinsically place restrictions on the source, surface heights or surface slope. However, not surprisingly, the choice of these parameters has an impact on the ease of the solution. We have already seen

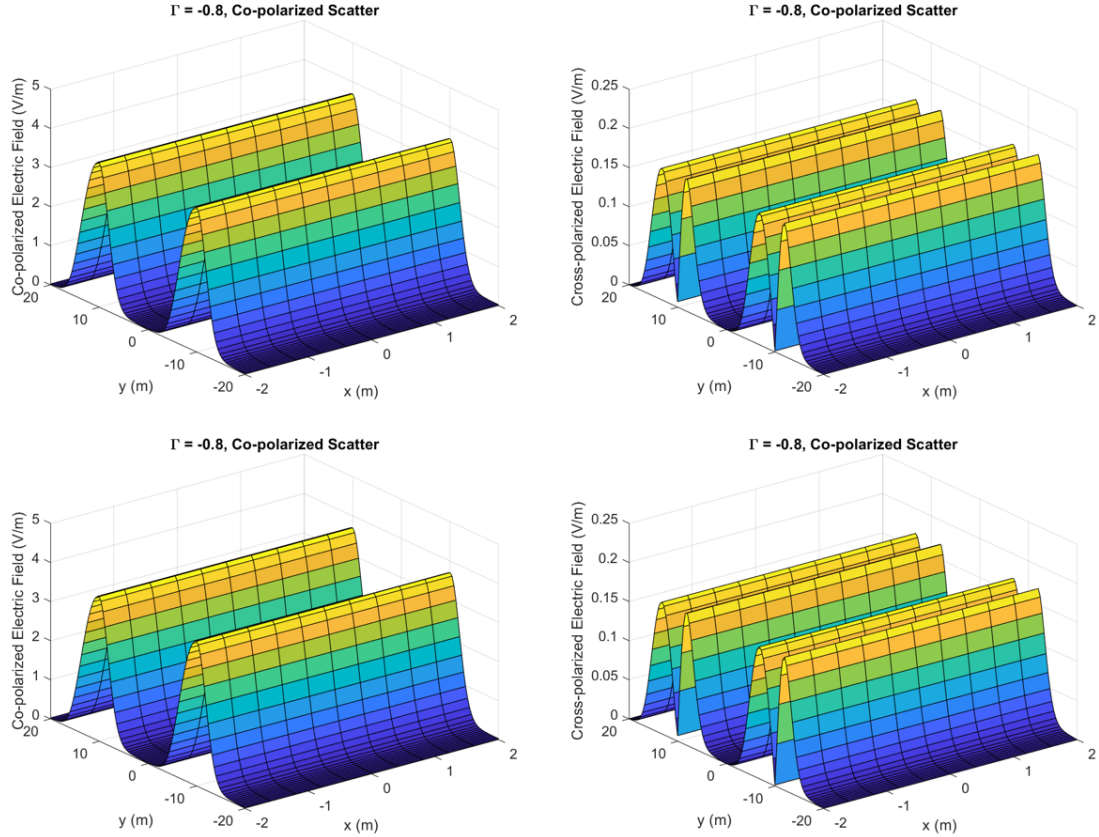


Figure 2.2: Magnitude of co-polarized (left) and cross-polarized (right) fields for good conductor (top) and general surface (bottom). In both cases the simulation parameters are the same and the simulations are indistinguishable.

that using a plane wave source allows for an approximation to the scattered field to be found in closed form. It is apparent from (1.39) and (1.40) that the angles measured from the source to the surface impact the wavenumber for valid solutions. Walsh [82] uses the geometry of Figure 2.1 and measures θ_x and θ_y with respect to the x and y axes. This approach implicitly assumes a flat surface and results in the small slope assumption. Measuring the angles with respect to the rough surface as illustrated in Figure 2.4, removes the small slope assumption.

For nadir incidence, as assumed for this study, the angles with respect to the surface only depend on surface slope, $-\nabla f$. Since the surface is assumed to vary only

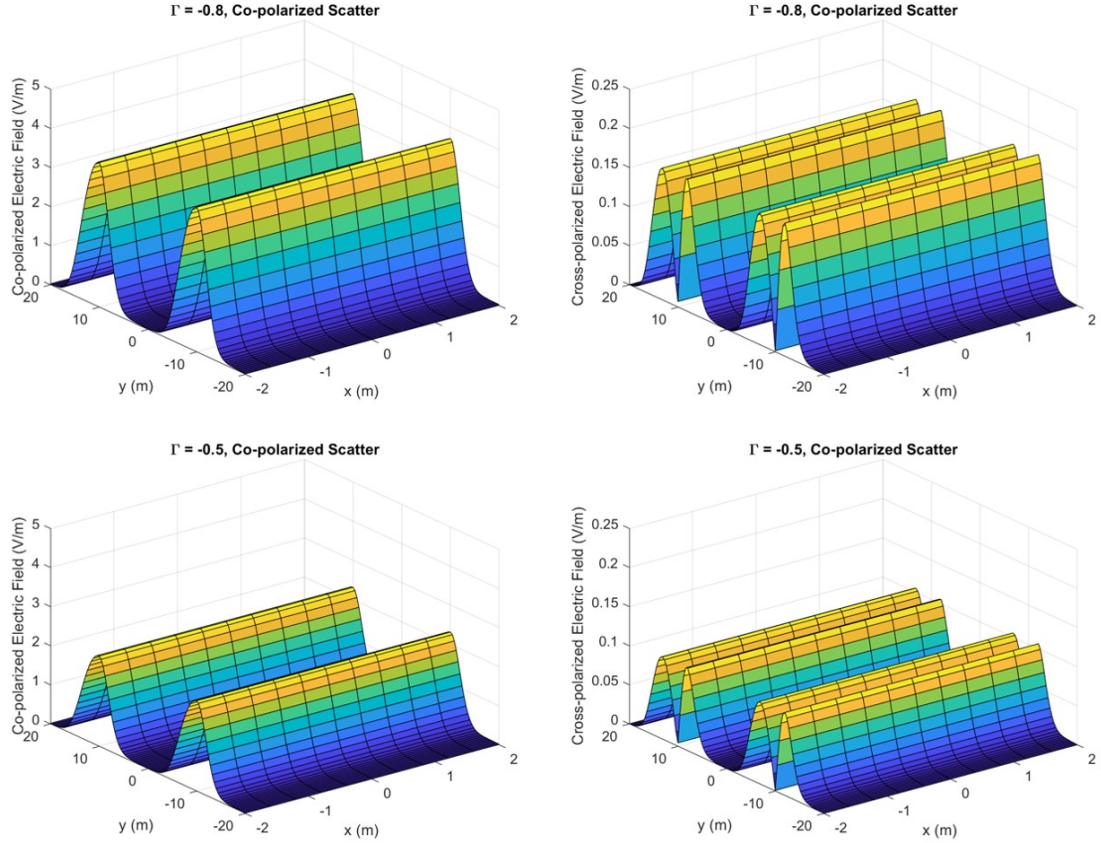


Figure 2.3: Magnitude of co-polarized (left) and cross-polarized (right) fields for general dielectric surface for $n_1 = 9$ (top) and $n_1 = 3$ (bottom) refractive index

in the y -direction, we find that

$$\begin{aligned}\theta_x &= \pi/2 \\ \theta_y &= \tan^{-1} \frac{1}{ak_0 \sin(k_0 y)}.\end{aligned}\tag{2.15}$$

This approach is not limited to the simple surface being considered for this study, but may be applied to a general source over a random rough surface. In the general case the angles θ_x and θ_y will be a function of the surface slope and radar incidence angle.

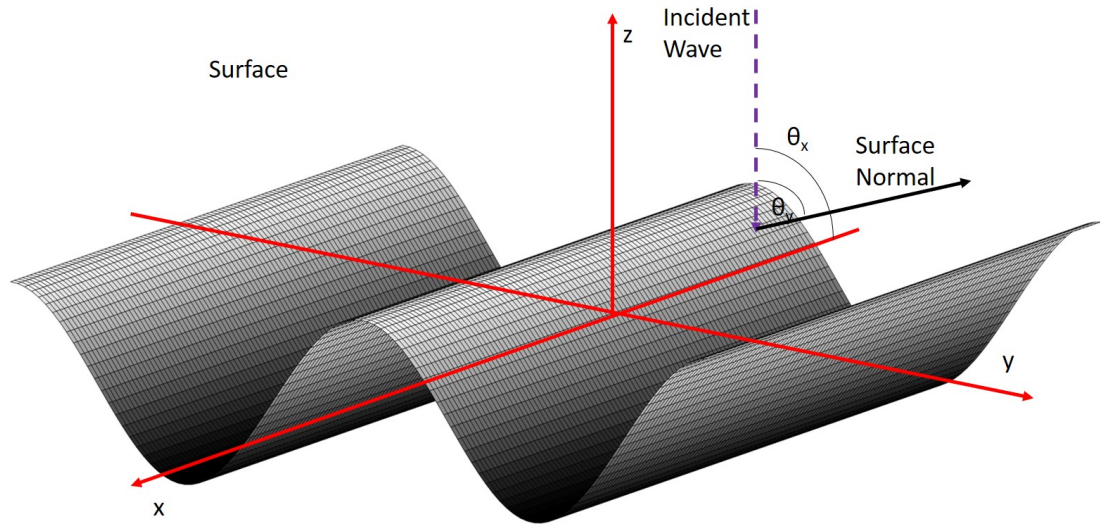


Figure 2.4: Geometry of scattering angles

Removing the small slope assumption has an impact on the shape of the scattered field. Figure 2.5 shows the co-polarized portion of the scattered field when the small slope assumption is made for two different amplitudes of the surface variation. It can be seen that the shape of the scattered field remains the same while the magnitude of the scattered field drops. This is expected since for normal incidence the greatest scatter will occur for a smooth surface and surface roughness will reduce the strength of the scattered field. When surface slope is considered, as shown in Figure 2.6, the shape of the scattered field shows no apparent change when the amplitude of the surface variation is $a = 0.2$, but when the surface amplitude is higher, $a = 0.8$, the slope of the scattered field is sharper and appears to saturate at the maximum amplitude achieved when small slopes are assumed. Key parameters for the simulations are given in the title, where Γ refers to the reflection coefficient from a smooth surface based on the contrast in the refractive index. The value $\Gamma = -0.5$ corresponds to $n_1 = 3$, when the upper medium is freespace. Although the small slope assumption

does not impact the peak magnitude of the scattered field, the total scattered energy is greater when small slopes have not been assumed. The small slope assumption will be removed for all simulations discussed from this point onwards.

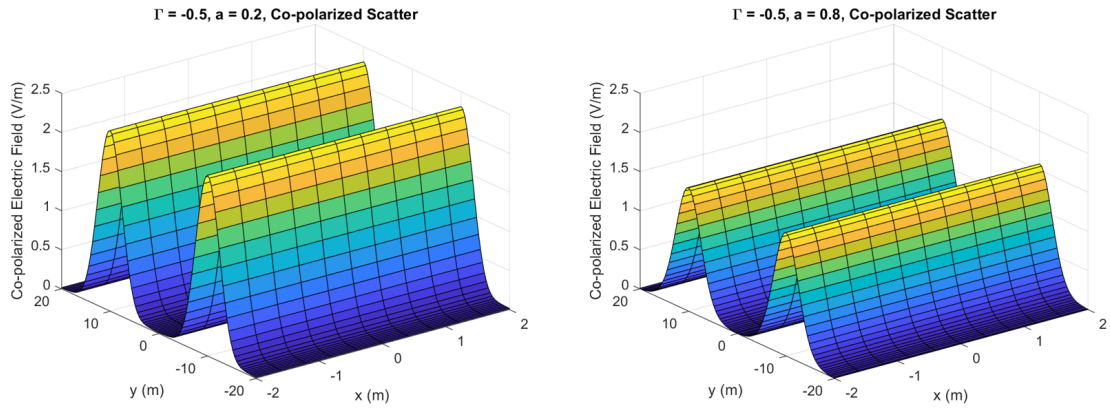


Figure 2.5: Field scattered from rough surface using small slope assumption

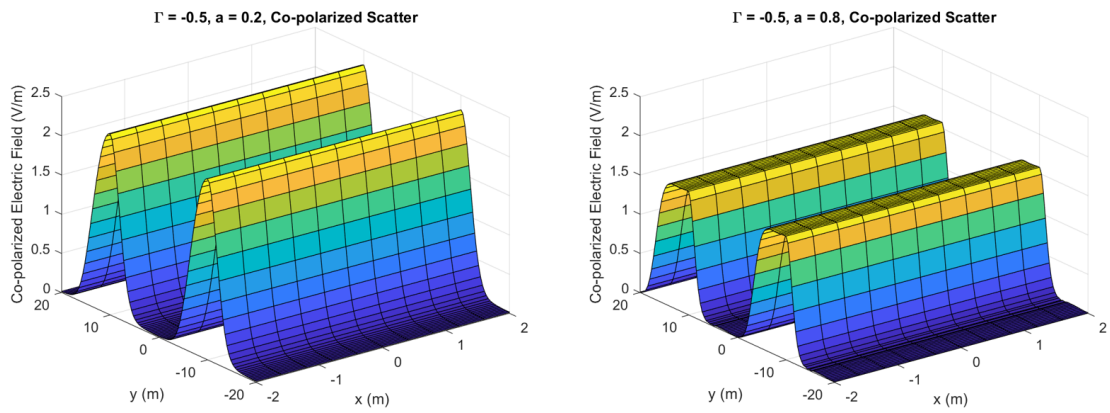


Figure 2.6: Field scattered from rough surface with small slope assumption removed

2.4 Deriving the x -Component of the Scattered Field

The analysis to this point has followed Walsh's derivations [82] and has focused on determining the y - and z - components of the scattered field since they are coupled for the choice of surface and are representative of the horizontal and vertical fields. For penetrating radar applications it may also be valuable to determine the x -component of the scattered field. Since the surface only varies in the y direction, the x -component of the field is simpler than the y -component of the field, but the form of the solution is slightly different and is worth investigating.

Beginning with the R_x^+ from (2.4) and using (1.20) it is possible after some algebra to write

$$\begin{aligned}
2\underline{E}_{sx}^{z^-} e^{-z^- u_0} u_0 &= \sum_q \left\{ A_q(u_{0q} - u_0) \left[(u_0 + u_1) \left(1 + \frac{(ak_0)^2}{2} \right) \right] - \frac{(ak_0)^2}{4} (u_0 + u_1) \cdot \right. \\
&\quad \left. [A_{q+2}(u_{0q} - u_0) + A_{q-2}(u_{0q} - u_0)] \right\} G_{1x}(k_x, k_y - qk_0) \\
&+ \sum_q \left(\frac{n_1^2 - 1}{n_1^2} \right) \left(\frac{ak_0}{2} \right) [A_{q-1}(u_{0q} - u_0) - A_{q+1}(u_{0q} - u_0)] \cdot \\
&\quad G_{1y}(k_x, k_y - qk_0) \\
&+ \sum_q \left(\frac{n_1^2 - 1}{n_1^2} \right) (jk_x) A_q(u_{0q} - u_0) G_{1z}(k_x, k_y - qk_0). \tag{2.16}
\end{aligned}$$

A similar process may be followed to derive the expression for the scattered field as

$$\begin{aligned}
\underline{E}_x^s &= \frac{e^{-z+u_0}}{2u_0} \left[\sum_q \left\{ \left[(u_0 - u_1) \left(1 + \frac{(ak_0)^2}{2} \right) \right] A_q(u_{0q} + u_0) - (u_0 - u_1) \left(\frac{(ak_0)^2}{4} \right) \right. \right. \\
&\quad \left. \left. [A_{q-2}(u_{0q} + u_0) + A_{q+2}(u_{0q} + u_0)] \right\} G_{1x}(k_x, k_y - qk_0) \right. \\
&\quad + \sum_q \left\{ \left(-\frac{n_0^2 - 1}{n_0^2} \right) \frac{ak_0}{2} [A_{q-1}(u_{0q} + u_0) - A_{q+1}(u_{0q} + u_0)] G_{1y}(k_x, k_y - qk_0) \right. \\
&\quad \left. \left. + \sum_q \left\{ \left(-\frac{n_0^2 - 1}{n_0^2} \right) jk_x A_q(u_{0q} + u_0) \right\} G_{1z}(k_x, k_y - qk_0) \right\} \right]. \tag{2.17}
\end{aligned}$$

The expressions for the x -component of the source and scattered fields are derived in a similar fashion and have the same structure as the y - and z - components of the fields, except the x - components of the fields are a function of the x -, y - and z - components of the source. As before, the source field may be expressed as

$$\underline{E}_{sxx} = (I + \Sigma)G_{1x} \tag{2.18}$$

where I is the identity operator and Σ includes the summation terms for $q \neq 0$. A Neumann series expansion, $(I + \Sigma)^{-1} = I - \Sigma + \Sigma^2 - \Sigma^3 + \dots$, can be used to solve for G_1 . This allows the expression for each component of G_1 to be expressed as a matrix equation. For the simple 1D surface discussed here, the y - and z - component equations are coupled and are not dependent on the x -component, but the full general equation may be given as

$$\begin{bmatrix} \underline{E}_{sx} \\ \underline{E}_{sy} \\ \underline{E}_{sz} \end{bmatrix} = \begin{bmatrix} \alpha_{xx} & \alpha_{xy} & \alpha_{xz} \\ \alpha_{yx} & \alpha_{yy} & \alpha_{yz} \\ \alpha_{zx} & \alpha_{zy} & \alpha_{zz} \end{bmatrix} \begin{bmatrix} G_{1x} \\ G_{1y} \\ G_{1z} \end{bmatrix}. \tag{2.19}$$

The elements α_{xx} , α_{xy} and α_{xz} in the first matrix on the right hand side of (2.19) are

the multipliers on G_{1x} , G_{1y} , G_{1z} from (2.16). Similarly, the remaining two rows of that matrix correspond to the multipliers on the components of G_1 for the y - and z -components of the source field. For the chosen surface, both $\alpha_{yx} = \alpha_{zx} = 0$. Since the source terms will be known in (2.19), matrix inversion yields the unknown G_1 terms. Expressions for the scattered fields can then be written and the x -component is

$$\underline{E}_x^s = \frac{e^{-z^+u_0}}{2u_0} \left[(u_0 - u_1) \left(1 + \frac{(ak_0)^2}{2} \right) \right] \begin{bmatrix} G_{1x} \\ G_{1y} \\ G_{1z} \end{bmatrix}^\top \begin{bmatrix} \rho_x \\ \rho_y \\ \rho_z \end{bmatrix}. \quad (2.20)$$

Here the ρ_x , ρ_y and ρ_z are the respective multipliers on G_{1x} , G_{1y} , G_{1z} from (2.17), and similar expressions can be found for the y - and z - components of the scattered fields. Using (2.19) it is possible to express the x -component of the scattered field in terms of the source as

$$\underline{E}_x^s = \frac{e^{-z^+u_0}}{2u_0} \left[(u_0 - u_1) \left(1 + \frac{(ak_0)^2}{2} \right) \right] \begin{bmatrix} \underline{E}_s^x \\ \underline{E}_s^y \\ \underline{E}_s^z \end{bmatrix}^\top \left(\begin{bmatrix} \alpha_{xx} & \alpha_{xy} & \alpha_{xz} \\ \alpha_{yx} & \alpha_{yy} & \alpha_{yz} \\ \alpha_{zx} & \alpha_{zy} & \alpha_{zz} \end{bmatrix}^\top \right)^{-1} \begin{bmatrix} \rho_x \\ \rho_y \\ \rho_z \end{bmatrix}. \quad (2.21)$$

For calculation purposes, it is more convenient to express (2.21) in terms of $(\underline{E}_{sx})^q e^{-z^-}$, $(\underline{E}_{sy})^q e^{-z^-}$ and $(\underline{E}_{sz})^q e^{-z^-}$, which are the modes of the source below the surface at $z = z^-$ and the source terms are

$$\begin{aligned}
(\underline{E}_{sx})^q &= e^{-z^+u_0} \sum_{q=q^-}^{q^+} \frac{2(\underline{E}_{sx}^{z^-} e^{-z^-u_0})u_{0q}}{(u_0 + u_{1q})(1 + \frac{(ak_0)^2}{2})} \\
(\underline{E}_{sy})^q &= e^{-z^+u_0} \sum_{q=q^-}^{q^+} \frac{2(\underline{E}_{sy}^{z^-} e^{-z^-u_0})u_{0q}}{(u_{0q} + u_{1q})[1 + \frac{(ak_0)^2}{2} \frac{1}{n_0^2}]} \\
(\underline{E}_{sz})^q &= e^{-z^+u_0} \sum_{q=q^-}^{q^+} \frac{2(\underline{E}_{sz}^{z^-} e^{-z^-u_0})u_{0q}}{u_{0q} + \frac{u_{1q}}{n_0^2} + \frac{(ak_0)^2}{2}(u_{0q} + u_{1q})}. \tag{2.22}
\end{aligned}$$

The x -component of the scattered field expressed as modes of the source may be written as

$$\begin{aligned}
\underline{E}_x^s &= e^{-z^+u_0} \sum_{q=q^-}^{q^+} \left[\frac{(u_0 - u_1) \left(1 + \frac{(ak_0)^2}{2}\right)}{(u_{0q} + u_{1q})(1 + \frac{(ak_0)^2}{2})} \right] \frac{u_{0q}}{u_0} T_q^x(k_x, k_y) (\underline{E}_{sx}^{z^-} e^{-z^-u_0})^q \\
&+ e^{-z^+u_0} \sum_{q=q^-}^{q^+} \left[\frac{(u_0 - u_1) \left(1 + \frac{(ak_0)^2}{2}\right)}{(u_{0q} + u_{1q})(1 + \frac{(ak_0)^2}{2} \frac{1}{n_0^2})} \right] \frac{u_{0q}}{u_0} T_q^y(k_x, k_y) (\underline{E}_{sy}^{z^-} e^{-z^-u_0})^q \\
&+ e^{-z^+u_0} \sum_{q=q^-}^{q^+} \left[\frac{(u_0 - u_1) \left(1 + \frac{(ak_0)^2}{2}\right)}{u_{0q} + \frac{u_{1q}}{n_0^2} + \frac{(ak_0)^2}{2}(u_{0q} + u_{1q})} \right] \frac{u_{0q}}{u_0} T_q^z(k_x, k_y) (\underline{E}_{sz}^{z^-} e^{-z^-u_0})^q \tag{2.23}
\end{aligned}$$

where T_q is the multiplication of the last two matrices of (2.21). The scattered field may be expressed in terms of scattering coefficients as

$$\underline{E}_x^s = \frac{e^{-z^+u_0}}{2u_0} \left[\sum_q s_{xx}^q G_{1x}(k_x, k_y - qk_0) + \sum_q s_{xy}^q G_{1y}(k_x, k_y - qk_0) + \sum_q s_{xz}^q G_{1z}(k_x, k_y - qk_0) \right]. \tag{2.24}$$

The definitions of the scattering coefficients given by s_{xx}^q , s_{xy}^q and s_{xz}^q are apparent from (2.17) and are in terms of the modes of the source. The co-polarized component of the scatter is indicated by s_{xx} and the cross-polarized portions of the signal are represented by s_{xy} and s_{xz} . These scattering coefficients indicate the proportion of

the scattered field from the surface in each direction and the sum of the scattering coefficients indicates the total proportion of scattered energy. Expression (2.23) is an extension of Walsh's results in that it applies to general non-conducting surfaces without a small slope assumption and is for the x -component of the wave.

2.5 Summary

This chapter directly builds on the Walsh scattering approach [82] and updates the model to be valid for scattering from a rough ice surface. The scattering model was enhanced to accommodate surfaces with general permittivities and general slopes. An expression was also developed for the x -component of the scattered field, which is useful for sources such as the field from a horizontal dipole, which may be used for penetrating through the surface. The following chapter describes how to calculate the scattering from sea ice ridges when they are modeled as a rough surface over homogeneous, isotropic layers.

Chapter 3

Modeling scatter from sea ice ridges represented as rough surfaces above stratified media

3.1 Introduction

The previous chapter showed how Walsh's existing rough surface scattering model may be updated to be appropriate for sea ice scatter using a penetrating radar. This chapter addresses the next two questions. First, what is a reasonable physical model for representing sea ice ridges and second, how can we model the scatter from sea ice ridges? For this research, sea ice ridges are represented as a rough surface over stratified media and justifications for this approach are provided. The modification of Walsh's rough surface scattering model has been discussed in Chapter 2 and will be used with Walsh's stratified media scattering model [83], [84]. More details on the specific characteristics of FY and MY ridges are provided in Chapter 4.

3.2 Ridges as Rough Surfaces

3.2.1 Roughness Criteria

Surface roughness depends on the nature of the surface variations, the wavelength of the EM field and the local angle of incidence. Several metrics may be used to describe surface roughness [94], but the two most common metrics are the standard deviation of surface height, σ_h , and correlation length, l_c . The value of σ_h may be calculated using standard formulas for standard deviation and l_c is the self similarity of the surface and is defined as the distance at which the autocorrelation of the surface drops below $1/e$ or 36.9%, where e is the base of the natural logarithm. The correlation length is a measure of variation on the horizontal scale and indicates the statistical independence of two points on the surface [95]. Rayleigh suggested that surfaces are smooth when the path difference between incident waves, $\Delta\phi$, is less than $\pi/2$, which corresponds to surface height variations of $\sigma_h < \lambda/8 \cos\theta$, where θ is the incidence angle of the EM field and λ is the EM wavelength. Norton suggested that the choice of $\pi/2$ was arbitrary and that path differences must be within $\pi/4$ [96] or $\pi/8$ [97] for a surface to be considered smooth.

It has been suggested that surface roughness also depends on the separate cases of scattering from the surface or transmission through the surface [98]. As with the Rayleigh and Norton approaches, the criterion for surface roughness depends on the path difference introduced by the surface roughness. The Rayleigh roughness parameter for reflection, Ra_r , and transmission, Ra_t , are used to determine if the surface is smooth, slightly rough or very rough. The incidence angle plays a major role in determining the degree of roughness and a surface which is rough for reflection may be smooth for transmission for one viewing geometry and vice versa for another incidence angle. Surfaces are considered slightly rough for $Ra_r, Ra_t > \pi/16$ and very

rough for $Ra_r, Ra_t > \pi/C_R$, where C_R is a constant selected between 2 and π . The expressions for the Rayleigh roughness parameter are (as found, for example, in [98])

$$\begin{aligned} Ra_r &= k_1 \sigma_h \cos \theta_i \\ Ra_t &= k \sigma_h \frac{|n_0 \cos \theta_i - n_1 \cos \theta_t|}{2}, \end{aligned} \quad (3.1)$$

where the subscripts 0 and 1 refer to the above and below surface quantities, respectively, k_1 is the radar wavenumber below the surface, θ_i is the incidence angle and θ_t is the transmission angle.

Surface roughness is relevant as it determines the balance between coherent and incoherent scatter. The average intensity of the scattered field, $\langle |\vec{E}^s|^2 \rangle$, can be expressed as the sum of the coherent, $|\langle \vec{E}^s \rangle|^2$, and incoherent, $|\langle \delta \vec{E}^s \rangle|^2$, intensities. For fully coherent scatter, as from an infinite, smooth, flat surface, the scattered field is dominated by the specular component. For scatter from a very rough surface the incoherent scatter term dominates and all other cases would have a balance between coherent and incoherent scatter.

As will be seen in Section 3.6, calculating the field transmitted down through the ice will involve an incoherent sum of the fields scattered from the surface and from the subsurface. Since ice penetrating radar would typically operate at normal incidence and at moderate heights above the surface it cannot be assumed that the surface is very rough.

Wadhams [99] has developed an exponential model to describe sea ice ridge sail height distributions, but for this analysis full surface details are not needed. Instead, three different roughness scales are considered that correspond to the dimensions of the blocks in the sail and the overall sail height and the coherence at those scales is

illustrated in Figure 3.1. A more complete description of ridge geometry is provided in Chapter 4. It may be noted, for the geometry and surface roughness considered in this study, the surface is very rough above 100 MHz for reflection from the surface. For transmission, it can be seen that ice ridges will not be rough for $\sigma_h = 0.4$ m until 275 MHz or 425 MHz and that a roughness of $\sigma_h = 0.8$ m is needed to have a rough surface for all frequencies above 100 MHz. It is interesting to note that with 0.4 m surface variation, the surface would be considered rough for transmission at 100 MHz using the standard Rayleigh criterion.

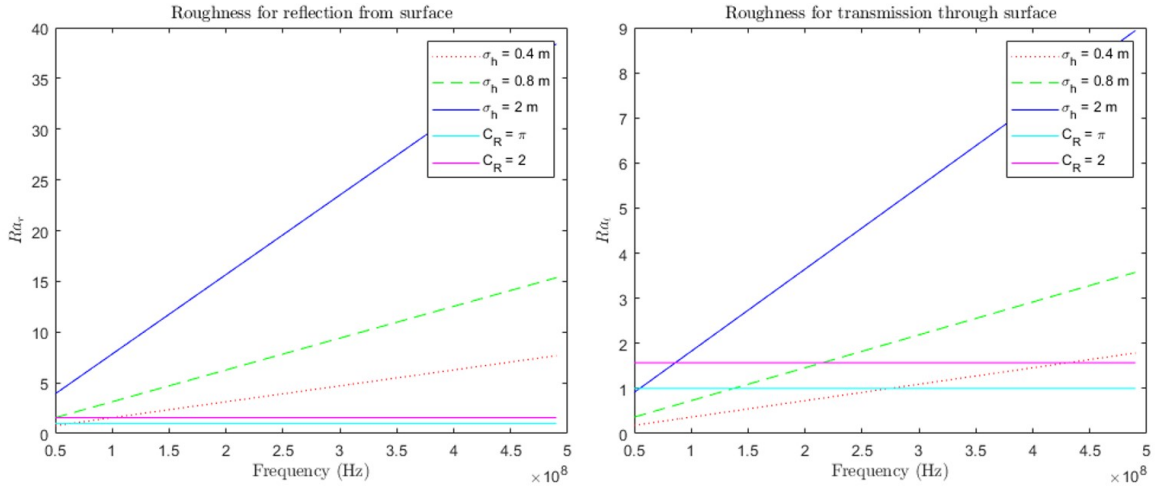


Figure 3.1: Surface roughness effect on Rayleigh roughness parameters

3.2.2 Sea Ice Ridge Roughness

Sea ice ridges are rough, but the reason for the roughness may be different for FY and MY features. The roughness of FY ridges can be due to the prominent ice blocks that are visible in the sail, the arrangement of the blocks or the ridge itself as a perturbation from the level ice surface. Melt and refreeze cycles consolidate MY ridges so that individual blocks are no longer visible. Similar to FY ridges, the entire

MY ridge can be considered a deviation from the level ice surface. Differential melt also causes the topography of MY ridges to be rough.

The heights of hundreds of thousands of surface features were collected using lidar [1] and the most frequently occurring heights of FY and MY features were recorded as 0.45 m, but average heights were nominally greater for MY features. However, it is likely that snow features were recorded in addition to ridges. One way snow features may be excluded is by specifying a cutoff height [100]. One of the issues with this approach is that the same ridge may be counted multiple times. A more robust method is to apply the Rayleigh criterion in which a ridge is identified as a peak above a certain threshold that is surrounded by troughs half the height of the peak [101]. However, the reliance on a fixed cutoff height still naturally biases measurements to larger ridges.

Despite the towering dimensions of some ridges, they are generally composed of thin and medium FY ice and the maximum ridge height is determined by the thickness and strength of the ice sheet [102]. The aspect ratio (length to thickness) of the ice blocks varies from two [103] to five [20], [104].

A comprehensive literature review of field studies of FY ridges indicated that of the data collected, the average ridge height was 1.96 m and the average ridge width was 12 m with maximum widths of 40 m [2]. It is reasonable to expect that MY ridges have similar statistics. FY ridges that last two or more summer melt seasons are smaller than when they were FY ridges, but larger FY ridges are more likely to persist to become MY ridges. The roughness scales of Figure 3.1 are consistent with topography measurements made over first year and multiyear ice regimes in the central Arctic and Beaufort/Chukchi Sea areas [1]. The maximum roughness scale used may also correspond to ridge height [2].

Correlation length may be estimated based on ridge width. Several researchers

have noted that ridge sails may be modeled as triangles (e.g., [105], [106], [2], [107]), making it easy to calculate l_c . Local topography variations due to the arrangements of ice blocks in FY sails and differential melt in MY sails are assumed to dominate the roughness height variations in the 100–500 MHz range. At these frequencies the EM wavelength will be larger than the typical size of blocks in FY sails and will not have an impact on the scattering. Due to the large variability in ridge heights, widths and surface topography, ridge dimensions are not reliable metrics for separating FY and MY ridges. Further details on sea ice ridge roughness are discussed in Section 4.3.1.

3.3 Ridges as Stratified Media

Sea ice ridges are created through chaotic processes and appear to have a random structure. Walsh’s scattering theory for stratified media requires that the layers are homogeneous and isotropic, which does not seem to apply to sea ice ridges. Nonetheless, it is possible to simplify sea ice profiles as being stratified with minimal impact on scattering. Researchers at Cold Regions Research and Engineering Laboratory (CRREL) [4] collected ice penetrating radar signatures over second year ridges and validated the radar data using ice cores collected at 1 m intervals with ice properties calculated and measured every 0.1 m of depth. For illustrative purposes, the salinity and brine volume profiles at one site are shown below in Figure 3.2. Models to calculate the ice parameters are presented in [9] and will be discussed further in Chapter 4.

It is apparent from the salinity profile of Figure 3.2 that there are three distinct regions. For the first two metres of the ridge, the salinity has a mid-level average value with high variability. From 2 to 3 m the average salinity is low with low

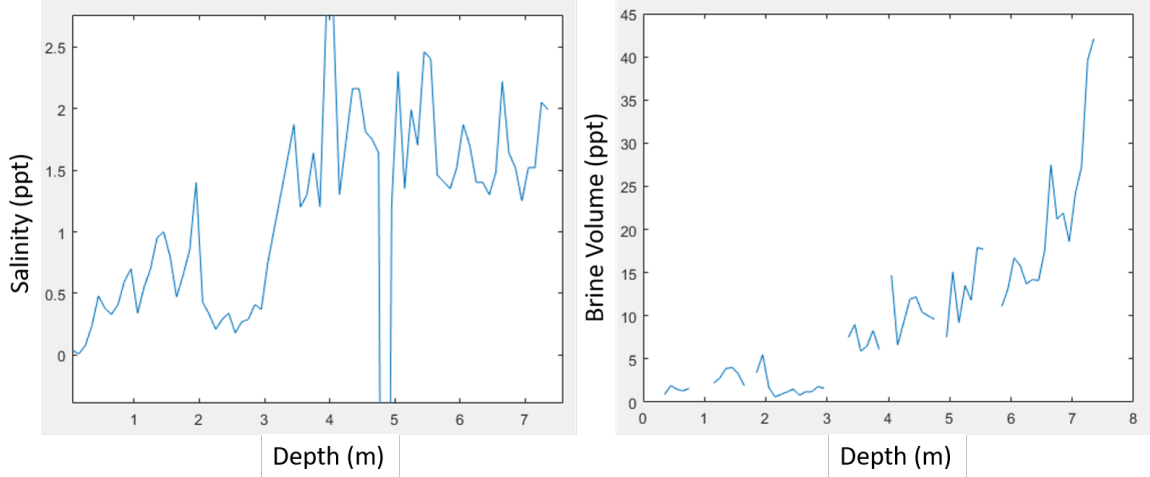


Figure 3.2: Salinity and brine volume for a second year ridge

variability and the remainder of the ridge has high salinity that is highly variable. At first glance comparing the salinity profile with Figure 1.2, it appears that these three layers correspond to the sail, consolidated layer and rubble. It is known that the top layer corresponds to the sail, however, the authors do not provide information on the consolidated layer. One additional link between the physical model and the ice properties may be observed from the brine volume plot. Although there are some gaps in the calculated brine volume from the original publication, the same three layers may be observed plus an extra layer at the bottom of the ridge where the value rapidly increases. The final layer likely corresponds to the skeletal layer at the ridge bottom. The skeletal layer is a lattice of weak ice a few centimeters thick that undergoes advective transfer with the sea water [62], but does not have any noticeable effect on scattering at VHF [58].

In general, sea ice ridge profiles are more complex than the data presented in Figure 3.2, but as we shall see in Chapter 4, there are some general characteristics of ridges that make it possible to justify such a simple modeling approach. When there is no discernible pattern in the parameters, each individual measurement may

be considered a separate layer. Another factor to consider based on experience from field studies is that a discrete change of 40% in the relative permittivity is required to generate a weak reflection [108]. The Fresnel reflection coefficient, Γ , may be calculated for normal incidence as

$$\Gamma = \frac{n_{upper} - n_{lower}}{n_{upper} + n_{lower}}, \quad (3.2)$$

where the subscripts *upper* and *lower* refer to a pair of adjacent layers in the ice. Assuming a minimum change of 30% in the relative permittivity and applying (3.2) corresponds to a reflection coefficient of approximately $\Gamma = 8\%$, and this does not take into account attenuation of the signal as it propagates through the lossy sea ice.

The salinity and brine volume profile data of Figure 3.2 were used with other measurements to calculate the relative permittivity. Using the criterion that a 30% change in the permittivity must be present for an observable reflection, Figure 3.3 shows that the relative permittivity does not vary significantly enough to generate any significant reflections from the internal ice structure. The flat line for the right plot of Figure 3.3 shows that all the permittivity values are within $\pm 30\%$ of a central value.

Sea ice ridges often have air voids between ice blocks, large brine pockets or unfrozen sea water and partially frozen ice and may be covered in wet or dry snow. These materials may cause a stronger contrast in the permittivity resulting in stronger reflections and higher attenuation. The sea water at the bottom of the ridge will also cause a strong reflection. An approach for dealing with these factors and others will be addressed in Chapter 4, but for now it is reasonable to consider sea ice ridges as having a rough surface over stratified media. Further details on the structure of sea ice ridges are discussed in Sections 4.3.1 and 4.6.

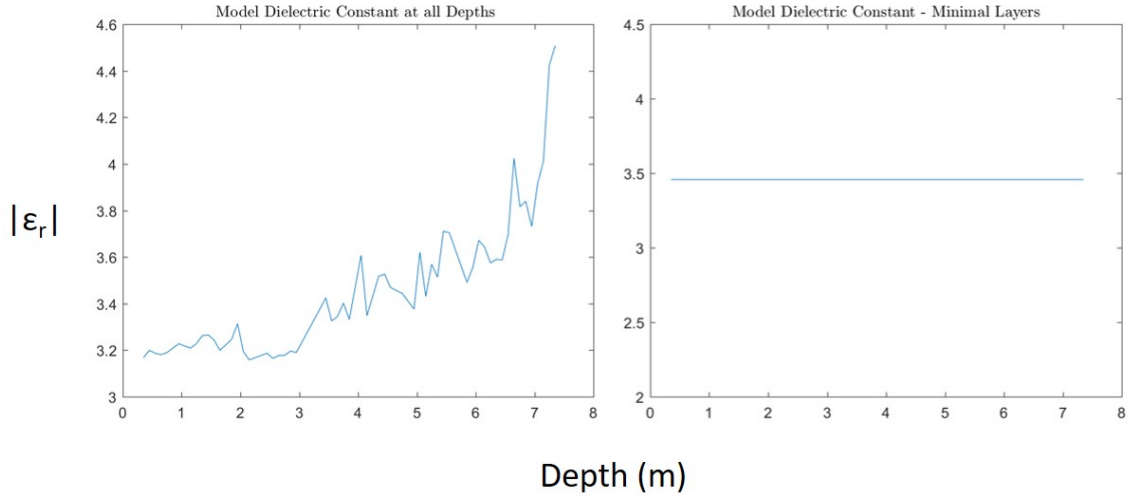


Figure 3.3: Effective reflections from sea ice ridge

3.4 Analysis Overview

Unlike Walsh’s work on propagation across the ocean surface, the work described in this research considers penetration of radar waves through the surface at normal incidence, as illustrated in Figure 3.4.

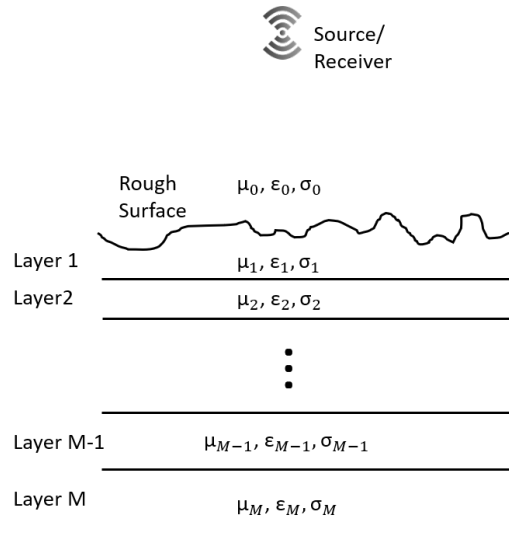


Figure 3.4: Rough surface over layers

In the figure the source is located in free space above the rough surface and the

conductivity, permittivity, and permeability, are specified for each of the M layers. The total scattered field above the surface will be a combination of the field scattered directly from the surface and the portion scattered from the subsurface or layered media which succeeds in exiting the rough surface. Walsh's equations assume a far field approximation and since the field transmitted through the rough surface is expressed in terms of a sum of plane waves, the far field approximation is satisfied. Multiple reflections between the layers are possible but are ignored for this research due to the high salinity of the ice (see Section 4.5.6). Figure 3.5 illustrates the scattering and transmission events that contribute to the total scattered field. The remainder of this chapter will describe how these scattering components are calculated. The direct scatter from the surface may be calculated from the rough surface scattering model previously developed and will be discussed in Section 3.5. Since the surface is not necessarily a good conductor, a non-negligible amount of the electric field will penetrate down through the surface, as described in Section 3.6, and will be scattered from the layers, as detailed in Section 3.7. Section 3.8 has a description of how the field scattered from the layers is scattered up through the underside of the rough surface. Section 3.9 details how the scattered field will be transmitted back through the surface and a simulation of the total scattered field is provided. The final section contains concluding remarks and ideas for future work.

It is important to note that the scattering model implemented does not account for spreading losses and it is not possible to determine calibrated radar cross sections of the ice types. As well, the scattering model does not consider the rough surface and stratified media to be horizontally bounded so edge effects are not included in the analysis. This is not expected to be an issue since the objective of the research is not to model the scattering from sea ice ridges, but to determine the scattering differences between FY and MY ridges. Since the same limitations or constraints are

applied to each ice type, the differences in the scattering will be preserved.

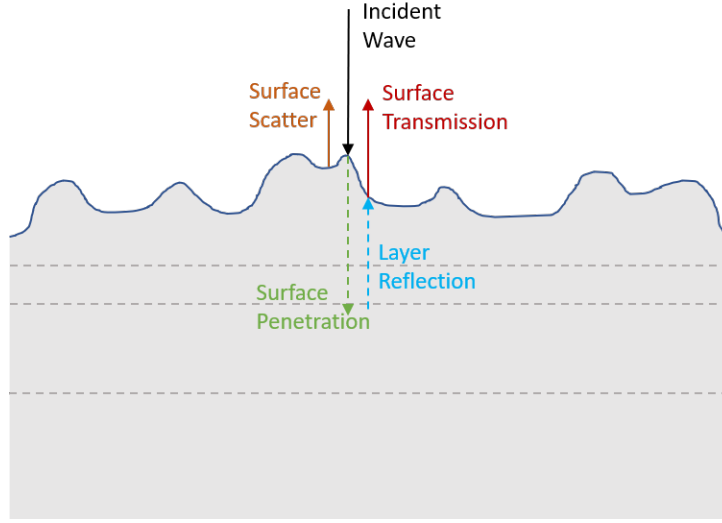


Figure 3.5: Rough surface over layers

3.5 Direct-Surface Scatter

Walsh's approach for scattering from a rough surface was outlined in Chapter 1 and updates to the theory were described in Chapter 2. To simplify the analysis, only the coupled y - and z - components of the scattered field will be considered and the source will be assumed to have y -component only so that it will be easier to identify the co-polarized and cross polarized fields:

$$E_s = E_{0y} e^{-jk_x^\circ x - jk_y^\circ y + u_0^\circ z} \quad (3.3)$$

with Fourier transform

$$\underline{E}_s = 4\pi^2 E_{0y} e^{u_0^\circ z} \delta(k_x + k_x^\circ) \delta(k_y + k_y^\circ). \quad (3.4)$$

The delta functions in (3.4) make it is easy to inverse transform the expressions

in (2.11) and (2.12) to obtain the fields in the spatial domain as given in (2.13) and (2.14). It is possible to express (2.13) and (2.14) in terms of scattering coefficients as

$$E_y^s = E_{0y} \sum_{q=q^-}^{q^+} s_{yy}^q e^{-jk_x^{\circ}x - j(k_y^{\circ} - qk_0) - u_{0q}^{\circ}z} \quad (3.5)$$

and

$$E_z^s = E_{0y} \sum_{q=q^-}^{q^+} s_{zy}^q e^{-jk_x^0x - j(k_y^0 - qk_0) - u_q^0z}, \quad (3.6)$$

where s_{yy}^q is the q th mode of the co-polarized scattering coefficient and s_{zy}^q is the q th mode of the cross-polarized scattering coefficient. The expressions in (3.5) and (3.6) offer a convenient notation useful for determining the total scattered field from the rough surface over layers, as discussed in Section 3.9.2.

3.6 Transmission Down through the Rough Surface

As seen in the previous section, Walsh's method [82] may be used to find the rough surface scattering equations. Since the surface does not absorb any energy the boundary conditions at the surface must be satisfied, allowing us to write the well-known relationship

$$1 + \Gamma = \mathcal{T}, \quad (3.7)$$

where Γ is the reflection coefficient from the surface and \mathcal{T} is the transmission coefficient through the surface. If the reflection coefficient is purely imaginary, a variation of (3.7) is needed [109] to ensure that the phase shift from reflection does not introduce unrealistic amplitudes at the interface, and the expression is

$$\mathcal{T}\mathcal{T}^* = 1 + \Gamma\Gamma^* \quad (3.8)$$

where (*) indicates the complex conjugate and the expression may be obviously rewritten as $|\mathcal{T}|^2 = 1 + |\Gamma|^2$. For lossy surfaces it is apparent that from (3.8) it is only possible to determine $|\mathcal{T}|$ and the phase of the transmitted wave cannot be recovered. For the case of lossy media, the reflection coefficients will be complex, which leads to

$$\mathcal{T}\mathcal{T}^* = (1 + \Gamma)(1 + \Gamma)^*. \quad (3.9)$$

This discussion is relevant since now the scattering equations, (2.13) and (2.14), have been simplified and the modal scattering coefficients from expressions (3.5) and (3.6) may be considered as modal reflection coefficients.

Walsh's expression for the scattered field involves a summation over the expansion modes, resulting in an array of scattering coefficients for both co-polarization and cross-polarization. Thus, it will not be possible to directly apply (3.9) since each mode will not satisfy the equation as it is written. The modal scattering coefficients are complex and the magnitudes of sample scattering coefficients are plotted with respect to q in Figure 3.6 where it may be observed that the values are symmetric about $q = 0$ and the scattering coefficients are larger when $|q|$ is close to zero. In general, the magnitude of the scattering coefficients will be symmetrical, but they may be offset with respect to $q = 0$ depending on the value of k_y .

The standard relationship between reflection and transmission appearing in (3.9) implies, by the presence of the '1', that the reference is the incident field. However, the incident field is not known for each mode. The equation may be easily reorganized as $\mathcal{T}\mathcal{T}^* = (\Gamma - (-1))(\Gamma - (-1))^*$. Since it is known that $\Gamma = -1$ for reflection from a perfect electric conductor (PEC) it is possible to write $\mathcal{T}\mathcal{T}^* = (\Gamma - \Gamma_{PEC})(\Gamma - \Gamma_{PEC})^*$,

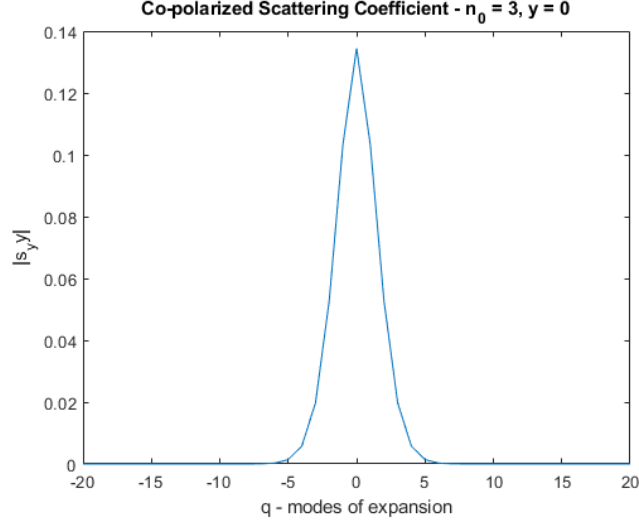


Figure 3.6: Scattering coefficients when $\Gamma = -0.5$ for a simple rough surface

or in terms of the modal expansion

$$\mathcal{T}_q \mathcal{T}_q^* = (\Gamma_q - \Gamma_{q,PEC})(\Gamma_q - \Gamma_{q,PEC})^*, \quad (3.10)$$

where $\Gamma_{q,PEC}$ is the modal scattering coefficient for scattering from a perfect electric conductor. The reference is now explicitly taken to be the reflection from a perfect electric conductor. Unfortunately, it is not possible to use Walsh's scattering equations directly to find the reflection from a perfect electric conductor as there are nonlinearities in the scattering model for very high refractive indices. Figure 3.7 is a plot of the scattered field when $\Gamma = -0.5$ and $\Gamma = -0.99$ and differences between the plots may be observed. The peak intensity should be just less than two times higher when $\Gamma = -0.99$, but it is approximately 2.1 times higher. In addition, the shapes of the curves are different, and the plot with $\Gamma = -0.99$ has sharper peaks and troughs. Figure 3.8 shows how the magnitudes of the modal scattering coefficients change as a function of Γ . It may be seen that $|s_{yy}|$ is noticeably non-linear for $\Gamma > 0.95$, confirming that it is not possible to use this method to generate reliable

scattering coefficients for reflection from a perfect electric conductor. This is possibly a side effect of the assumptions made to simplify the analysis. Of the approximately 40 modal scattering coefficients used in the plots in Figure 3.7, only the strongest ones are visible in the plots appearing in Figure 3.8. The weakest modal scattering coefficients, corresponding to values of q far from the central value, do not follow this same linear relationship, but their impact on the scattered field is orders of magnitude smaller, provided that there are a sufficient number of expansion modes (i.e., the correlation length of the surface is sufficiently long. Further details are provided in Appendix A).

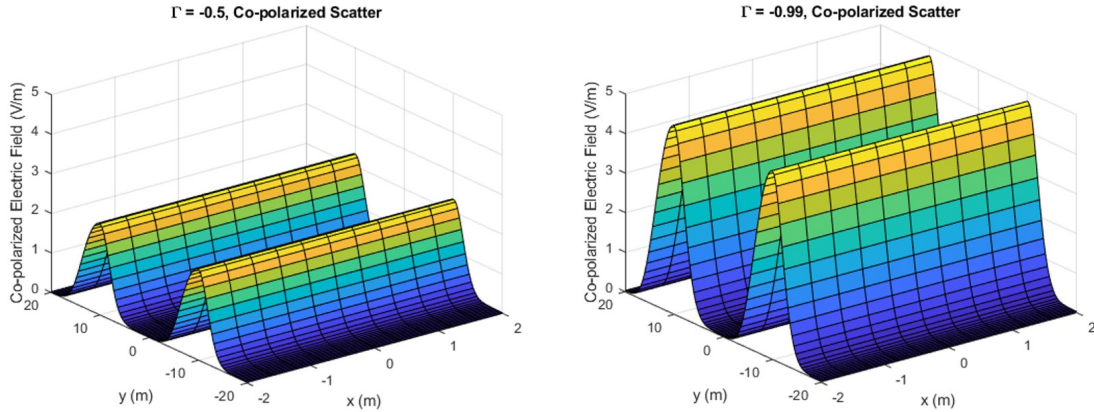


Figure 3.7: Co-polarized scatter when $\Gamma = -0.5$ (left) and $\Gamma = -0.99$ (right)

It has been shown [88] that the the magnitude of the scattered field is proportional to the overall reflection coefficient, when the reflection coefficient is calculated in the standard manner assuming non-magnetic media as per (3.2), where in this case the upper layer corresponds to air and the lower layer refers to the top layer of the ice.

It may also be shown that the modal scattering coefficients are proportional to the overall reflection coefficient for the gentle roughness used. For example, $|s_{yy}|_{\Gamma=-0.8} = 1.6|s_{yy}|_{\Gamma=-0.5}$ for all significant values of q . This specific case is illustrated in Figure 3.9 for the reflection coefficients and Figure 3.10 for the scattered field, which confirms that the reflection coefficients can be scaled within the linear region of Figure 3.8.

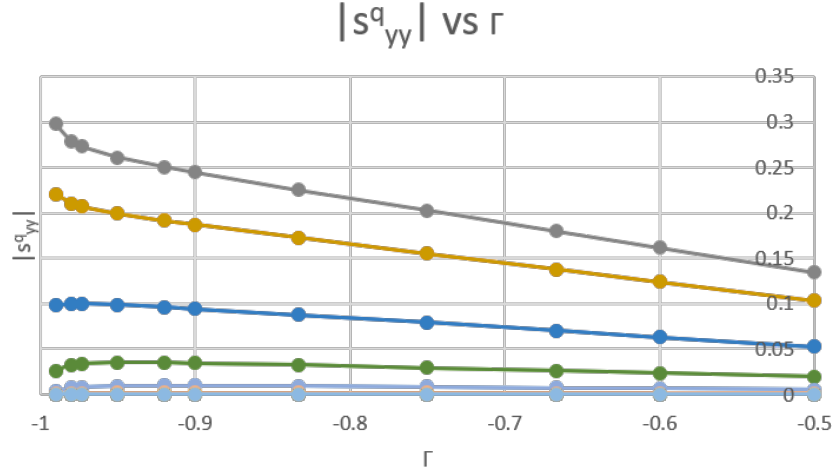


Figure 3.8: Co-polarized modal scattering coefficients vs reflection coefficient ($|s_{yy}^q|$ vs Γ). There is a separate trace for each value of q

For this research it is being proposed that the scattering coefficients for $\Gamma = -1$ may be found by extrapolating from the linear portion of the s_{yy} vs Γ relationship. Mathematically this can be expressed as

$$s_{x_1x_2}^q|_{PEC} = \frac{1}{p} s_{x_1x_2}^q|_{\Gamma=p} \quad (3.11)$$

where x_1x_2 represents any polarization combination, for example yy or zy and p is the reflection coefficient in the linear range of the s_{yy} vs Γ relationship for valid q . For convenience, only real values of p have been used to determine the modal reflection coefficients for a perfect electric conductor. It should be noted that it is only reasonable to extrapolate from the linear portion of the s_{yy} vs Γ plot when the wavelength of the surface variation is sufficiently large. Recall that $k_x^2 + (k_y - qk_0)^2 \leq k^2$ so that for a fixed EM frequency as the wavelength of the surface variation decreases, $q_{max} - q_{min}$ also goes down. When this happens, the modal scattering coefficients for q close to q_{max} or q_{min} are no longer insignificant and scattering coefficients for large values of q are still not linearly scalable. Thus, the scattering coefficients and the

scattered field are not linearly scalable for all length scales of the surface variation. This is consistent with previous work [93] that indicated for very rough surfaces the scattering will be dominated by the surface roughness, not the refractive index of the surface. Simulations have shown for an EM frequency of 300 MHz ($\lambda = 1$ m) the surface wavelength should be no smaller than 7.5 m to avoid non-linear effects for values of q far from the central q . Further illustration of this point is provided in Appendix A. Ridge sails have an average width of 12 m [2] and are often represented as triangles and a triangle is similar in shape to a half wavelength of a sinusoid. Thus, the restriction on the surface wavelength will not affect modeling of sea ice ridges. Unless otherwise specified, simulations have been carried out with $k_0 = 0.313$, which corresponds with a surface wavelength of approximately 20 m. Further details showing the impact of surface roughness on the validity of the analysis is provided in Appendix A.

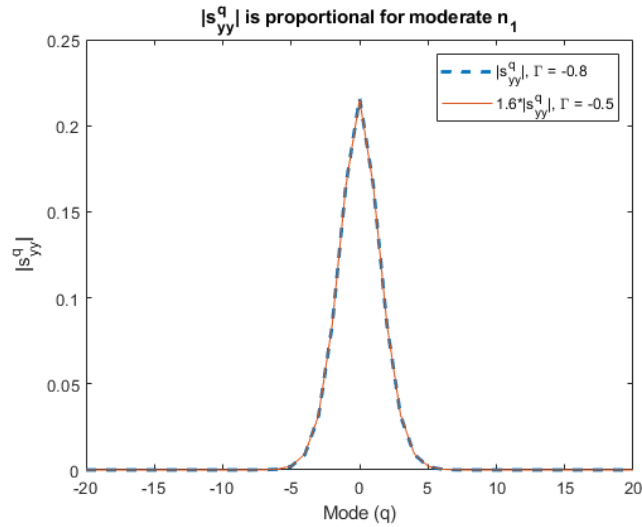


Figure 3.9: Modal co-polarized scattering coefficients when $\Gamma = -0.5$ (scaled) and $\Gamma = -0.8$

An example of the co-polarized scatter from and transmission through the surface when the magnitude of the incident radiation is $E_{0y} = 5$ V/m is given in Figure 3.11.

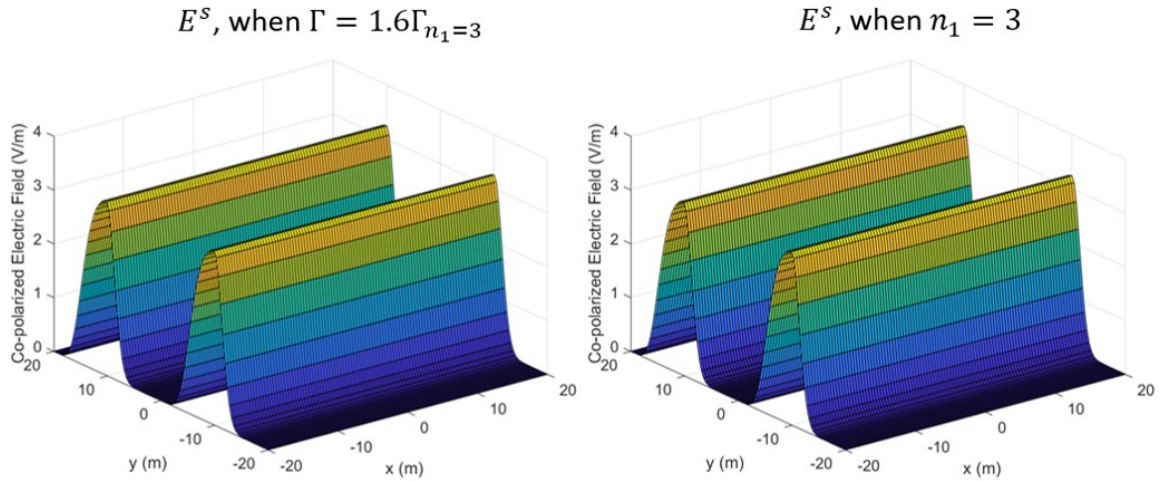


Figure 3.10: Co-polarized scattered field may be scaled for Γ in linear range

The proportions of surface scatter and transmission through the surface are due to the surface refractive index and surface roughness. It is apparent that the scattered and transmitted fields are inversely related with peaks in the scattered field corresponding to troughs in the transmitted field and vice versa.

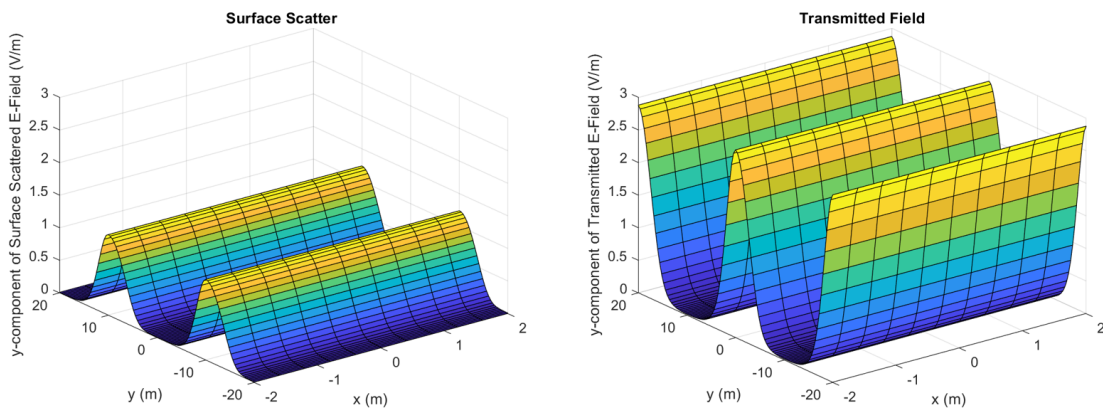


Figure 3.11: Surface scattered field (left) and field transmitted through the surface (right)

3.7 Scatter from Stratified Media

Walsh has developed equations for the total field above the layers when stratified media are present [83], [84]. The solution for the spatial fields for the two layer case was presented in Chapter 1, but it is instructive to examine the Fourier transformed fields. For convenience, the y - and z - components of the expression are reproduced here from [84] as

$$\begin{aligned} \underline{E}_y^{z^+} = & \underline{E}_{sy}^{z^+} + e^{-z^+u_0} \left[\frac{u_0 - U_{1h}}{u_0 + U_{1h}} E_{0sy} \right. \\ & \left. - jk_y \frac{2u_0 \frac{1}{n_1^2} \nu_1 + N_{10}}{(u_0 + U_{1h})(u_0 + \frac{1}{n_1^2} U_{1z})} E_{0sz} \right] \end{aligned} \quad (3.12)$$

and

$$\underline{E}_z^{z^+} = \underline{E}_{sz}^{z^+} + e^{-z^+u_0} \frac{u_0 - \frac{1}{n_1^2} U_{1z}}{u_0 + \frac{1}{n_1^2} U_{1z}}, \quad (3.13)$$

where N_{10} is a function of the permittivity of layers 1 and 0, U_{1h} and U_{1z} are each a function of the electrical characteristics of the layers and are calculated recursively as

$$U_{mh} = \frac{u_m \tanh((a_m - a_{m-1})u_m) + U_{(m+1)h}}{1 + \tanh((a_m - a_{m-1})u_m) \frac{U_{(m+1)h}}{u_m}}$$

and

$$U_{mz} = \frac{u_m \tanh((a_m - a_{m-1})u_m) + \frac{n_m^2}{n_{m+1}^2} U_{(m+1)z}}{1 + \tanh((a_m - a_{m-1})u_m) \frac{n_m^2}{n_{m+1}^2} \frac{U_{(m+1)z}}{u_m}},$$

where for the lowest layer $U_{Mh} = U_{Mz} = u_M$ and ν_1 is calculated recursively as

$$\nu_m = \frac{(1 - \tanh^2((a_m - a_{m-1})u_m)) \left(\frac{n_m^2}{n_{m+1}^2} \nu_{m+1} + N_{(m+1)m} \right)}{\left(1 + \tanh((a_m - a_{m-1})u_m) \frac{U_{(m+1)h}}{u_m} \right) \left(1 + \tanh((a_m - a_{m-1})u_m) \frac{n_m^2}{n_{m+1}^2} \frac{U_{(m+1)z}}{u_m} \right)}$$

and $\nu_M = 0$, where $N_{(m+1)m}$ is a function of the permittivity of layers $m + 1$ and m . It may be seen that the total field above the layers consists of a source, or zero order scatter component, and a term for scattering from the layers. Simulations using a dipole source have shown that the third term in (3.12) is two orders of magnitude smaller than the second term. Further discussion on this point is given in Appendix B. The third term in (3.13) will be ignored for all future analysis. The second term in the expressions has the form of a scaled image of the source since the exponent of e is $(-z^+)$. The scale factor for the horizontal (i.e., y) component is $(u_0 - U_{1h})/(u_0 + U_{1h})$, which has the same structure as the reflection coefficient for horizontally-polarized fields [82]

$$r_H = \frac{u_0 - kn_1}{u_0 + kn_1}. \quad (3.14)$$

Similarly, the scale factor for the vertical (i.e. z) component is $(u_0 - 1/n_1^2 U_{1z})/(u_0 + 1/n_1^2 U_{1z})$, which has the same structure as the reflection coefficient for vertically polarized fields [82]

$$r_V = \frac{u_0 - k \frac{\sqrt{n_1^2 - 1}}{n_1^2}}{u_0 + k \frac{\sqrt{n_1^2 - 1}}{n_1^2}}. \quad (3.15)$$

Thus, it is possible to express the scattered field portion of (3.12) and (3.13) in terms of a simple scattering coefficient. Above the surface, the field scattered from stratified media may be expressed in terms of the source field as

$$\begin{aligned}\underline{E}_y^s &\approx \underline{\Gamma}_{Ly} \underline{E}_{0sy} e^{-z^+ u_0} \\ \underline{E}_z^s &= \underline{\Gamma}_{Lz} \underline{E}_{0sz} e^{-z^+ u_0}\end{aligned}\quad (3.16)$$

where E_y^s and E_z^s are the y - and z - components, respectively, of the scattered field and Γ_{Ly} and Γ_{Lz} are the y - and z - components of the scattering coefficient. In this context the source terms, E_{0sy} and E_{0sz} , are the y - and z - components, respectively, of the field transmitted through the surface and incident on the layers. In this way it is possible to express the field scattered from the layers in terms of reflection coefficients. As described in Chapter 1, the rough surface plane wave scattering equations limit the spatial wavenumbers such that $k_x = -k_x^\circ$ and $k_y = -(k_y^\circ - qk_0)$. Using the Fourier transform pair of equations,

$$\begin{aligned}\underline{f}(k_x, k_y) &= \int_x \int_y f(x, y) e^{-jk_x x - jk_y y} dx dy, \\ f(x, y) &= \frac{1}{4\pi^2} \int_{k_x} \int_{k_y} \underline{f}(k_x, k_y) e^{jk_x x + jk_y y} dx dy,\end{aligned}\quad (3.17)$$

it is possible to directly write the spatial domain equations as

$$\begin{aligned}E_y^s &\approx \frac{1}{4\pi^2} \frac{u_0^\circ - U_{1h}^\circ}{u_0^\circ + U_{1h}^\circ} e^{-z^+ u_0} E_{0sy} \\ E_z^s &= \frac{1}{4\pi^2} \frac{u_0^\circ - \frac{1}{n_1^2} U_{1z}^\circ}{u_0^\circ + \frac{1}{n_1^2} U_{1z}^\circ} e^{-z^+ u_0} E_{0sz}.\end{aligned}\quad (3.18)$$

The inverse transform which makes it possible to readily obtain (3.18), also means that the subsurface scatter is also a function of the modal expansion used for the

rough surface equations. These expressions are for calculating the total scatter from the layers, including the surface layer. Since scatter from the surface has already been accounted for, the expression must be modified as

$$\begin{aligned} E_y^s &\approx \frac{1}{4\pi^2} \frac{u_1^\circ - U_{2h}^\circ}{u_1^\circ + U_{2h}^\circ} e^{-z+u_0} E_{0sy} \\ E_z^s &= \frac{1}{4\pi^2} \frac{u_1^\circ - \frac{1}{n_2^2} U_{2z}^\circ}{u_1^\circ + \frac{1}{n_2^2} U_{2z}^\circ} e^{-z+u_0} E_{0sz}, \end{aligned} \quad (3.19)$$

where $u_1^\circ = \sqrt{(k_x^\circ)^2 + (k_x^\circ)^2 - n_1^2 k^2}$, n_2 is the refractive index of the second layer of ice and U_{2h}° and U_{2z}° are calculated by considering the second layer as the top layer where the superscript $^\circ$ dictates the valid wavenumbers as per (1.39) and (1.40). The expression now considers scatter from the layers looking down from the first layer. The two-way signal attenuation through the top layer may be taken into account using an empirically-derived method as discussed in [9], [4] and will be discussed in Chapter 4.

3.8 Scatter from the Underside of the Rough Surface

The rough surface scattering equations presented in (2.13) and (2.14) are specific to the surface specified in (1.25). To determine the scattering from the underside of the rough surface it is important to recognize:

1. The underside of the rough surface is different from the topside and the scattering equations must be rederived.
2. The impedance contrast is reversed, since the wave is traveling from the top

layer of ice to air.

The remainder of this section provides details on how these aspects of the analysis may be accomplished.

When observing the interface from below the rough surface, the equation describing the rough surface profile is the opposite of (1.25) with peaks and troughs directly interchanged and may be expressed as

$$f^u(x, y) = b - a \cos(k_0 y), \quad (3.20)$$

where $b - a \geq 0$ for $a, b > 0$ as required for Walsh's formulation [82]. Fortunately the scattering equations from the surface, f^u , do not need to be completely rederived and similarities with the derivations of (2.13) and (2.14) may be exploited in the solution. Rather than giving all the details, a brief introduction to the equations is provided. Walsh [82] expresses the transform of the scattered field, \underline{E}_y^s , as

$$\underline{E}_y^s = \frac{e^{-z^- u_0^u}}{2u_0^u} \left[\int_{x'} \int_{y'} [|\vec{n}^u|^2 E_y^+(x', y') u_0^u + R_y^+] e^{f^u(x', y') u_0^u} e^{-jk_x x' - jk_y y'} dy' dx' \right], \quad (3.21)$$

where \vec{n}^u is the normal to the surface pointing downwards and the primed coordinates arise from a convolution operation earlier in the equation derivation. The superscript u again refers to the upward traveling wave when the EM wave travels from the ice to free space such that $u_0^u = \sqrt{k_x^2 + k_y^2 - n_{ice}^2 k^2}$ and n_{ice} is the refractive index of the top layer of the ice. A similar expression may be written for the y - and z - components of the scattered field. The expression for R_y^+ , acknowledging that the surface only varies with respect to y , is

$$\begin{aligned}
R^+ = & - (1 - n_{ice}^2) \left[-f_{yy}^u E_y^+ - f_y^u \frac{\partial E_y^+}{\partial y} + \frac{\partial E_z^+}{\partial y} \right] \\
& - u_1^u \left[\left(1 + \frac{(f_y^u)^2}{n_1^2}\right) E_y^+ + f_y^u (1 - n_{ice}^2) E_z^+ \right], \tag{3.22}
\end{aligned}$$

where $f_y^u = \partial f^u / \partial y$, $f_{yy}^u = \partial^2 f^u / \partial y^2$ and $u_1^u = \sqrt{k_x^2 + k_y^2 - k^2}$. Since the surface normal is defined as

$$\vec{n}^u = -f_x^u \hat{x} - f_y^u \hat{y} + \hat{z}. \tag{3.23}$$

It is possible to expand (3.21) to yield

$$\begin{aligned}
\underline{E}_y^s = & e^{-z^- u_0} [u_0 - u_1] \int_{x'} \int_{y'} E_y^+ K^+ dy' dx' + (u_0 - u_1) \int_{x'} \int_{y'} (f_{y'}^u)^2 E_y^+ K^+ dy' dx' \\
& + (1 - n_{ice}^2) \int_{x'} \int_{y'} f_{y'y'}^u E_y^+ K^+ dy' dx' + (1 - n_{ice}^2) \int_{x'} \int_{y'} f_{y'}^u \frac{\partial E_y^+}{\partial y'} K^+ dy' dx' \\
& - u_1 (1 - n_{ice}^2) \int_{x'} \int_{y'} f_{y'}^u E_z^+ K_L dy' dx' \\
& - (1 - n_{ice}^2) \int_{x'} \int_{y'} \frac{\partial E_z^+}{\partial y'} K^+ dy' dx', \tag{3.24}
\end{aligned}$$

where $K^+ = e^{f(x',y')u_0} e^{-jk_x x' - jk_y y'}$ has been used to shorten the expression. The bandlimited field above the surface may be expressed as the inverse Fourier transform of an unknown function \vec{G}_1 as

$$E_y^+(x', y') = \frac{1}{4\pi^2} \int_{k_{x'}} \int_{k_{y'}} G_{1y}(k'_x, k'_y) e^{f^u(x',y')u'_0} e^{jk_x x' + jk_y y'} dk'_x dk'_y \tag{3.25}$$

and

$$E_z^+(x', y') = \frac{1}{4\pi^2} \int_{k_x'} \int_{k_y'} G_{1z}(k_x', k_y') e_L^{f^u(x', y')u_0'} e^{jk_x x' + jk_y y'} dk_x' dk_y' \quad (3.26)$$

where k_x', k_y', e_L and u' indicate that the spatial frequency is bandlimited to $k_x'^2 + k_y'^2 \leq k^2$ and $u_0' = \sqrt{k_x'^2 + k_y'^2 - n_{ice}^2 k^2}$. The variables k_x' and k_y' are the spatial transform variables for G_1 . Using (3.25) and (3.26), and rearranging the order of the integrals, it is possible to express the individual integrals of (3.24) as

$$\begin{aligned} \int_{x'} \int_{y'} E_y^+ K^+ dy' dx' &= \frac{1}{4\pi^2} \int_{k_x'} \int_{k_y'} G_{1y}(k_x', k_y') \\ &\int_{x'} \int_{y'} e_L^{f^u(x', y')(u_0' + u_0)} e^{-j(k_x - k_x')x' - j(k_y - k_y')y'} dy' dx' dk_y' dk_x', \end{aligned} \quad (3.27)$$

$$\begin{aligned} \int_{x'} \int_{y'} (f_{y'}^u)^2 E_y^+ K^+ dy' dx' &= \frac{1}{4\pi^2} \int_{k_x'} \int_{k_y'} G_{1y}(k_x', k_y') \\ &\int_{x'} \int_{y'} (f_{y'}^u)^2 e_L^{f(x', y')(u_0' + u_0)} e^{-j(k_x - k_x')x' - j(k_y - k_y')y'} dy' dx' dk_y' dk_x', \end{aligned} \quad (3.28)$$

$$\begin{aligned} \int_{x'} \int_{y'} f_{y'} e_L^{f(x', y')(u_0' + u_0)} E_y^+ K^+ dy' dx' &= \frac{1}{4\pi^2} \int_{k_x'} \int_{k_y'} G_{1y}(k_x', k_y') \\ &\int_{x'} \int_{y'} f_{y'} e_L^{f(x', y')(u_0' + u_0)} e^{-j(k_x - k_x')x' - j(k_y - k_y')y'} dy' dx' dk_y' dk_x', \end{aligned} \quad (3.29)$$

$$\begin{aligned}
\int_{x'} \int_{y'} f_{y'}^u \frac{\partial E_y^+}{\partial y'} E_y^+ K^+ dy' dx' &= \frac{1}{4\pi^2} \int_{k'_x} \int_{k'_y} u'_0 G_{1y}(k'_x, k'_y) \cdot \\
&\int_{x'} \int_{y'} (f_{y'}^u)^2 e^{f^u(x',y')(u'_0+u_0)} e^{j(k_x-k'_x)x'+j(k_y-k'_y)y'} dk'_x dk'_y \\
&+ \frac{1}{4\pi^2} \int_{k'_x} \int_{k'_y} j k_{y'} G_{1y}(k'_x, k'_y) \cdot \\
&\int_{x'} \int_{y'} f_{y'}^u e_L^{f^u(x',y')(u'_0+u_0)} e^{-j(k_x-k'_x)x'-j(k_y-k'_y)y'} dy' dx' dk'_y dk'_x, \tag{3.30}
\end{aligned}$$

$$\begin{aligned}
\int_{x'} \int_{y'} f_{y'}^u E_z^+ K^+ dy' dx' &= \frac{1}{4\pi^2} \int_{k'_x} \int_{k'_y} G_{1z}(k'_x, k'_y) \cdot \\
&\int_{x'} \int_{y'} f_{y'}^u e_L^{f^u(x',y')(u'_0+u_0)} e^{-j(k_x-k'_x)x'-j(k_y-k'_y)y'} dy' dx' dk'_y dk'_x, \tag{3.31}
\end{aligned}$$

and

$$\begin{aligned}
\int_{x'} \int_{y'} \frac{\partial E_z^+}{\partial y'} E_y^+ K^+ dy' dx' &= \frac{1}{4\pi^2} \int_{k'_x} \int_{k'_y} u'_0 G_{1z}(k'_x, k'_y) \cdot \\
&\int_{x'} \int_{y'} (f_{y'}^u)^2 e^{f^u(x',y')(u'_0+u_0)} e^{j(k_x-k'_x)x'+j(k_y-k'_y)y'} dk'_x dk'_y \\
&+ \frac{1}{4\pi^2} \int_{k'_x} \int_{k'_y} j k_{y'} G_{1z}(k'_x, k'_y) \\
&\int_{x'} \int_{y'} e_L^{f^u(x',y')(u'_0+u_0)} e^{-j(k_x-k'_x)x'-j(k_y-k'_y)y'} dy' dx' dk'_y dk'_x. \tag{3.32}
\end{aligned}$$

To solve the integrals in (3.27)-(3.32), $e^{f^u(x',y')(u'_0+u_0)}$ is expanded as a Fourier series and the partial derivatives of the surface profile are needed. To calculate (2.13) and (2.14) the partial derivatives of the rough surface as viewed from above the surface are found to be

$$\begin{aligned}
f &= b + a \cos(k_0 y') \\
f_{y'} &= -ak_0 \sin(k_0 y') \\
f_{y'}^2 &= (ak_0)^2 \sin^2(k_0 y') \\
f_{y'y'} &= -ak_0^2 \cos(k_0 y').
\end{aligned} \tag{3.33}$$

Scatter from the layers must pass through the underside of the rough surface and the derivatives of the underside of the surface are

$$\begin{aligned}
f^u &= b - a \cos(k_0 y') \\
f_{y'}^u &= ak_0 \sin(k_0 y') \\
(f_{y'}^u)^2 &= (ak_0)^2 \sin^2 k_0 y' \\
f_{y'y'}^u &= ak_0^2 \cos(k_0 y').
\end{aligned} \tag{3.34}$$

It is apparent there are similarities between (3.33) and (3.34). It may be observed that $\text{sgn}(f_{y'}^2) = \text{sgn}((f_{y'}^u)^2)$, but $\text{sgn}(f_{y'}) = -\text{sgn}(f_{y'}^u)$ and $\text{sgn}(f_{y'y'}) = -\text{sgn}(f_{y'y'}^u)$, which makes it possible to simplify the expressions in (3.27) to (3.32) using the calculations for scattering from above the rough surface as given in [82] and Chapter 2.

3.9 Transmission Upward Through Underside of Rough Surface

There are two challenges that must be addressed to determine the field transmitted through the air-ice interface. First, the modes of the field transmitted through the air-ice interface must properly correspond with the modes of the field transmitted back to the air from the ice. Second, the field transmitted through the surface will have co- and cross-polarized components that must be combined properly.

3.9.1 Combining Modes of Electric Field

In this research the scattered field is determined by tracing the path followed by the energy as illustrated in Figure 3.5. Using this approach the source for the field transmitted through the surface is the incident plane wave and the source for the field transmitted upward through the ice-air interface is the field scattered from the ice layers. The scattered field is a function of both the source and the surface. Even though the frequency of the surface variation is the same whether approaching from above or below and the number of modes for the surface expansion will be the same for the downward and upward going waves, there will not be a direct correspondence between modes of the same index. That is, each mode of the overall scattered field, $(E^s)^q$, is not proportional to the direct product of the transmission coefficients for the downward and upward going waves. This is because the modes are created using a series expansion and the transmission coefficients for the upward going wave must be calculated by expanding the transmission coefficients for the downward going wave.

A comparison of the expression for the incident plane wave source in (3.3) with the scattering equations of (2.13), (2.14) shows that the total scattered wave is the sum of plane waves that are scaled by the scattering coefficients. This means that

each mode of the wave transmitted into the ice may be treated as an incident plane wave and further expanded. The approach of considering a wave as a sum of plane waves has been discussed by Wait [75] and has not been explicitly applied to Walsh's method prior to this work.

Fortunately, the analysis yields an intuitive result: when the surface is inverted, the shape of the scattered field is reversed as well. This is illustrated for the magnitude of the co-polarized scattered wave in Figure 3.12 using the same parameters as were used for Figure 3.11. It is important to note that the two plots are not direct inverses as they both exhibit sharp peaks and shallower troughs, but the peaks of one plot are aligned with the troughs of the other. The scatter from the underside of the surface has a very similar appearance to the transmitted field, but for different reasons. Recall that the difference in scattered and transmitted fields is because lower scattering corresponds to higher transmission and vice versa. Here, an inverted surface leads to a reversal between the peaks and troughs. The scatter from the top and bottom of the surface is different because the contrast between the refractive index is reversed for the downward and upward going waves. The transition from air to ice for the downward going wave is different for the transition from ice to air for the upward going wave.

3.9.2 Total Polarized Field

It is well understood that when EM fields interact with objects it is possible for the polarization state to change, especially when there are multiple reflections. It is apparent from (2.13) and (2.14) that depolarization occurs from rough surface scatter, but it is implicitly assumed from the simplification resulting in (3.16) that depolarization is negligible for scattering from stratified media for the geometry being considered. Thus, referring again to Figure 3.5, it may be seen that a portion of the

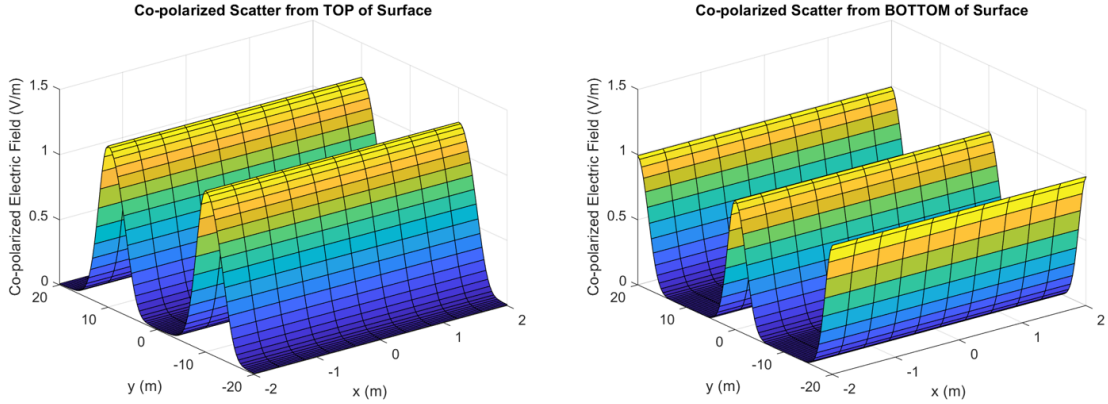


Figure 3.12: Co-polarized scattering from the top and bottom of a rough surface

radar wave becomes depolarized from the scattering and transmission through the rough surface. There is no change in the polarization for scatter from the subsequent layers but again depolarization occurs for transmission upward through the ice-air rough interface. When observing any single component of the wave, in this case the y - or z -component, both co- and cross-polarized contributions must be considered. The scattering directly from the rough surface is defined as per (2.13), (2.14) and the scattering terms from the layers are illustrated in Figure 3.13. Recall that for the reflection and transmission coefficients, the first letter in the subscript indicates the output polarization and second letter is the input polarization. The number in the subscript refers to the scattering event where ‘1’ refers to the downward traveling wave from the source incident on the rough surface from above and ‘2’ denotes the upward traveling wave scattered from the layers and incident on the rough surface from below. The bottom row of the figure shows that the y -component of the scattered wave has two subcomponents: \mathcal{T}_{yy2} and \mathcal{T}_{yz2} . The \mathcal{T}_{yy2} term results when the y -polarized source transmits through the surface and back up without undergoing any depolarization through the pathway $E_y \rightarrow \mathcal{T}_{yy1} \rightarrow \Gamma_{Ly} \rightarrow \mathcal{T}_{yy2}$ and the \mathcal{T}_{yz2} term undergoes two depolarizations through the pathway $E_y \rightarrow \mathcal{T}_{zy1} \rightarrow \Gamma_{Lz} \rightarrow \mathcal{T}_{yz2}$. A similar process

occurs for the z -component of the wave, except both \mathcal{T}_{zz2} and \mathcal{T}_{zy2} undergo a single depolarization. An example of the overall scatter is illustrated in Figure 3.14. For this example the simulation is based on properties of a MY ridge. Further details on ridge properties are discussed in Chapter 4 and simulations will be described in detail in Chapter 5. The lower surface of the ice is assumed to be flat and the bottom layer is sea water. In this case the larger, off center peaks are due to surface scatter and the smaller central and edge peaks are caused by the subsurface scatter. It is possible to distinguish between the surface and subsurface scatter in this example since the length scale of the surface roughness is known and has been chosen to be much larger than the radar wavelength to illustrate the individual contributions to the overall scatter. For general roughness it will not be possible to separate the contributions to the overall scatter. For the parameters considered in this study, the magnitude of scatter from the subsurface is generally smaller than the direct rough surface scatter for both the co-polarized and cross-polarized cases, but this will depend on surface roughness and effective permittivity of the layers. Chapter 5 focuses on quantifying the impact that ice properties, ice types and surface properties have on the magnitude of the co- and cross-polarized scatter.

3.10 Possible Extensions

There are numerous directions that this work can follow to better simulate real world conditions. Normal incidence with a plane wave source has been assumed here and preliminary work has been completed using a dipole source. The current research has also been restricted to a simple rough surface over smooth, isotropic, homogeneous layers, which are restrictions not imposed in other research (e.g., [79], [80], [81]). The focus of this research has been on the forward problem, i.e., to determine the

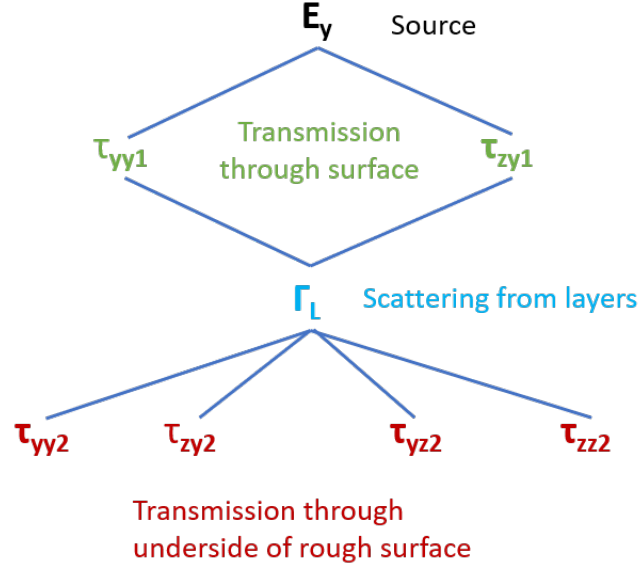


Figure 3.13: Scattering components from the layers

scattered fields for a given source irradiating certain media. During field studies the inverse problem is more relevant. Both the source and scattered fields will be known and may be used to estimate the characteristics of the surface and internal structure and composition.

It is possible to extend the current method to one of rough layers using the transmission line technique. Daniels [110] considers the case of ground penetrating radar through smooth homogeneous layers and uses reflection and transmission coefficients. Figure 3.15 illustrates the geometry of the layers. Rather than considering the layers collectively, each layer is considered consecutively. Assuming smooth interfaces, the reflection from interface 2 is, for example $\Gamma_{23} = \frac{n_2 - n_3}{n_2 + n_3}$ and the field scattered from interface 2, E_2^s is

$$E_2^s = E_0 \mathcal{T}_{01} \mathcal{T}_{12} \Gamma_{23} \mathcal{T}_{21} \mathcal{T}_{10}, \quad (3.35)$$

where E_0 is the electric field incident to the layers and the transmission coefficients are

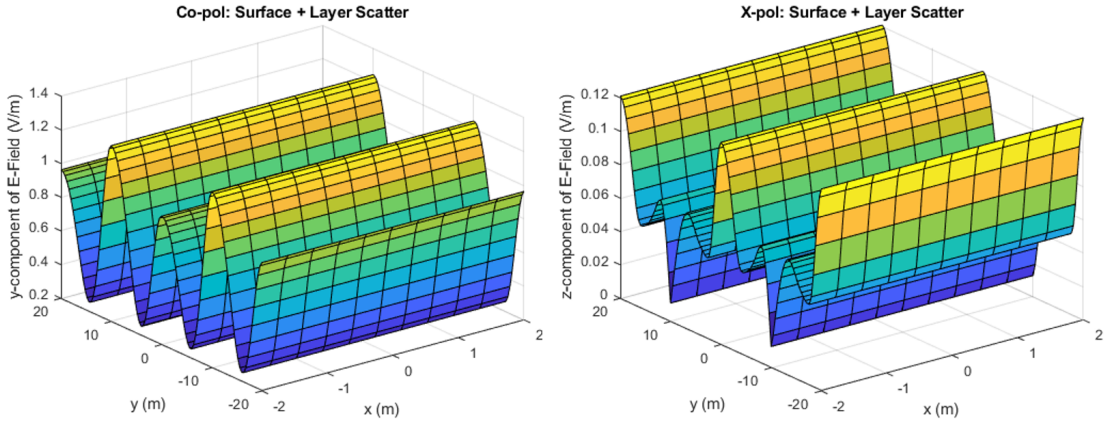


Figure 3.14: Co-polarized and cross-polarized scatter from surface and layers

calculated as per (3.7), but with the propagation losses for each layer accounted for as well. For rough interfaces, the procedure outlined in Section 3.5 and Section 3.6 may be used to determine the reflection and transmission coefficients. The total scattered field can be found by combining the contributions from each layer. This simple model does not consider collectively how the layers above and below each interface have an impact on the reflection and scattering. Instead, the scattering and transmission from each layer are considered individually.

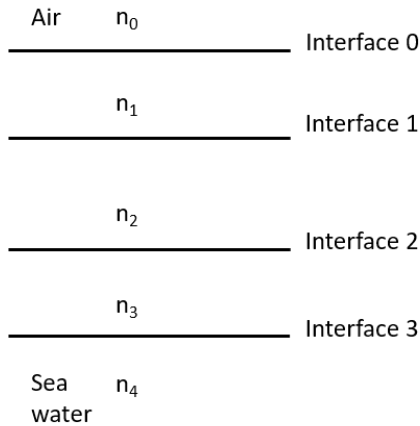


Figure 3.15: Transmission line model for determining reflection and transmission coefficients

This model is easily extended to rough interfaces where the modal reflection coefficients are calculated from (2.13) and (2.14). The scattering from the layers does not need to be computed and instead the contributions from each layer must be summed. Although this approach grows rapidly in complexity as the number of layers increases, it is able to handle any number of rough interfaces and multiple scattering between the layers.

3.11 Summary

This chapter begins with a brief justification of sea ice ridges as layered media with a rough surface. Under this premise, a new approach has been developed applying Walsh's method to model scatter from a rough surface that overlies stratified media. The total scattered field is the sum of the scatter from the surface and from the layers. The scatter from the surface was discussed in Chapter 2 by extending Walsh's method to non-conducting surfaces [91] and general surface slopes. Calculating the field transmitted through the air-ice interface is possible by considering an alternate form of the relationship between the transmission and reflection coefficients and recognizing that the field in the layers is a sum of plane waves weighted by the original transmission coefficients. The scatter from stratified media using Walsh's analysis [83] involves co-polarized and cross-polarized components, but the cross-polarized component for scatter at normal incidence is negligible and the scattered field may be determined as a scattering or reflection coefficient. Scattering from the underside of the rough surface requires that the scattering equations be revised, but there are many similarities with the original equations, which simplifies the task. By combining the surface and subsurface scatter terms it is possible to find the total scattered field. This work is the first time Walsh's method has been used to model scatter from rough surfaces

above stratified media for the application of penetrating through a surface, rather than propagation across the surface.

The beginning of this chapter provided a basic description of sea ice ridges as rough surfaces over stratified media. Chapter 4 presents more details of the structure and properties of sea ice ridges relevant to scattering at VHF.

Chapter 4

Modeling Sea Ice Ridges for Scattering at VHF

4.1 Introduction

Sea ice has been described as a thin solid layer that forms near the poles and separates two much larger fluid regions, the ocean and the atmosphere [111], and serves as an insulator between those two layers [112]. Sea ice was originally considered only as an obstacle to navigation [113], but has since inspired significant study that consumes vast data and human resources. Since World War II sea ice research has exploded due to factors such as the Cold War, Arctic offshore oil and gas exploration and development, climate change and advances in satellite radar.

Detailed descriptions of the growth and structure of sea ice are available (e.g., [62], [63], [111], [114]) and sea ice ridges have been studied extensively as well. Studies have also been carried out to understand the morphology (e.g., [2], [105], [115]), internal structure (e.g., [7], [8], [107]) and internal properties (e.g., [4], [116], [117]) of sea ice ridges. The mechanics of sea ice ridge formation has been modeled for individual

ridges (e.g., [102]) and for distributions of ridges (e.g., [106]). Ice redistribution, or deformation, is also considered in global sea ice/ocean models (e.g., [118]). The mechanics of ice ridge interaction with structures has been studied (e.g., [20], [119], [120]). The total force per unit width that may be exerted by a ridge or rubble field on a structure has been simply represented as the sum of the unit failure forces that may be exerted by the sail, consolidated layer and unconsolidated keel [20]. Due to the low volume of the sail, the loading contribution from the sail may be ignored [121].

EM-based remote sensing methods for assessing ice thickness, structure and strength rely on surface characteristics. For example, passive microwave may be used to retrieve ice thickness since sea ice surface dielectric properties change as the ice thickens. Similarly, satellite synthetic aperture radar (3-10 GHz) assessments of ice thickness are based on surface roughness and dielectric properties [52]. Some research has been done to model scattering from sea ice ridges using penetrating radar, but the main emphasis was on measuring ice thickness [58].

The goal of this chapter is to develop models of FY and MY sea ice ridges that are relevant for VHF scattering. Section 4.2 discusses how the main characteristics of FY and MY sea ice differ. Due to limited field data of sea ice ridges, trends in level sea ice properties will be used to provide insight on ridge properties at different times of the year. Next, Section 4.3 describes the characteristics of the main physical components of sea ice ridges. This information is provided since there is a link between the physical and electrical characteristics of sea ice ridges and it is important to understand the structure and composition of sea ice ridges. Section 4.4 lists some studies of sea ice ridges and measured data on ridge properties. Section 4.5 outlines the equations needed to calculate the complex permittivity of sea ice ridges based on their physical characteristics. Finally, Section 4.6 presents the structure and physical characteristics of sea ice ridge models to be used in the scattering simulations of Chapter 5.

Sea ice ridges were first discussed as having a rough surface over layers in Chapter 2, but this modeling approach along with the simplifications to the model will be more fully justified. Sea ice ridges will change during the season and model parameters will be provided for fall, mid-winter and early spring. Sea ice ridge properties for the melt season are not provided since ice characteristics are more variable, limited penetration of the EM wave is expected due to surface and subsurface water and alternate approaches are required for modeling the permittivity.

4.2 Overview of Sea Ice Properties

FY and MY ice differ in form and composition. This section considers composition differences through the parameters of salinity, density and micro-porosity. Temperature is also included since ice properties vary with temperature. These properties are directly used to calculate the relative permittivity of sea ice using the equations presented in Section 4.5.

4.2.1 Salinity

Salinity (S) is a dimensionless measure of the mass fraction of dissolved salts in water and is measured in parts per thousand (ppt or ‰, e.g., [114]) or in terms of practical salinity units (psu). Although the salinity of sea water varies geographically, its composition is generally consistent and there is a relationship between electrical conductivity and mass fraction, which is the basis for psu measurements [122]. The psu scale was intended to be used for salinities and temperatures naturally present in the oceans and salinity reported as psu and ppt are found to be within 0.01‰ over typical sea water salinities [123]. Since sea ice brine may be much colder and saline than typical sea water and to maintain consistency with historical studies, salinity

will be reported in parts per thousand in this study.

As sea water freezes, salt does not get incorporated in the ice crystals, but rather remains as concentrated brine between the pure ice crystals. In addition, the salinity of sea ice is much less than that of the water from which it formed. The salinity of sea ice is greatest when it is first forming and depends on the water salinity and the rate of freezing with faster freezing rates leading to more saline sea ice.

Malmgren [5] studied the salinity of FY sea ice as a function of depth and time of year. He noted that the salinity profile from October to June had a characteristic ‘C’ shape with higher salinities at the top and bottom of the sea ice and lower salinity in the middle. A plot of his results is shown in Figure 4.1. The average salinity of growing FY ice is in the range 4-6 ppt. Since the prime mechanism for brine drainage is gravity, the top of the ice has the greatest salinity as it cannot drain as readily. A secondary contribution to brine loss is brine expulsion, during which brine moves up through the ice. During ice growth, the bottom of the sea ice also has high salinity since the sea ice is in contact with the high salinity sea water. The bottom 1-3 cm of the ice is called the skeleton layer with a dendritic structure. The skeletal layer is structurally weak and undergoes advective exchange with the sea water and has very high salinity [63]. The skeletal layer will have an impact on EM scatter when the EM wavelength has a similar length scale to the thickness of the skeleton layer and is not expected to have an impact at VHF [58].

The salt in sea ice is in the form of concentrated brine that is at phase equilibrium, which means the brine is always at its freezing point and brine salinity is dependent on temperature. As the temperature rises the brine pockets grow larger as ice is melted. The brine salinity reduces and the brine volume rises. The opposite process occurs as the temperature drops [62]. At sufficiently low temperatures, specific salts will precipitate. For example, at -8.2°C mirabilite ($\text{Na}_2\text{SO}_4 \cdot 10\text{H}_2\text{O}$) starts to precipitate

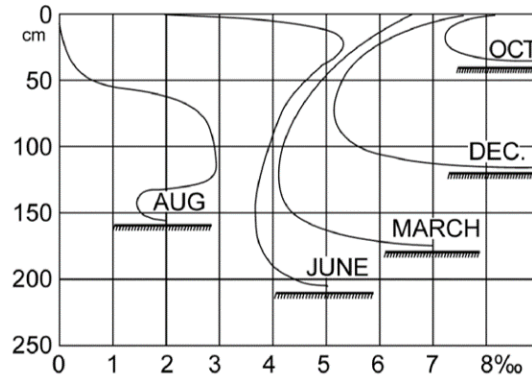


Figure 4.1: FY sea ice salinity vs depth, from [5]

and at -22.9°C hydrohalite ($\text{NaCl} \cdot 2\text{H}_2\text{O}$) begins to precipitate. Solid salts do not have a noticeable effect on EM scatter, but at the onset of precipitation of a salt there is a step change in the brine salinity, and hence the dielectric permittivity [86].

The brine is located in needle shaped inclusions at ice crystal boundaries [86], [114]. Most of the salt is rejected as ice forms and brine continues to leave the ice through brine channels. As temperatures warm in the spring, brine channels grow and surface meltwater percolates through the porous ice and flushes most of the remaining brine from the ice, especially the upper layers. Late summer ice will have low salinity as will old ice. In this way the salinity of FY ice varies with temperature and time of year. Salinity continues to decline over repeated melt seasons until MY ice reaches a stable year round average value of between 1-2‰ [124], [125]. The salinity profile of MY ice is not homogeneous as the top of the sail may have virtually no salt content and salinity increases with depth [63], [126].

4.2.2 Density

At a given temperature and salinity, sea ice density is a function of the proportions of pure ice, brine and entrapped gas. Although the concept of density is straight forward, it is challenging to measure in the field since it is difficult to cut an ice specimen with

exact dimensions, brine may quickly drain from the ice, especially at temperatures above -15°C , entrapped gas may escape if the density is determined after melting and the ice may become saturated if the volume is determined by the amount of fluid it displaces upon submersion [6]. Nonetheless, accurate measures of density are important as a 5% error in density leads to a 60% error in gas volume [124].

At a set salinity and temperature there is a linear relationship between density and air volume or brine salinity, as illustrated in Figure 4.2. For a given salinity, over the temperature range from -22.9°C to -5°C there is a linear relationship between density and temperature (4.3). Above -5°C density rises more rapidly and below -22.9°C there is a change in the relationship as hydrohalite begins to precipitate; these changes are more pronounced at higher salinities. However, it may be observed from Figure 4.3 that there is very little change in density with temperature for temperatures below -5°C .

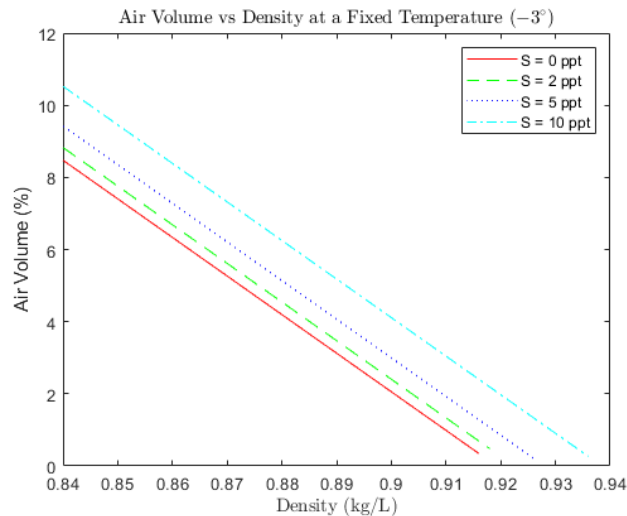


Figure 4.2: Air volume vs density at a fixed temperature, from [6]

There have been a number of studies of sea ice density that indicate density differences between FY and MY ice above the water line and differences between ice above and below the waterline. Combining the results from several studies, Timco and Fred-

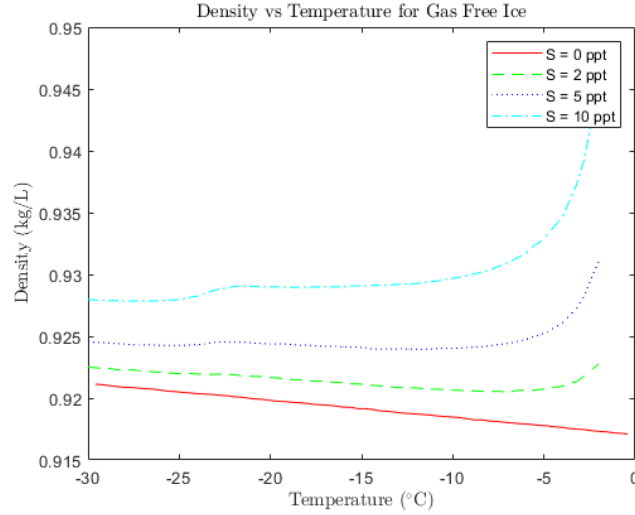


Figure 4.3: Density vs temperature for gas free ice, from [6]

erking (1996) report that the density of FY ice above the waterline varies between 0.84-0.91 kg/m³ and below waterline densities are in the range 0.90-0.94 kg/m³. The density of MY ice is in the range 0.72-0.94 kg/m³ and 0.89-94 kg/m³, for ice above and below the waterline, respectively [6]. Low sail density of MY ice is due to high porosity that occurs from brine drainage and refreeze cycles and is discussed in the following section. Ice below the waterline is typically denser since brine drainage is slower below the waterline and pores below the waterline are not likely to be filled with air. Thus, it is reasonable to expect that densities below the waterline are similar for FY and MY ice [114]. As brine drains from the ice, the density of FY ice and ridges composed of FY ice will decline. Since MY ridge salinity does not change substantially throughout the year its density will remain static [125], except for the top of the sail that undergoes melt and refreeze.

4.2.3 Micro-porosity

Total sea ice micro-porosity, ν_t is the sum of brine volume fraction, V_{br} , and air volume fraction, V_a . In the initial stages of sea ice growth, the porosity is dominated by the

brine volume and the air volume is less than 15‰. Porosity for FY ice may reach 200‰ at the bottom of the ice sheet, but values are typically between 20‰ and 60‰ [62]. As brine drains from the ice above the waterline it is replaced by air. Brine drainage below the waterline occurs less rapidly and it is less porous.

Due to the melt/refreeze cycle, MY ice undergoes more extensive brine drainage over the top 10-30 cm of the ice [127], but lower densities are found for the top 1 m of the ice. This high porosity region has numerous gas bubbles typically ranging in size from 1-3 mm, but bubbles have been observed as large as 6 mm [127] with interconnected air bubbles forming voids averaging 8 mm in size [128]. Macro-porosity is discussed in Section 4.3.1.

During the melt season the porosity of the ice increases. Brine channels expand and, in the Arctic, surface melt water flushes the ice of the brine. Brine volume increases while brine salinity decreases.

4.2.4 Temperature

Sea ice is present at a broad range of temperatures and temperature affects sea ice properties. In addition to previously discussed impacts on brine volume and density, temperature affects ice strength. Ice that is warmer and more porous is mechanically weaker, a fact that is of great engineering interest. Even old ice, which does not undergo the same brine rejection cycle as FY ice, is stronger at low winter temperatures and weaker at warmer summer temperatures [124].

For snow-free FY and MY ice the top of the ice can be as cold as the ambient air temperature and the bottom of the ice is at the freezing point of sea water ($\approx -1.8^\circ\text{C}$). During the winter months there is a linear temperature gradient for ice thinner than 80 cm (e.g., [63], [21]). Field studies confirm that cold ridges will also have a roughly linear temperature gradient (e.g., [117], [129]), making it easy to estimate the average

temperature of the ridge. During the melt season, the temperature profile follows a ‘C’ shape with higher temperatures near the top and bottom ice surfaces [114], [124]. This study will focus on the time period from fall through to early spring. The top of the ice may be taken to be close to the air temperature and the bottom of the ice will be close to the freezing point of sea water.

4.3 Sea Ice Ridge Structure

Sea ice ridges are typically formed from blocks of thinner (<50 cm) FY ice, but their characteristics are sufficiently different from level ice to warrant independent study. Sea ice ridges consist of a sail, consolidated layer and unconsolidated rubble [2], as illustrated in Figure 1.2. Pressure ridges are created by ice pressure events that break ice by bending or buckling. The colliding ice sheets are broken into blocks with aspect ratios (length to thickness) of 2-5 [21], [104]. The sails of pressure ridges have a blocky appearance and this research will focus on pressure ridges only. The remaining subsections provide details of each component of sea ice ridges. Each section provides a comparison of the characteristics of FY and MY ridges. MY ridges have survived at least two melt seasons, which is necessary to freeze all the voids between the ice blocks [64] but at times it is difficult to distinguish between FY and second-year features [130]. Although second year and MY ridges have different properties, for this research they will be considered together. The trends and values specified will be used to characterize sea ice ridges for the electromagnetic sea ice ridge model. The ridge structure includes the surface characteristics and internal composition and determines the nature of the surface and subsurface scatter. The impacts of ridge structure on the scattered field are discussed in Chapter 5.

4.3.1 Sail

Sea ice ridge sails appear striking as they can grow to several meters in height, a fact that is more formidable considering the buoyancy of ice which dictates that approximately 7/8 of the ridge mass is under water. FY ridges have a blocky appearance since the blocks of ice from which they are formed have not been weathered through a melt season and consolidated. The following sections provide details on sail morphology and composition. Ridge sail morphology may be characterized by three main features: sail height and keel to sail ratios, sail angle and block size. The composition of ridge sails, especially the salinity, micro-porosity and macro-porosity are distinct between FY and MY ridges.

Morphology

A comprehensive review of FY ridge morphology is provided in [2] using data from over 300 ridges collected over 40 years over Arctic and sub-Arctic areas. The average keel height to sail height ratio, $H_k/H_s = 5.17$, is consistent with earlier studies using smaller data sets, however this ratio will vary from region to region and throughout the ice season. Ridge sails have been found as high as 8 m, but most sails were under 3 m in height. Using high resolution stereo optical images captured from satellite, ridging has been found with maximum sail heights of 30 m, but no field observations were made to confirm the remote sensing results (C-CORE, unpublished). The tallest ridges were found in the Arctic as were the highest keel to sail ratios.

Using data collected from Operation IceBridge during 2009-2014, sea ice features were studied in the Beaufort/Chukchi Seas and Central Arctic. Using a scanning laser altimeter with a 200-300 m swath width allowed over 40000 surface features to be imaged. The summary of results presented in Table 4.1 reveals several interesting elements. MY ice features are slightly taller and more variable than FY features and

features in the Central Arctic are on average taller than those in the Beaufort/Chukchi region. However, across both regions and both ice ages, the typical feature height is 0.45 m. It is important to note that laser altimetry measurements include snow features and snow cover and do not measure ridge heights exclusively.

Table 4.1: Ice topography, summarized from [1]

Region	Mean (m)	Std. Dev. (m)	Mode (m)
Central Arctic FY Ice	1.03	0.59	0.45
Central Arctic MY Ice	1.36	0.82	0.45
Beaufort/Chukchi FY Ice	0.97	0.59	0.45
Beaufort/Chukchi MY Ice	1.10	0.67	0.45

A comprehensive review of first year sea ice morphology has been conducted from data collected around the Arctic and sub-Arctic [2]. The maximum ridge dimensions presented in Table 4.2 are the average values of the maximum ridge sails and keels over the data compiled for the study. The absolute maximum sail heights and keel depths are almost four times larger than the average values shown in the table.

Table 4.2: Morphology of first year ridges, taken from [2]

Region	Max. Sail Height (m)	Avg. Sail Height (m)	Max. Keel Depth (m)	Avg. Keel Depth (m)
Sub-arctic FY Ice	1.6	0.6	7.8	4.2
Arctic	2.1	0.8	8.2	4.8
All	2.0	0.7	8.0	4.5

There have been several smaller sea ice morphology studies. In one study, a data set of 112 FY ridges and 64 second year or MY ridges [105] found the keel to sail ratio to be 4.4 for FY ridges and 3.3 for second year or MY ridges.

In another study the morphology of FY and MY sea ice ridges were compared [131] as an extension of an analysis of ridge shapes [105]. A variety of data sources was compiled consisting of 85 second year or MY ridges from across the Barents and Norwegian Seas and the Beaufort Sea and Canadian/American Arctic. The study yielded similar

results to the altimeter-based results from [1] since mean ridge heights are similar for FY ridges and old ice ridges, but old ice ridges have greater maximum thickness. Given the variability of ridge geometry and the close similarity between mean FY and MY ridge sail heights, sail height is not a reliable parameter for separating ridge types.

Sail height of a FY ridge in the Baltic Sea was studied from formation to collapse. The sail height reduced slightly in the middle of the season, possibly due to settling or melting of the ridge blocks, and underwent further reduction during the early melt season [3]. No information was collected on block thickness or the overall blockiness of the ridge, but substantial weathering is not expected until the melt season is in progress. A summary of relevant results from [3] is given in Table 4.3. MY ridge sails will also decline during the melt season.

Table 4.3: Consolidation of FY ridge, from [3]. Standard deviations provided in parentheses where available

Parameter	Visit 1 13 days	Visit 2 48 days	Visit 87 days
Level ice thickness (m)	0.31	0.55	0.58
Sail thickness (m)	0.21 (0.17)	0.17 (0.16)	0.14 (0.07)
Max sail height (m)	1.08	1.00	0.60
Keel thickness (m)	3.13 (1.25)	2.89 (1.22)	2.19 (0.72)
Max keel depth (m)	5.28	4.45	3.12
Consolidated layer (m)	0.52 (0.19)	0.93 (0.25)	1.02 (0.31)
Porosity (macro)	0.281	0.203	0.175

The roughness of ridge sails may be described using sail angles and variations in sail height. Sail angles are dependent on ridge age and location. Although ridges have complex morphology, sails are often represented as symmetric triangles and the average sail angle for FY and MY ridges is 28° [2] and 19.5° [105], respectively. The correlation length for symmetrical triangles with reference to the peak may be expressed with respect to the sail height as $1.17H_s$ and $1.22H_s$ for FY and MY ridges,

respectively.

Surface height variations also occur within a ridge. Individual ice blocks are visible in first year ridges and ice block dimensions contribute to surface roughness. MY ridges are weathered and individual blocks are not visible. In the Beaufort Sea some ice blocks were 1.9 m thick and the Canadian Arctic had several ridges with blocks exceeding 1 m thickness. Due to these outliers, average block thickness in the Arctic was found to be approximately 0.7 m. In sub-arctic areas such as the East Coast of Canada and the Baltic Sea the average block thickness was around 0.25 m. While ice blocks contribute to surface roughness, their typical size is smaller than the EM wavelength so the arrangement of several blocks contributes to roughness at VHF.

Surface elevation profiles were taken of FY ridges and an example is provided in Figure 4.4. It may be seen that elevation changes are largely restricted to within 2.5 m and most features on the surface have a stable elevation over several metres.

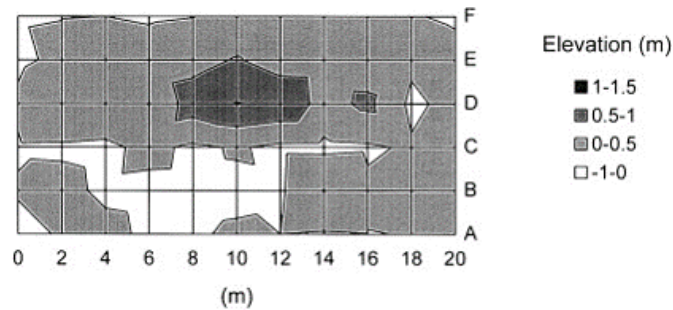


Figure 4.4: Elevation profile from a FY ridge, from [7]

Composition

Sail salinity and macro-porosity are relevant parameters to consider for modeling EM scatter at VHF. Section 4.2.1 states that level FY ice is more saline than MY ice and this is true for ridge sails as well. Salinities of MY sails are typically less than 1‰ (e.g., [4], [132]) and the salinity of FY sails can be as high as 7‰ [132], [7] although

average values through the sail will be lower.

Macro-porosity is defined as the ratio of non-ice volume (voids) to total ice volume [129]. Non-ice materials include water, slush and air. Voids containing these materials may be detected as a drop in drilling resistance and will also have an effect on the permittivity. In the sail, voids are filled with air or snow [62], [7] and are only present in FY ridges, since voids are filled with melt water and frozen through the melt and refreeze process for MY ridges. The macro-porosity of FY ridge sails may exceed 40%, but typical values are in the range 20-30% (e.g., [2], [8], [129]). Voids in the sail may be up to 2 m long and 0.05-0.15 m deep [7] and the sail cross section shown in Figure 4.5 illustrates how spaces between ice blocks may appear in FY sails. Voids in FY sails may be represented as additional layers of air in the model or as ice with higher porosity. It is reasonable to expect that void dimensions will be of the same order as block sizes, which is smaller than the EM wavelength. Thus, the EM field will interact with a mixture of ice and air when voids are present. It is possible that there are geographic variations in macro-porosity for FY ridges due to differences in the oceanographic forcing, but data are limited and it is not possible to draw conclusions [2]. Throughout the season, FY ridges continue to consolidate and there is a reduction in the macro-porosity, [3], but reduction of sail macro-porosity through consolidation will be limited since the voids are filled with air or snow. Changes in the macro-porosity for a single ridge are listed in Table 4.3, but these data may not represent changes in sail macro-porosity.

4.3.2 Consolidated Layer

The keel is the below water portion of a ridge, which may be further divided into the consolidated layer and the unconsolidated rubble. Although the consolidated layer may grow upwards into the sail if trapped water, slush or crushed ice are present at



Figure 4.5: Cross section of FY ridge illustrating high macro-porosity, from [8]

the bottom of the sail, for this discussion the consolidated layer is considered to exist below the water surface [2]. Just below the water surface upon ridge formation, small blocks of randomly oriented ice are present with voids filled with crushed ice, slush and water [20]. Since the voids are relatively small and are partially filled with icy constituents, the voids freeze 1.5 to 2 times faster than level ice [105] to form the consolidated layer. The consolidated layer is the strongest portion of the ridge, but is approximately 20-30% weaker than level ice. This does not imply that FY ridges are less hazardous than level ice; ridges are many times thicker than level ice and can exert greater loads on structures and vessels (e.g., [20]).

The consolidated layer may be slightly thicker than the level ice or up to three times thicker [107]. During repeat measurements of the same FY ridge the consolidated layer was approximately twice as thick as the surrounding level ice [3]. The thickness of the consolidated layer depends on the measurement technique. Drilling is used to assess the depth of the consolidated layer by noting when the strength of core samples drops and tends to consistently provide higher values since the partially consolidated layer is included. The depth of the consolidated layer may also be determined by checking when the temperature drops below the freezing point of sea water, but this neglects the partially consolidated layer [129].

Apart from being at a higher temperature than the consolidated layer, the partially

consolidated layer is weaker, is comprised of larger ice blocks and has less crushed ice present since the region has undergone lower compressive forces [20]. Voids, when present in the consolidated layer, have been found at the bottom [129], or throughout [132] the layer. Several studies of ridge porosity do not explicitly indicate the porosity of the consolidated layer (e.g., [133], [134]) and it is possible to define the consolidated layer as the region lacking voids (e.g. [8], [133]). For this study the consolidated layer is assumed to be void free.

The thickness of the consolidated layer of a MY ridge was studied over time [3] and data from the study may be found in Table 4.3. The consolidated layer was always approximately two times greater than the level ice thickness and continued to grow even during the melt season. For the purposes of the sea ice model being developed in this research, MY ridges are assumed to be fully consolidated. Salinity increases gradually with depth for the underwater portion of MY ridges.

There is limited quantitative data on the roughness of the top and bottom of the consolidated layer for FY ridges. Simulations on the consolidation process graphically illustrate how the consolidated layer grows over time, but they were based on a specific arrangement of ice blocks and numeric data are not provided on the roughness [135]. Although the bottom of the sail may become consolidated, it is being assumed for this research that the top of the consolidated layer is the level ice surface [20], [107], [133].

Tests conducted on a single FY ridge from late summer to early spring 1998 suggested that the consolidated layer is in the shape of a ‘W’, with the deepest parts of the consolidated layer offset from the location of the peak sail height. Overall, height variations were gentle. The authors concluded that asymmetric snow deposition favoring the leeward side of the ridge limited the growth of the consolidated layer on that side [7]. However, a three-year study of six FY ridges indicated that the thickness of the consolidated layer was highly variable and did not follow a specific pattern.

Variations in consolidated layer thickness were commonly ± 1 m and even ± 2 m over length scales of 5 to 10 m [107]. Similar variations in consolidated layer thickness and variability were reported in [133], however, no details are available explaining how the height variations of the consolidated layer change during the ice season. These variations are assumed to occur exclusively at the bottom of the consolidated layer. Fortunately, the roughness of the bottom of the consolidated layer may be ignored since the high attenuation of saline FY ice (see Section 4.5.6) eliminates any noticeable scatter from the bottom of the consolidated layer.

MY ridges, which are assumed to be fully consolidated, have broader, rectangular keels that contrast with the triangular keels of FY ridges. Keel angles for MY ridges were highly variable and ranged from 0° to 50° [105]. A separate analysis of 85 MY ridge keels using multi-beam sonar also indicated a wide spread in keel angles with an average slope of 25.2° [136]. Apart from the steep keel angles, a study including multiple profiles of a single pressure ridge showed that the keel was massive and ‘bowl-shaped’ [126] and another study indicated the keels were relatively flat [105] and lacking significant depth variations at the bottom of the keel. Thus it is reasonable to ignore the roughness at the bottom of MY keels in the simulations of Chapter 5.

4.3.3 Keel - Unconsolidated Rubble

Below the consolidated layer in FY ridges lies the remainder of the keel. In this region the blocks are not bonded together and are held in place due to buoyancy. Although ridges have irregular shapes, due to isostasy it is possible to estimate the keel depth from the sail height.

Water and slush are often present below the consolidated layer, which will strongly reflect the EM field and there will be limited penetration of the EM field through the ice [132]. Soft ice has also been observed below the consolidated layer [137]. Since soft

ice is believed to form from slush [138], soft ice will still have high water content and it will cause a strong reflection of the EM field. The sea ice model being developed assumes the region below the consolidated layer, the unconsolidated rubble, will not be penetrated by the VHF field due to the presence of liquid water. This assumption is further justified in Section 4.5.3.

New FY ice may grow at the bottom of the MY keel and this will have three potential effects. Firstly, the new ice growth will have high salinity and high water content and field studies have indicated that a strong reflection does not occur at the ice/water boundary where the winter water temperature is assumed to be -1.8°C , but within the ice where the temperature is -2.2°C [9]. This is likely due to the high salinity and water content of the bottom of the ice. For cold FY ice up to 2 m thick this interface is approximately 5 cm from the bottom of the ice [4], but no details have been found on the location of the interface for MY ice. Secondly, the orientation of the new crystal growth will have an impact on the scatter. Under the influence of consistent currents under the ice, the new ice crystals may retain a specific orientation over a large distance. If this orientation is perpendicular to the electric field, the reflection from the ice/water interface may not be visible, despite the low loss through the ice. This effect has been observed during a survey of fast ice [62] and in MY ice trapped in fast ice [116]. Since this study is not limited to fast ice, the impact of ice crystal orientation at the bottom of the ridge will not be included in the simulation. More discussion on orientation effects may be found in Section 4.5.7. A third way new ice growth with a dendritic structure may affect EM scatter is by providing a smooth transition of the dielectric constant from the ice to the water. Since the dendritic layer is only a few centimeters thick, it is not expected to have an impact on VHF scatter [58].

4.4 Profile Measurements

Comprehensive datasets have been collected of sea ice ridges from ice cores examined at small depth increments. Some of these datasets contribute to the development of sea ice ridge models and provide an understanding of how sea ice ridge parameters change over depth. Select studies are briefly discussed in this section to indicate the quality and nature of information available. The data are used for the sea ice ridge models presented in Section 4.6.

CRREL has led numerous field studies on sea ice. In one study ground penetrating radar transects were collected at 80-500 MHz over second year sea ice ridges [4]. At times the high salinity of the ice prevented observation of a distinct reflection from the bottom of the ice and moist regions of the partially consolidated keel also inhibited transmission through the ice. Cores were drilled and each core was analyzed in 10 cm increments of the ice core and sea ice density, salinity and temperature were measured. These measurements were used to calculate the gas volume, brine volume, total porosity, pure ice density, apparent dielectric constant and attenuation. The data indicated no large jumps in ice properties, but the data were surprisingly ordered, as observed in Figure 3.2. A discussion on the relationship between the measured data and physical ridge structure may be found in Section 3.3.

Another CRREL project was conducted June-July 1984 and studied the physical properties of summer sea ice in the Fram Strait [116]. Researchers found that snow depth and sea ice bulk salinity were excellent discriminators of FY and MY ice. Core samples were drilled at 54 different sites and salinity and usually temperature were extracted at 0.1 m intervals. Although the emphasis was on studying undeformed ice, 10 of the 31 cores in MY ice were of ridged ice that were included inadvertently. In one instance a site appeared to be level at the surface, but the core revealed tilted ice blocks indicative of deformed ice. In general the authors concluded that a significant

amount of deformed ice has no surface expression. The mean salinity profile was similar for deformed and undeformed ice, but the variability of the salinity was much greater for deformed ice.

A commercially funded field study was conducted in the southern Beaufort sea in 1971 to study pressure ridges and ice islands [117]. Detailed profiles of salinity, temperature, density and brine volume were collected over one MY ridge. Both density and salinity increased with depth, brine volume increased sharply at the bottom of the ridge and temperature generally declined.

Several CRREL researchers participated in the Canadian Polar Continental Shelf Project in the Northwest Territories where data over three transects of the same MY ridge were collected [126]. The ridge was fully consolidated with all interblock voids filled with ice. Four variables (temperature, salinity, brine volume and density) were measured only for the third transect, which had a ridge height of 3.4 m measured using standard surveying methods and a keel depth estimated at 11.5 m using acoustic measurements, but measurements were only taken to a depth of 3 m. The measured values are consistent with other studies and the high porosity (low density) and near zero salinity at the top of the ridge is prominent.

The National Research Council (NRC) funded a field study of a FY ridge off the west coast of Newfoundland in March 1999 [139]. The ridge was in the process of deteriorating and detailed measurements of two cores from the ridge were taken. The ridge sail height varied from 0.35 to 0.5 m, the consolidated layer thickness ranged from 0.9 to 1.8 m and the total thickness varied between 2.0 to 5.0 m. Both the submergence and mass/volume methods were used to measure density. The average density of the ridge was 0.88 g/cm^3 . Ridge temperature was close to 0°C in the sail and approximately -1.4°C through the rest of the keel. The salinity was under 3‰ in the sail and around 5‰ in the keel.

A number of other studies [8], [65], [129], [132] provide data on the ridge sail, keel and/or consolidated layer. To calculate the relative dielectric constant it is necessary to have data on temperature, salinity and density/macro-porosity and all other parameters may be calculated from these. In some cases calculated brine volume is provided instead of density measurements. Although density may be calculated from brine volume and temperature [140], these data have not been included in this analysis. Warm summer ice that has high macro-porosity and density will not be included in the model since the spaces between blocks are expected to be filled with water and limited penetration of the EM wave is expected. In addition, at temperatures above -5°C , the electrical properties vary more rapidly [141] and pores become connected [128]. Brine pockets also begin to join together [116] and it is more challenging to model the electrical properties of the ice. Densities as high as 0.98 g/cm^3 have been reported for melting ice [132]. The set of studies mentioned in this section is not comprehensive and sometimes certain research is intentionally excluded if any of the key parameters are not provided. The key layers in FY ridges are the sail and the consolidated layer. The layers relevant to MY ridges are the top of the sail, main part of the sail and the keel. Based on the studies reviewed it is possible to summarize the main macroscopic parameters for sea ice ridges that are relevant to scattering from EM frequencies commonly used for penetrating applications. These data may be used to develop a basic model of FY and MY sea ice ridges. In many cases the values presented are estimated from plots and in some cases a range of values is provided. No distinction is made between single ridge measurements and averages over multiple ridges since the objective of listing ice parameters is to show the range of possible values. Studies in which ridge measurements are taken over several months have multiple entries to illustrate how ridge parameters vary over time or specify measurements on different ridges.

Some datasets provide averages over the ridge region and others provide graphical or numerical data through the ridge profile. This information is tabled in the following sections to provide insight on the values and variability of the parameters. Variations in the parameters through each component of the ridge are not explicitly taken into account in the ridge model, however, it was seen in Figure 3.2 that even a large variability in parameters does not result in large reflections of the electric field. Ridge height data have been summarized in Table 4.1 and Table 4.2 and will not be repeated here.

4.4.1 FY Ridge Values

Very few studies measured the density, salinity, macro-porosity and temperature for the sail and consolidated layer for the same FY ridge. In lieu of complete data sets, data have been compiled for each parameter as available. Tables 4.4 to 4.7 summarize the characteristics of FY ridges.

Table 4.4: Summary of FY ridge density measurements

Source	Sail (kg/L)	Consol. Layer (kg/L)	Season
Høyland (2007) [134]	0.86	0.88	May
Høyland (2007) [134]	N/A	0.87 - 0.89	May
Høyland (2007) [134]	0.82	0.85	May

Table 4.5: Summary of FY ridge salinity measurements

Source	Sail (‰)	Consol. Layer (‰)	Season
Høyland and Løset (1999) [7]	0 - 7	3 - 6	April
Høyland (2007) [134]	3.4 - 4.1	4.4	May
Høyland (2007) [134]	N/A	3.5 - 4.2	May
Høyland (2007) [134]	N/A	5.6	May
Høyland (2007) [134]	N/A	4.2	May

Table 4.6: Summary of FY ridge porosity measurements

Source	Sail (%)	Consol. Layer (%)	Season
Høyland (2002)	24	3.4	N/A
Høyland and Løset (1999) [7]	7 - 48	4.8 - 7.9	March
Høyland and Løset (1999) [7]	32.3	2.6	April
Høyland and Løset (1999) [7]	3.3 - 45.3	0 - 6.2	May
Bonath et al. (2018) [107]	0 - 30	N/A	March - April
Leppäranta and Hakala (1992) [8]	19	N/A	March - April
Beketsky et al. (1996) [142]	26	N/A	N/A
Kankaanpää (1989) [143]	20	N/A	March - April
Høyland (2007) [134]	15 - 29	N/A	May
Ervik et al. (2018) [133]	11	N/A	May - June
Strub-Klein and Sudom (2012) [2]	22.1	N/A	N/A

Table 4.7: Summary of FY ridge temperature measurements

Source	Sail (°C)	Consol. Layer (°C)	Season
Hoyland (2002) [129]	-12	-6	March
Hoyland (2002) [129]	-7	-3.5	April
Bonath et al. (2018) [107]	-1 to -3	-2 to -5	March - April
Ervik et al. (2018) [133]	-2 to 0	-2 to -3	May - June

Limited data have been collected detailing how FY ridge parameters change over time. It is known that the keel rubble porosity reduces as the ridge consolidates [133], but quantitative data are not provided on how the sail porosity, salinity and density and consolidated layer salinity change with time, although settling of ice blocks may be the reason sail height reduces over time [3]. General trends as discussed in Section 4.3 will be used to model FY ridge characteristics throughout the ice season.

4.4.2 MY Ridge Values

Several studies of MY ridges included measurements of density, salinity and temperature, providing a complete data set for individual ridges. Tables 4.8 to 4.10 provide examples of relevant MY and second year ridge parameters. Although data collection

was concentrated during the spring months, it is known that salinity remains relatively constant throughout the year for MY ridges [124]. Only ice temperature will vary for the duration being considered in this research.

Table 4.8: Summary of MY ridge density measurements

Source	Sail Top (kg/L)	Sail (kg/L)	Keel (kg/L)	Season
Richter-Menge and Cox (1985) [65]	N/A	0.81	0.88	April
Richter-Menge and Cox (1985) [65]	N/A	0.88	0.90	April
Richter-Menge and Cox (1985) [65]	N/A	0.85	0.89	April
Richter-Menge and Cox (1985) [65]	N/A	0.88	0.89	April
Kovacs et al. (1973) [126]	0.82	0.87 - 0.91	0.86 - 0.91	March
Hnatiuk et al. (1978) [117]	0.84	0.83 - 0.9	0.9 - 0.93	April
Kovacs and Morey (1986) [4]	N/A	0.8 - 0.86	0.8 - 0.89	N/A
Kovacs and Morey (1986) [4]	0.81	0.76 - 0.84	0.84 - 0.92	N/A
Kovacs and Morey (1986) [4]	0.75	0.75 - 0.90	0.85 - 0.91	N/A

Table 4.9: Summary of MY ridge salinity measurements

Source	Sail Top (‰)	Sail (‰)	Keel (‰)	Season
Richter-Menge and Cox (1985) [65]	N/A	0.71	1.56	April
Richter-Menge and Cox (1985) [65]	N/A	0.08	0.89	April
Richter-Menge and Cox (1985) [65]	N/A	0.86	1.66	April
Richter-Menge and Cox (1985) [65]	N/A	1.68	2.68	April
Kovacs et al. (1973) [126]	0	0 - 2	1 - 8	March
Hnatiuk et al. (1978) [117]	0	0 - 1	1 - 4.5	April
Kovacs and Morey (1986) [4]	0	0.2 - 1.4	0.2 - 2.5	N/A
Kovacs and Morey (1986) [4]	0.3	0 - 1.7	2.5 - 3.8	N/A
Kovacs and Morey (1986) [4]	0.6	0.1 - 2.8	2.0 - 4.0	N/A

Table 4.10: Summary of MY ridge temperature measurements

Source	Top of Sail (°C)	Sail (°C)	Keel (°C)	Season
Richter-Menge and Cox (1985) [65]	-20	-20	-20	April
Kovacs et al. (1973) [126]	-21	-21 to -16	-16 to -3	March
Hnatiuk et al. (1978) [117]	-17	-18 to -21	-17 to -1	April
Kovacs and Morey (1986) [4]	-14	-13 to -14	-13 to -2	N/A
Kovacs and Morey (1986) [4]	-6	-7 to -10	-7 to -10	N/A
Kovacs and Morey (1986) [4]	-11	-9 to -11	-6 to -9	N/A

4.5 Modeling Electrical Parameters

Significant research has been conducted to relate the physical properties of sea ice to its electrical properties, namely the complex dielectric permittivity. As discussed previously, sea ice is commonly modeled as a combination of pure ice, brine and gas and the properties of ice and brine are often calculated assuming a Debye model (e.g. [9]), which assumes there is no interaction between particles and the relaxation time is a single value [144]. The permittivity of sea ice may be calculated using a mixture model [145].

The Debye model may be used to calculate the complex, frequency dependent relative permittivity, ϵ_r , of a material as

$$\epsilon_r = \epsilon'_r - j\epsilon''_r = \epsilon_{r\infty} + \frac{\epsilon_{rs} - \epsilon_{r\infty}}{1 + j\omega\tau} - j\frac{\sigma_{DC}}{\omega\epsilon_0}, \quad (4.1)$$

where $\epsilon_{r\infty}$ is the high frequency or optical relative permittivity, ϵ_{rs} is the static relative permittivity, τ is the relaxation time, σ_{DC} is the ionic conductivity for direct current and ϵ'_r and ϵ''_r are the real and imaginary parts, respectively, of the relative dielectric permittivity. In the following sections the subscripts *i*, *br* *sw* and *a* refer to the

quantities pure ice, brine, sea water and air, respectively.

4.5.1 Pure Ice Parameters

For frequencies above 100 MHz the DC conductivity may be ignored for pure ice and $\epsilon_{r\infty,i} = 3.14$. This makes it possible to simplify the Debye equation as [9]:

$$\epsilon_{r,i} = 3.14 + \frac{\epsilon_{rs,i} - 3.14}{1 + j\omega\tau_i}, \quad (4.2)$$

where both $\epsilon_{rs,i}$ and τ_i are a function of temperature, as illustrated in 4.6 and 4.7.

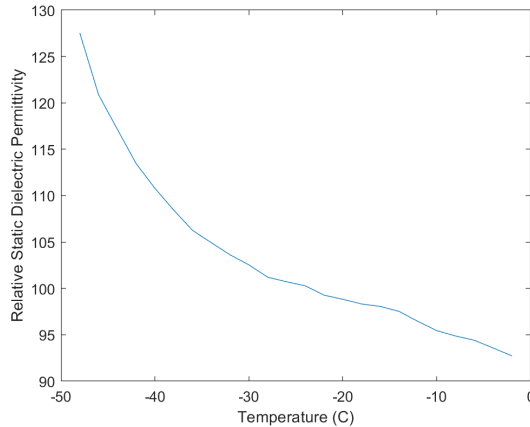


Figure 4.6: Relative static dielectric permittivity for pure ice, from [9]

4.5.2 Brine Parameters

Calculations for brine permittivity are based on the same research as was used for sea water. Research for this work was based on NaCl solutions, which were assumed to be a suitable proxy for sea water since NaCl is the primary salt in sea water [146]. In addition, the empirically derived relationships for $\epsilon_{rs,br}$ and τ_{br} were originally developed for temperatures in the range $0^\circ \leq T \leq 40^\circ$ [147]. Since brine will be in

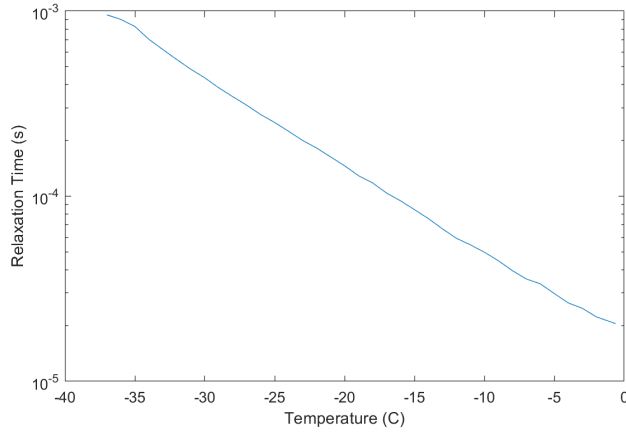


Figure 4.7: Relaxation time for pure ice, from [9]

liquid form, it is reasonable to extrapolate these relationships to freezing temperatures [86].

The parameters in (4.1) for brine are based on [147] in which the data are fitted to polynomial functions. The static limit of the relative permittivity of the brine, $\epsilon_{rs,br}$ is a function of the temperature and normality, N ,

$$\epsilon_{rs,br}(T, N) = \epsilon_{rs,br}(T, 0)[1.000 - 0.2551N + 5.151 \times 10^{-2}N^2 - 6.889 \times 10^{-3}N^3], \quad (4.3)$$

where the normality is a measure of the equivalent concentration and is calculated as the gram equivalent weight of solute per liter of solution. The additional parameters introduced are

$$\epsilon_{rs,br}(T, 0) = 88.22 - 0.4105T + 8 \times 10^{-4}T^2 - 1.0879 \times 10^{-6}T^3, \quad (4.4)$$

and

$$N = S_{br}(1.707 \times 10^{-2} + 1.205 \times 10^{-5}S_{br} + 4.058 \times 10^{-9}S_{br}^2), \quad (4.5)$$

where S_{br} is the brine salinity in the range $0 \leq S_{br} \leq 260$. The brine salinity is a function of temperature, since certain salts begin to precipitate at specific temperatures:

$$\begin{aligned}
S_{br} &= 1.725 - 18.756T - 0.3964T^2, & -8.2^\circ\text{C} \leq T \leq -2^\circ\text{C}, \\
S_{br} &= 57.041 - 9.929T - 0.16204T^2 - 0.002396T^3, & -22.9^\circ\text{C} \leq T \leq -8.2^\circ\text{C}, \\
S_{br} &= 242.94 + 1.5299T + 0.0429T^2, & -36.8^\circ\text{C} \leq T \leq -22.9^\circ\text{C}, \\
S_{br} &= 508.18 + 14.535T + 0.2018T^2, & -43.2^\circ\text{C} \leq T \leq -36.8^\circ\text{C}. \quad (4.6)
\end{aligned}$$

The high frequency limit of the relative brine permittivity was initially believed to be 4.9 [147], but was later determined to be a function of temperature [87] as

$$\epsilon_{r\infty,br} = \frac{82.79 + 8.19T^2}{15.68 + T^2}. \quad (4.7)$$

The relaxation time of the brine, τ_{br} , is also a function of temperature and normality and may be expressed as

$$\tau_{br}(T, N) = \tau_{br}(T, 0)[0.1463 \times 10^{-2}NT + 1.000 - 0.04896N - 0.02967N^2 + 5.644 \times 10^{-3}N^3], \quad (4.8)$$

where

$$\tau_{br}(T, 0) = 17.80 \times 10^{-12} - 0.6032 \times 10^{-12}T + 0.0109 \times 10^{-12}T^2 - 0.0001 \times 10^{-12}T^3. \quad (4.9)$$

The expressions in (4.4) and (4.9) appear in [9] and are specified to be valid over the range $-10^\circ\text{C} \leq T \leq 20^\circ\text{C}$. These expressions are an update from equations in [86] which may be used over the range $0^\circ\text{C} \leq T \leq 40^\circ\text{C}$. For this work the expressions

will be assumed to be valid for $T > -22.9^\circ\text{C}$ so that winter ridge conditions may be modeled.

The DC brine conductivity is a function of temperature and normality and is based on NaCl solutions. It may be expressed with respect to the conductivity at 25°C as

$$\begin{aligned} \sigma_{br}(T, N) = \sigma_{br}(25, N) & [1.000 - 1.962 \times 10^{-2} \Delta + 8.08 \times 10^{-5} \Delta^2 \\ & - \Delta N \{3.020 \times 10^{-5} + 3.922 \times 10^{-5} \Delta + N(1.721 \times 10^{-5} - 6.584 \times 10^{-6} \Delta)\}], \end{aligned} \quad (4.10)$$

where $\Delta = 25 - T$ and

$$\sigma_{br}(25, N) = N[10.394 - 2.3776N + 0.68258N^2 - 0.13538N^3 + 1.0086 \times 10^{-2}N^4]. \quad (4.11)$$

Although the above expressions have been specified for calculating the relative permittivity of brine, they may also be used to estimate the relative permittivity of sea water.

4.5.3 Sea Water Parameters

The water temperature immediately below the ridge may be assumed to be close to the freezing point. Arctic waters are stratified with regards to salinity and the top 50 m has salinity in the range $S_{sw} = 30 - 34\text{‰}$, with lower salinities occurring during the summer due to glacial ice melt [148]. For this analysis the water salinity is taken to be $S_{sw} = 32\text{‰}$, which is lower than salinities found outside the Arctic basin. Water properties are relevant for this study since sea water under the ridge affects the amount of subsurface scatter present.

Knowledge of sea water conductivity, σ_{sw} may be used to determine the skin depth of sea water, δ_{sw} ,

$$\delta_{sw} = \frac{1}{\sqrt{0.5\omega\mu_0\sigma_{sw}}}. \quad (4.12)$$

For sea water at -1.8°C with salinity of 32‰ and EM frequency of 300 MHz, $\delta_{sw} \approx 0.085$ m. Thus, it is reasonable to assume that the EM wave will not penetrate beyond the water or slush commonly found below the consolidated layer.

4.5.4 Proportions of Sea ice Components

As stated previously, sea ice ridge studies often measure density, salinity and temperature and it is possible to estimate the proportions of entrapped gas, brine and pure ice. These proportions are needed to calculate the relative permittivity of the sea ice mixture. Rather than providing the derivations and mathematical definitions of all the terms, this review focuses on the key parameters and how to calculate them. In all cases, the volume proportions are defined as the volume of the component divided by the total volume of the sea ice sample. Although solid salts will have a higher density than ice or brine ($\approx 1500\text{g/cm}^3$), they may be ignored at temperatures above -15.2°C [47]. It has been reported that the presence of solid salts does not impact the mechanical strength of sea ice or the dielectric permittivity in the range from 0.1-40 GHz [111]. For this work solid salts are assumed to have no effect on dielectric permittivity.

Unless otherwise specified, this material is summarized from [140] and is valid for temperatures below -2°C . Alternate equations [149] may be used for warmer ice conditions. The brine volume proportion, V_{br} , may be calculated as

$$V_{br} = \frac{\rho S}{\rho_{br} S_{br}} = \frac{\rho S}{F_1(T)}, \quad (4.13)$$

where ρ is the density of sea ice, S is the sea ice salinity in parts per thousand and ρ_{br} is the brine density. The brine density may be calculated as [150]

$$\begin{aligned} \rho_{br} &= 0.997978 - 0.01658912T - 5.126629 \times 10^{-4}T^2, & -8^\circ\text{C} \leq T < -1.8^\circ\text{C}, \\ \rho_{br} &= 1.024326 - 0.01039362T - 1.307606 \times 10^{-4}T^2, & -32^\circ\text{C} \leq T < -8^\circ\text{C}, \end{aligned} \quad (4.14)$$

and $F_1(T)$ is a polynomial defined as

$$\begin{aligned} F_1(T) &= -4.732 - 22.45T - 0.6397T^2 - 1.074 \times 10^{-2}T^3, & -22.9^\circ\text{C} \leq T \leq -2^\circ\text{C}, \\ F_1(T) &= 9.899 \times 10^3 + 1.309 \times 10^3T^2 + 55.27T^3 + 0.7160T^4, & -30^\circ\text{C} \leq T \leq -22.9^\circ\text{C}. \end{aligned} \quad (4.15)$$

The air volume proportion, V_a , may be calculated as

$$V_a = 1 - \frac{\rho}{\rho_i} + \rho S \frac{F_2(T)}{F_1(T)}. \quad (4.16)$$

The volume proportion of air includes both micro-porosity and macro-porosity. Macro-porosity is often measured during field work, allowing micro-porosity also to be determined using (4.16). The relative permittivity of air or entrapped gas is assumed to be unity.

The density of pure ice may be calculated as

$$\rho_i = 0.917 - 1.403 \times 10^{-4}T. \quad (4.17)$$

The expression for $F_2(T)$ accounts for the volume of solids:

$$\begin{aligned}
 F_2(T) &= 8.903 \times 10^{-2} - 1.763 \times 10^{-2}T - 5.330 \times 10^{-4}T^2 \\
 &\quad - 8.801 \times 10^{-6}T^3, \quad -22.9^\circ\text{C} \leq T \leq -2^\circ\text{C}, \\
 F_2(T) &= 8.547 + 1.089T^2 + 4.518 \times 10^{-2}T^3 + 5.819 \times 10^{-4}T^4, \quad -30^\circ\text{C} \leq T \leq -22.9^\circ\text{C}.
 \end{aligned} \tag{4.18}$$

To calculate the volume proportion of pure ice, V_i , a temperature dependent constant, C , is required which relates the mass of solid salts, m_{ss} to the mass of brine, m_{br} through $m_{ss} = Cm_{br}$, where C is typically provided through a look up table. It is possible to calculate V_i as

$$V_i = \frac{\rho}{\rho_i} - (1 - C) \frac{\rho_{br}}{\rho_i} V_{br}. \tag{4.19}$$

4.5.5 Mixture Model

Several methods have been proposed to calculate the relative permittivity of a mixture of materials. To calculate the permittivity of sea ice due to micro-porosity, mixture models must be invoked twice, first to add air to pure sea ice and secondly to add brine. Since both air and pure ice are low loss materials a simplified equation may be used to account for the air inclusions [4]

$$\epsilon_{r,ia} = (V_a \sqrt{\epsilon_{r,a}} + V_i \sqrt{\epsilon_{r,i}})^2, \tag{4.20}$$

where $\epsilon_{r,ia}$ is the relative permittivity of the brine-free mixture of ice and air. The general mixture model proposed by Tinga et al. (1973) has been used frequently for modeling sea ice [145]. The general form of the expression for the relative permittivity

of the mixture, $\epsilon_{r,m}$, is [86]

$$\epsilon_{r,m} = \epsilon'_{r,m} - j\epsilon''_{r,m} = \epsilon_{r,ia} + \left[\frac{V_{br}\epsilon_{r,ia}(\epsilon_{r,br} - \epsilon_{r,ia})}{n_p(1 - V_{br})(\epsilon_{r,br} - \epsilon_{r,ia}) + \epsilon_{r,ia}} \right], \quad (4.21)$$

where n_p is a depolarization factor that is a function of the orientation of the electric field relative to the sea ice structure. Essentially, it is a measure of how effectively the inclusions may be polarized due to the external field. Empirical studies have shown that for FY sea ice $n_p \approx 0.1$ [9] and for MY ridges $n_p \approx 0.07$ [4]. It should be noted that the Tinga model may only be used when the inclusions are distinct and disconnected. For sea ice above -15°C , brine begins to drain from the ice [6] and brine pockets become connected at temperatures above -5°C [151].

The mixture model must be applied to account a second time for the macro-porosity of FY ridges. A straight forward method has been chosen to estimate the permittivity of the ice due to macro-porosity. The approach combines elements of equations (4.20) and (4.21) in that the permittivity is based on the volume proportions of air and sea ice and the inclusions are assumed to have a specific shape. For this work it has been assumed that the air is present as spherical inclusions in the ice. The expression to calculate, $\epsilon_{r,MP}$, the relative permittivity due to macro-porosity is [152]

$$\epsilon_{r,MP} = \epsilon_{r,m} + V_{MP} \frac{(1 - \epsilon_{r,m}) \left[\frac{2}{3}\epsilon_{r,m} + V_{MP}(1 - \epsilon_{r,m}) \right]}{\frac{2}{3}[\epsilon_{r,m} + (\frac{1}{3} + V_{MP})(1 - \epsilon_{r,m})]}, \quad (4.22)$$

where V_{MP} is the volume fraction of air due to macro-porosity. Macro-porosity is treated as a mixture of sea ice and air instead of individual layers as discussed in Section 4.3.1.

4.5.6 Field Attenuation

Sea ice is a lossy material and the EM field attenuates as it penetrates through the ice. The attenuation may be calculated using the effective conductivity, σ_e , of the ice

$$\sigma_e = \sigma_{DC} + \omega \epsilon''_{r,m} \epsilon_0, \quad (4.23)$$

where σ_{DC} is the DC conductivity of the ice calculated using a form of Archie's rule (e.g., [9]) as

$$\sigma_{DC} = \sigma_{br} (V_{br})^{m_a}, \quad (4.24)$$

where the value of m_a may take on values in the range 1.3 to 4 and depends on the consolidation, pore orientation and geometry and where the brine inclusions are located with respect to the ice crystals. There is a relationship between m_a and the depolarization factor, n_p [153]:

$$m_a = \frac{5 - 3n_p}{3(1 - n_p^2)}. \quad (4.25)$$

Using σ_e it is possible to calculate the real attenuation constant, α , in the standard manner as:

$$\alpha = \omega \left(\frac{\mu_0 \epsilon'_{r,m}}{2} \right)^{1/2} \left[\left(1 + \frac{\sigma_e^2}{\omega^2 (\epsilon'_{r,m})^2} \right)^{1/2} - 1 \right]^{1/2}. \quad (4.26)$$

The field attenuation through the ice is important for understanding whether signals will reflect from the ice/water interface, reflect from other interfaces or be absorbed by the ice.

4.5.7 Isotropy

Sea ice has been described as a lossy and anisotropic material [154]. Growing sea ice typically forms columnar crystals. Anisotropic effects are introduced by the orientation of the incident electric field relative to the orientation of the brine pockets. Currents flowing under landfast ice have been found to align the ice crystals, which also introduces anisotropic effects. It has been observed that when the incident electric field is perpendicular to the alignment of the ice crystals, ground penetrating radar surveys were unable to detect the bottom of the ice, but bottom reflections were visible at other orientations [62]. However, MY ridge properties are isotropic due to deformation [114]. Deformed ice contains a significant portion of frazil and granular ice, which are smaller crystals that are not aligned over large distances. Similarly, first year ridges have been found to have a significant volume of frazil and granular ice [116], especially in the consolidated layer while the sail blocks were composed of columnar ice [139]. It has been noted that columnar portions in ridges may result in anisotropic effects [65], but this potential effect has been ignored since the sail blocks will be placed randomly and a single block will not dominate the scattering behaviour. The electrical properties of sea ice ridges are taken to be isotropic for this study.

4.5.8 Volume Scatter

In general, sea ice backscatter depends on surface roughness, mean dielectric permittivity of the ice, orientation of the ice features, alignment of ice internal structure and volume scatter from inhomogeneities in the ice. Contributions from the first two factors have been discussed in Chapter 2, orientation effects are mitigated at normal incidence, anisotropy may be ignored and the contribution from volume scattering will also be negligible. Simulations have shown that volume scatter will not have any

noticeable impact below 1.2 GHz [86] and that the cross section for an individual air bubble declines rapidly below 4 GHz [155]. It is possible to represent the effect of volume scatter in a simplified manner by using an effective dielectric constant as presented in [156]. This approach was taken for a study that involved impulse radar sounding of sea ice in the frequency bands from 50-250 MHz and 300-1300 MHz [58]. The authors found that modifying the dielectric constant of the ice to account for volume scatter only had an impact at higher frequencies, which are not relevant for this study.

4.5.9 Snow Cover

Like sea ice, snow is a complex material composed of ice crystals, air and liquid water, which may be saline [141]. Snow salinity comes from brine wicked from the the sea ice surface [80]. Snow properties cover a wide range of densities, salinities and moisture contents [157]. Slight changes in the salinity and liquid water content have large impacts on the penetration depth and reflection [141], [158]. Snow-covered ice is warmer, which means that it cannot just be added as an extra layer as the thermodynamic properties of the ice are altered [159].

Both FY and MY ridges will have snow cover, but snow cover is deeper over MY ice since there is greater heat transfer through thinner FY ice resulting in sublimation of snow on FY ice [116]. Snow tends to accumulate on the slopes of ridges, making them appear wider and with a lower slope [1]. Limited snow is present on ridge sail peaks [107], [21], [62], which means that snow will have a limited effect on the scatter from nadir viewing geometry. Previous experiments and modeling with ground penetrating radar have indicated that dry snow has a minor impact on the scattering when using a nadir-pointing radar [58]. In addition, this study is not considering ridges during the melt season so it is reasonable to expect the snow to be dry and

transparent at VHF. For these reasons, this research does not model the impacts of snow over sea ice ridges.

4.6 Sea Ice Ridge Models

Based on the information reviewed, it is possible to develop simple models of sea ice ridges. FY and MY ridge models have been developed with three sets of parameters to correspond with the time periods of fall, mid-winter and early spring. Advanced melt is not included since the ice becomes saturated with melt water and EM field penetration will be limited and the sea ice becomes a matrix of pure ice, water and brine, rendering Tinga's model invalid. These ridge models are used for the simulations of Section 5.5 to determine if there are scattering differences between FY and MY ridges.

There are similarities between the FY and MY ridge data sets previously discussed. Likely due to logistics, studies have been conducted during the spring, when temperatures are still cold and ridges are expected to be strongest. General trends, as discussed in Section 4.3, may be used to estimate how salinity and the thickness of the consolidated layer change throughout the season. Ridge temperature will be constrained by an estimate of air temperature at the top of the sail and the freezing point of sea water at the bottom of the keel. For illustration purposes, average air temperature values will be based on data from Thule, Greenland for October (-9°C), February (-25°C) and April (-16°C) [160]. Average temperatures for the sail will be slightly warmer than these values. Density for the ridge components may be estimated from its porosity since density does not vary significantly with temperature.

In all cases, the layers will be represented by a rough surface and smooth, isotropic, horizontal layers. FY ridges will consist of a sail and consolidated layer and the sail

will consist of two layers. The top of the sail is sea ice with a rough surface defined by the arrangement of ice blocks. There is no macro-porosity in this top layer. The second layer is a mixture of sea ice and air and the proportions of each component are determined by the macro-porosity of the FY sail. MY ridges will also have a rough surface due to differential melt and the horizontal layers will include the top of the sail, the remainder of the sail and the keel. Since only the top layer is considered rough, the roughness is bounded by the thickness of the top layer. This restriction affects the range of ridge roughnesses and geometries that may be simulated. For FY ridges this means that for higher surface roughness, the macro-porosity of the remaining sail ice must be higher. The entire sail is not considered to be a blend of ice and air since the EM field will interact with a solid ice surface and not a blend. For MY ridges the roughness will be bounded by the thickness of the top layer that has very low density. Within these restrictions, it is still possible to model the scattering differences between FY and MY ridges.

Below the surface, all the layers are assumed to be smooth and horizontal. More complex models may allow rough interfaces between layers and random orientation of blocks in the sail to approach the scattering from a statistical perspective. Graphical representations of general FY and MY ridges are given in Figure 4.8. For this research, additional restrictions have been placed on the surface geometry and the ridge models used for this research are illustrated in Figure 4.9. Table 4.11 and Table 4.12 summarize nominal characteristics of FY and MY ridge models, respectively. The parameters specified are not intended to fully characterize FY and MY ridges, but to provide reasonable values that represent the two ice types at various points of the ice season.

Table 4.11: Summary of FY ridge characteristics

	Parameter	Early Fall	Mid-Winter	Early Spring
Sail	Height Variations (m)	0.2 - 1.0	0.2 - .95	0.2 - 0.9
	Height (m)	0.4 - 3.0	0.4 - 3.0	0.4 - 3.0
	Density (kg/L)	0.86 - 0.89	0.85 - 0.88	0.84 - 0.87
	Salinity (‰)	2 - 7	2 - 5.5	2 - 4
	Macro-Porosity (%)	10 - 40	10 - 35	10 - 35
	Temperature (°C)	-7 to -9	-18 to -22.9	-12 to -16
	Block Thickness (m)	0.2 - 0.5	0.2 - 0.5	0.2 - 0.5
	Block Length (m)	0.5 - 2	0.5 - 2	0.5 - 2
Consol. Layer	Depth Variations (m)	0 - 2	0 - 2	0 - 2
	Thickness (m)	0.2 - 0.4	1.4 - 2.5	1.6 - 3
	Density (kg/L)	0.88 - 0.91	0.85 - 0.89	0.85 - 0.89
	Salinity (‰)	4 - 7	3 - 5	3 - 5
	Macro-Porosity (%)	0	0	0
	Temperature (°C)	-5 to -7	-15 to -19	-9 to -13

4.7 Conclusions

A significant portion of this chapter has been devoted to reviewing literature on sea ice and sea ice ridge properties that have relevance for EM scattering in the range 100-500 MHz, frequencies that are often used for penetrating radar applications. One of the objectives of the detailed review is to gain knowledge on the structure and properties of sea ice ridges and understand how they affect the electrical parameters of sea ice ridges and scattering behaviour. Using this knowledge it is possible to develop models that represent the key characteristics of FY and MY sea ice ridges relevant to VHF scattering. FY ridges are modeled as having a sail and consolidated layer and distinct components for MY ridges are the top of the sail, remainder of sail and keel. The key ridge characteristics are the density, salinity and temperature; macro-porosity is also needed for FY sails. These parameters may be used to calculate other physical and electrical parameters of ridges. Although there are differences between sail heights in FY and MY ridges, they are not sufficiently different to reliably differentiate between ice types. The impact on scattering from differences in sea

Table 4.12: Summary of MY ridge characteristics

	Parameter	Early Fall	Mid-Winter	Early Spring
Sail Top	Height Variations (m)	0.2 - 1.0	0.2 - 1.0	0.2 - 1.0
	Height (m)	0.1 - 1.0	0.1 - 1.0	0.1 - 1.0
Sail	Density (kg/L)	0.65 - 0.75	0.65 - 0.75	0.65 - 0.75
	Salinity (‰)	0.0 to 0.25	0.0 to 0.25	0.0 to 0.25
Keel	Height (m)	0.4 - 4.0	0.4 - 4.0	0.4 - 4.0
	Density (kg/L)	0.75 - 0.85	0.75 - 0.85	0.75 - 0.85
	Salinity (‰)	0 - 2	0 - 2	0 - 2
	Temperature (°C)	-7 to -9	-18 to -22.9	-12 to -16
Keel	Depth (m)	1.5 - 8	1.5 - 8	1.5 - 8
	Density	0.86 - 0.91	0.86 - 0.91	0.86 - 0.91
	Salinity (‰)	1 - 3	1 - 3	1 - 3
	Temperature (°C)	-5 to -7	-15 to -19	-9 to -13

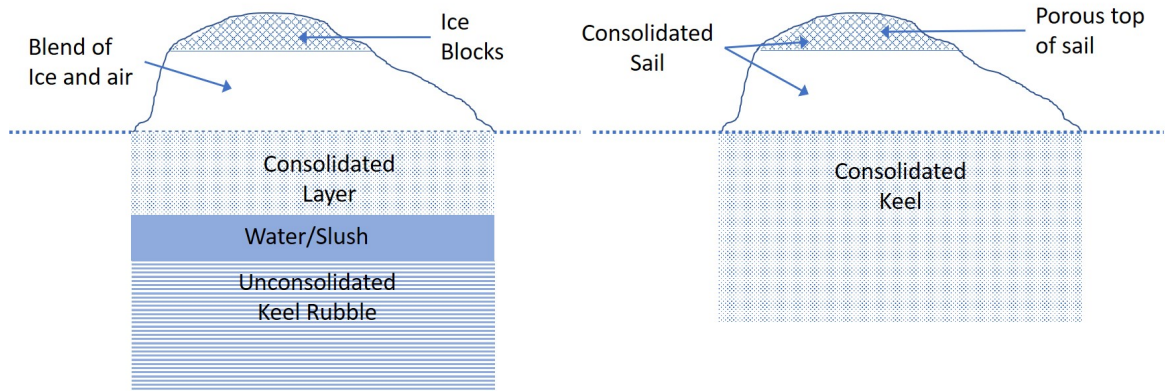


Figure 4.8: General representation of FY (left) and MY (right) sea ice ridges

ice properties, ridge characteristics, EM frequency and ridge age are investigated in Chapter 5.

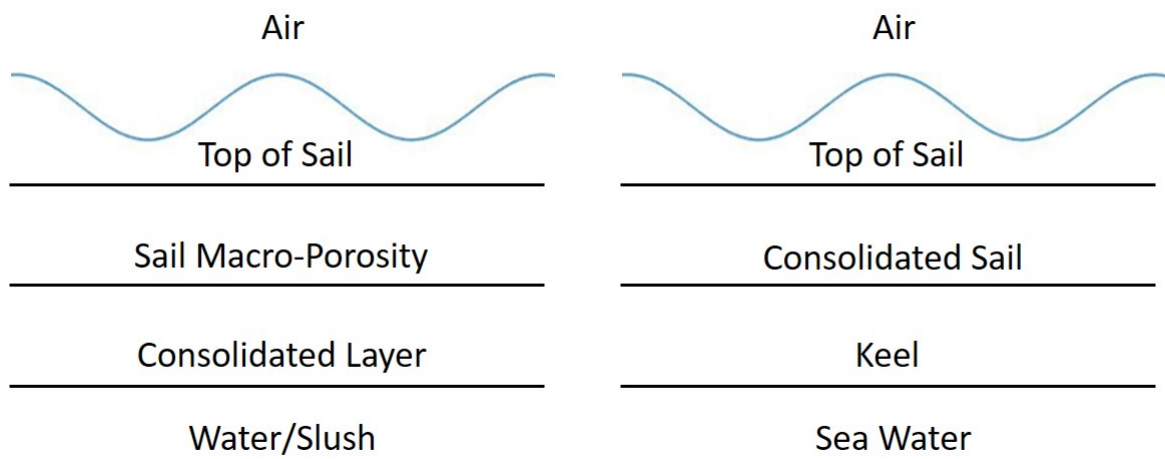


Figure 4.9: Representation of FY (left) and MY (right) sea ice ridges for this research

Chapter 5

Scattering Simulations for First Year and Multi-Year Ridges

5.1 Introduction

The preceding chapters have described the research that makes it possible to compare the scattering behaviour of FY and MY ridges. The scattering models have been updated to accommodate scattering from a rough sea ice surface and a method has been developed to model scattering from a rough surface above stratified media. A sea ice ridge model has also been developed making it possible to model the electrical characteristics of FY and MY ridges. Now it is possible to simulate how the physical characteristics of sea ice affect the scattering signature.

For this analysis, the rough surface is assumed to be a gently varying sinusoid varying in the y direction only. If the equation of the surface profile is known and slowly varying, the scatter from the surface and the layers may be separated spatially. Figure 5.1 is an example of the total co-polarized scatter from a rough surface over layers. The scatter directly from the surface is visible in the off center peaks and

the magnitude of the field scattered from the layered media presents as the central peak at $y = 0$ and at the edges of the plot at $y = \pm 20$ m. Although this trend is visible in both channels, it is more prominently visible in the co-polarized channel. The simulations may be analyzed by comparing the peak values of the surface and subsurface scatter for the co-polarized and cross-polarized channels. These four metrics summarize the scattering characteristics. Since a continuous plane wave source is being assumed instead of a pulsed source, the echoes from the surface and subsurface will be superimposed. The subsurface scatter will not be visible at a certain location unless it exceeds the surface scatter at that point. Thus, the lack of visible subsurface scatter does not mean the absence of subsurface scatter, merely that the subsurface scatter is weaker than the surface scatter at that location.

Since surface roughness, structure and internal characteristics may vary significantly between ridges, the focus of this study is not to simulate the scatter from specific ridges, but to determine if FY and MY ridges exhibit different scattering behavior in general. The chapter has five main sections of simulations. In the first round of simulations the impact of changing a single ice parameter is observed. Secondly, the impacts of changing the EM frequency and the ice surface characteristics are tested. Thirdly, the impact of changing ridge-specific parameters individually is assessed. Next, simulations using the FY and MY ridge models from Section 4.6 are conducted using ice parameters corresponding to three different times of year. Finally, a sensitivity analysis is conducted to determine scenarios in which the scattering signatures of FY and MY ridges may overlap. To simplify comparisons between simulations, the plane wave source will have a magnitude of $E_{0y} = 5\text{V/m}$.

The scattering characteristics of FY and MY ridges will not be compared in a statistical sense for this analysis. This is because the work is completely based on simulations and a number of assumptions were needed to develop the equations. Thus,

only general statements can be made when comparing the scattering characteristics of FY and MY ridges.

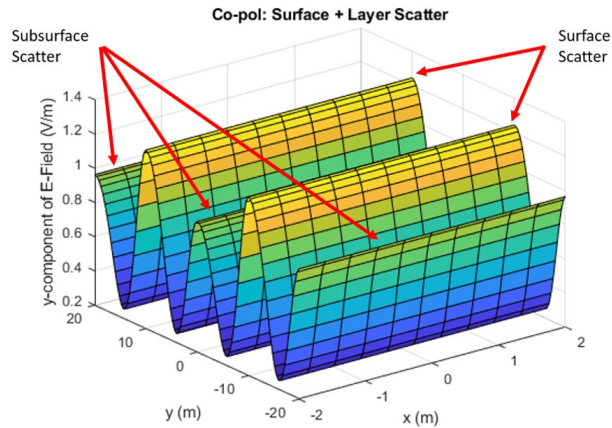


Figure 5.1: Co-polarized and cross-polarized scatter from surface and layers

5.2 Simulations based on Variations of a Single Sea Ice Parameter

This section assesses how changes in sea ice physical parameters impacts the scattered field. To better illustrate the impact of each parameter, only one parameter is changed at a time and only a single layer of ice is considered in this section. Figure 5.2 illustrates the sea ice structure used for this round of the simulations. In the figure a is the amplitude of the sinusoidal surface variation and t is the average ice thickness. To maintain consistency between simulations in this section, the depolarization factor typically found in FY ice will be used.

5.2.1 Impact of Salinity

The salinity of MY ridges is close to zero near the top of the sail (e.g., [4]), remains low for the remainder of the sail and the average salinity remains fairly constant with

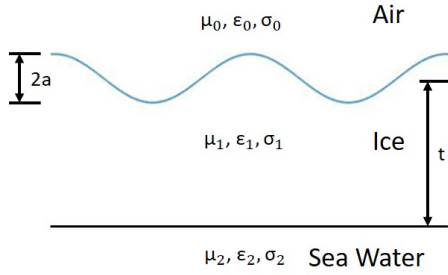


Figure 5.2: Sea ice model for assessing impact of varying a single parameter

depth with salinity around 2‰ (e.g., [124]). FY ridges may have lower salinity in the sail, but typical salinities throughout the ridge are around 3-6‰. Parameters used for simulations of changing salinity are listed in Table 5.1 and simulation results are summarized in Table 5.2. As expected, increasing salinity also results in an increase of the relative permittivity and increased co-polarized surface scatter. For non-saline ice the subsurface scatter is greater than the surface scatter, but quickly drops as salinity rises. Even for low salinity ice (1‰) the subsurface scatter may be buried under the surface scatter, depending on the thickness of the layer. As expected, the cross-polarized channel is much weaker. The cross-polarized surface scatter remains relatively constant and does not vary monotonically as salinity increases, but the cross-polarized subsurface scatter drops significantly as salinity increases. To better illustrate the impact of changing other sea ice and EM source parameters, low salinity ice will be used for simulations in this section. Figure 5.3 plots percentage attenuation of the amplitude of the scattered electric field as a function of salinity and ice thickness. It may be observed in the figure that the field magnitude rapidly decays with increasing salinity and thickness. Attenuation is plotted on a percentage scale instead of the more traditional decibel scale that accommodates a broader dynamic range since even 10 dB attenuation may result in the subsurface scatter being obscured by the surface scatter term.

Table 5.1: Parameters used for testing impact of sea ice salinity on scattering

Parameter	Value(s)
Frequency	300 MHz
Salinity	0-4 ‰
Temperature	-15°C
Density	0.86 kg/L
Ice thickness	3 m
Roughness Height	0.3 m

Table 5.2: Simulations showing impact of sea ice salinity on scattered field

Salinity (‰)	Scattered Field Parameter			
	<i>Co-pol Sfc</i>	<i>Co-pol Sub</i>	<i>Cross-pol Sfc</i>	<i>Cross-pol Sub</i>
0	1.15	2.42	7.9×10^{-2}	0.29
0.25	1.16	1.07	7.2×10^{-2}	0.13
0.5	1.16	0.16	6.7×10^{-2}	1.9×10^{-2}
1	1.18	N/A	6.7×10^{-2}	N/A
2	1.21	N/A	6.9×10^{-2}	N/A
4	1.26	N/A	7.2×10^{-2}	N/A

5.2.2 Impact of Thickness

Although typical sail height for FY and MY ridges is only 0.45 m [1], ridges may be up to tens of meters thick. Parameters used for simulations of different ice thickness are listed in Table 5.3 and simulation results are summarized in Tables 5.4 and 5.5. The co-polarized surface scatter is the same irrespective of the thickness, since the permittivity of the ice is unchanged. The subsurface scatter, for both co-polarized and cross-polarized cases, drops gradually for low salinity as seen in Table 5.4. For the higher salinity results of Table 5.5, the subsurface scatter declines much more rapidly and is quickly lost. As well, the cross-polarized subsurface scatter is lower for highly saline ice. It is apparent that the top layer of the ice must have low salinity for subsurface scatter to take place, or for the ridge to have low height. The presence of visible subsurface scatter in the co-polarized and cross-polarized fields implies low

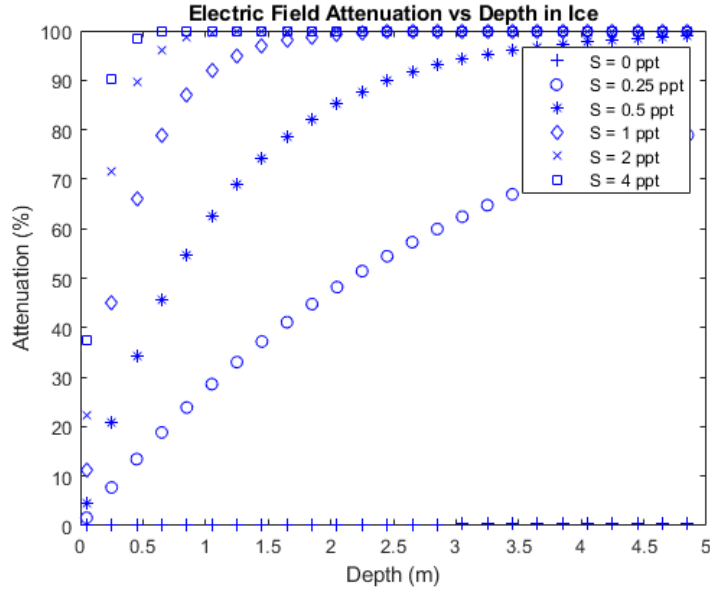


Figure 5.3: Attenuation of 300 MHz EM signal in Sea Ice

salinity ice and is expected to be an important indicator of MY ridges.

Table 5.3: Parameters used for testing impact of sea ice thickness on scattering

Parameter	Value(s)
Frequency	300 MHz
Salinity	0.25, 2 ‰
Temperature	-15°C
Density	0.86 kg/L
Ice thickness	1-6, 0.3-0.8 m
Roughness Height	0.3 m

5.2.3 Impact of Temperature

Ice properties are a function of temperature. For cold air temperatures, a roughly linear temperature profile can be expected through the ridge with the top of the sail similar to the air temperature and the bottom of the consolidated layer at the freezing point of sea water (e.g., [117], [129]). Simulations at varied temperature were conducted based on parameters listed in Table 5.6. Table 5.7 shows that for the co-

Table 5.4: Simulations showing impact of sea ice thickness on scattered field ($S = 0.25\text{‰}$)

Thickness (m)	Scattered Field Parameter			
	<i>Co-pol Sfc</i>	<i>Co-pol Sub</i>	<i>Cross-pol Sfc</i>	<i>Cross-pol Sub</i>
1	1.16	1.85	7.6×10^{-2}	0.22
2	1.16	1.40	7.4×10^{-2}	0.17
3	1.16	1.07	7.2×10^{-2}	0.13
4	1.16	0.81	7.0×10^{-2}	9.7×10^{-2}
5	1.16	0.62	6.9×10^{-2}	7.4×10^{-2}
6	1.16	0.47	6.9×10^{-2}	5.6×10^{-2}

Table 5.5: Simulations showing impact of sea ice thickness on scattered field ($S = 2\text{‰}$)

Thickness (m)	Scattered Field Parameter			
	<i>Co-pol Sfc</i>	<i>Co-pol Sub</i>	<i>Cross-pol Sfc</i>	<i>Cross-pol Sub</i>
0.3	1.21	0.17	7.0×10^{-2}	2.0×10^{-2}
0.4	1.21	7.0×10^{-2}	6.9×10^{-2}	8.3×10^{-3}
0.5	1.21	2.9×10^{-2}	6.9×10^{-2}	3.4×10^{-3}
0.6	1.21	1.3×10^{-2}	6.9×10^{-2}	1.4×10^{-3}
0.7	1.21	N/A	6.9×10^{-2}	N/A
0.8	1.21	N/A	6.9×10^{-2}	N/A

polarized field the surface scatter remains virtually unchanged while the subsurface scatter drops noticeably. The surface and subsurface cross-polarized scatter drops slightly with rising temperature. Over the temperature range tested for low salinity ice, the subsurface scatter was still sufficiently prominent to be clearly identified as low salinity ice.

5.2.4 Impact of Density

Sea ice density is a function of a number of factors including ice temperature, the rate of freezing and the ice age. Generally sea ice keels have higher densities than sea

Table 5.6: Parameters used for testing impact of sea ice temperature on scattering

Parameter	Value(s)
Frequency	300 MHz
Salinity	0.25 ‰
Temperature	-20 to -10°C
Density	0.86 kg/L
Ice thickness	3 m
Roughness Height	0.3 m

Table 5.7: Simulations showing impact of sea ice temperature on scattered field

Temperature (°C)	Scattered Field Parameter			
	<i>Co-pol Sfc</i>	<i>Co-pol Sub</i>	<i>Cross-pol Sfc</i>	<i>Cross-pol Sub</i>
-20	1.16	1.23	7.3×10^{-2}	0.15
-15	1.16	1.07	7.2×10^{-2}	0.13
-10	1.16	0.81	7.1×10^{-2}	9.7×10^{-2}

ice sails due to gravity brine drainage. Melt and melt water flushing in MY ice can result in very low densities in the top of the sail, but the keels of FY and MY sea ice have similar density. Table 5.8 shows the parameter values used for the simulation. Table 5.9 summarizes the simulation results. As density increases, the surface scatter increases for the co-polarized and cross polarized scatter. For the low salinity ice tested, the subsurface scatter remains high and even exceeds the surface scatter for the co-polarized return at lower densities. The surface scatter increases gradually with increasing density as expected since there is more ice present instead of air as density rises and the permittivity of the ice increases. The subsurface scatter decreases for increasing density.

Table 5.8: Parameters used for testing impact of sea ice density on scattering

Parameter	Value(s)
Frequency	300 MHz
Salinity	0.25 ‰
Temperature	-15°C
Density	0.7 to 0.9 kg/L
Ice thickness	3 m
Roughness Height	0.3 m

Table 5.9: Simulations showing impact of sea ice density on scattered field

Density (kg/L)	Scattered Field Parameter			
	<i>Co-pol Sfc</i>	<i>Co-pol Sub</i>	<i>Cross-pol Sfc</i>	<i>Cross-pol Sub</i>
0.70	0.99	1.39	6.4×10^{-2}	0.17
0.75	1.04	1.28	6.7×10^{-2}	0.15
0.80	1.10	1.18	6.9×10^{-2}	0.14
0.85	1.15	1.09	7.1×10^{-2}	0.13
0.90	1.20	1.00	7.4×10^{-2}	0.12

5.3 Simulations based on Variations of a Single Parameter of the Source and Surface

The characteristics of the source and the surface will affect the scattered field and result in differences in the scattered field for FY and MY ridges. Since plane wave incidence is considered, only the EM frequency will be changed. The simple 1D sinusoidal surface will be maintained, but the amplitude and wavelength of the surface will be varied.

5.3.1 Impact of EM Frequency

EM frequency can have a major impact on the scattering from sea ice ridges. The parameters used for checking the impact of EM frequency are given in Table 5.10. The cases of low salinity and moderate salinity ice are considered and results are provided

in Tables 5.11 and 5.12. At lower frequencies it is difficult to separate the surface and subsurface scatter for the cross polarized signal because they overlap and the max value alone will be reported. The max value may be higher due to the superposition of surface and subsurface scatter. These instances are indicated with an asterisk (*). Increasing frequency causes the most significant and consistent changes to the cross polarized scatter. Changing frequency has limited effect on the co-polarized surface scatter and at low salinity the co-polarized subsurface scatter is not monotonic. At moderate salinity levels the subsurface scatter is very low for the values of ice thickness used.

Table 5.10: Parameters used for testing impact of EM frequency on scattering

Parameter	Value(s)
Frequency	100-500 MHz
Salinity	0.25, 2 ‰
Temperature	-15°C
Density	0.86 kg/L
Ice thickness	3 m
Roughness Height	0.3 m

Table 5.11: Impact of EM frequency on scattered field, for $S = 0.25\text{‰}$, $t = 3$ m

Frequency (MHz)	Scattered Field Parameter			
	<i>Co-pol Sfc</i>	<i>Co-pol Sub</i>	<i>Cross-pol Sfc</i>	<i>Cross-pol Sub</i>
100	1.21	1.11	0.22*	0.22*
200	1.16	1.06	0.1	0.15
300	1.16	1.07	7.2×10^{-2}	0.13
400	1.16	1.09	6.1×10^{-2}	0.11
500	1.16	1.11	5.4×10^{-2}	0.11

5.3.2 Impact of Roughness Height

The sea ice model being used [89] has a rough surface over smooth, horizontally layered media. The thickness of the top layer of the ice must be as thick as the

Table 5.12: Impact of EM Frequency on scattered field, for $S = 2\text{‰}$, $t = 0.5$ m

Frequency (MHz)	Scattered Field Parameter			
	<i>Co-pol Sfc</i>	<i>Co-pol Sub</i>	<i>Cross-pol Sfc</i>	<i>Cross-pol Sub</i>
100	1.20*	1.20*	0.12*	0.12*
200	1.21	4.5×10^{-2}	8.4×10^{-2}	7.2×10^{-3}
300	1.21	2.9×10^{-2}	6.9×10^{-2}	3.4×10^{-2}
400	1.21	2.6×10^{-2}	6.0×10^{-2}	2.7×10^{-3}
500	1.21	2.5×10^{-2}	5.4×10^{-2}	2.3×10^{-3}

amplitude of the roughness or else other layers will also have to have rough surfaces as well. The top layer of MY ridges may be as thick as 1 m, but the thickness of the top of FY ridges is determined by the thickness of the ice blocks. Given that block thickness is typically less than 50 cm [64], a full range of roughness heights may not be explored for FY ridges. However, simulations using a single ice layer can illustrate how roughness affects the characteristics of the scattered signal. Table 5.13 specifies the parameters used for the simulations and, as with the other simulations, the roughness height specified refers to the amplitude of the sinusoidal variation. Root mean square (RMS) surface heights are easily calculated as $\sigma_h = a/\sqrt{2}$. As expected, values in Table 5.14 indicated that for scattering at normal incidence, the greatest scatter is for a smooth and level surface. As roughness increases, surface co-polarized scatter decreases, while cross-polarized surface scatter increases. The cross-polarized subsurface scatter shows no discernible trends.

Table 5.13: Parameters used for testing impact of roughness height on scattering

Parameter	Value(s)
Frequency	300 MHz
Salinity	0.25 ‰
Temperature	-15°C
Density	0.86 kg/L
Ice thickness	3 m
Roughness Height	0.2-0.8 m

Table 5.14: Impact of surface roughness height on scattered field, for $S = 0.25\%$

Roughness (m)	Scattered Field Parameter			
	<i>Co-pol Sfc</i>	<i>Co-pol Sub</i>	<i>Cross-pol Sfc</i>	<i>Cross-pol Sub</i>
0.2	1.24	1.15	6.7×10^{-2}	0.11
0.4	1.08	0.99	7.5×10^{-2}	0.14
0.6	0.95	0.87	8.3×10^{-2}	0.14
0.8	0.86	0.78	1.6×10^{-2}	0.14

5.3.3 Impact of Roughness Scale

All the simulations discussed to this point have assumed that the ice surface is represented by a 1D sinusoid with 20 m wavelength. Using a surface variation wavelength that is long with respect to the EM wavelength variation has three main advantages. Firstly, the surface and subsurface scatter appear in distinct locations, which has been discussed in Chapter 3. Secondly, the scatter is proportional to the surface permittivity, which allows the transmitted field to be calculated. For very rough surfaces the scatter will be dominated by the surface roughness [93]. The simulations presented in this section have assumed that the surface correlation length is much larger than the EM wavelength. Finally, the field scattered from the rough surface is assumed to be bandlimited and is expressed in terms of a Neumann series expansion [82], [91]. The expansion will have only one term when $k \leq k_0$. Since the Neumann expansion used here is based on a Fourier series expansion, it is expected that the scattered field will not be accurately represented when there are few terms used.

The parameters for the simulations are given in Table 5.15 and the simulation results are listed in Table 5.16 for low salinity ice. Instances where it is not possible to separate the surface and subsurface scatter will be denoted by an asterisk (*). When λ_s is 5 m, the scattered field is sensitive to small changes in wavelength and the scattering equations are deemed to be unsuitable. Even when $\lambda_s \lesssim 10$ the scattered field has unexpected results both for the low and moderate salinity cases. Further

discussion on the impact of the correlation length on the scattered field may be found in Appendix A.

Table 5.15: Parameters used for testing impact of rough surface wavelength on scattering

Parameter	Value(s)
Frequency	300 MHz
Salinity	0.25‰
Temperature	-15°C
Density	0.86 kg/L
Ice thickness	3 m
Roughness Height	0.3 m
Surface Wavelength	20-7.5 m

Table 5.16: Impact of rough surface wavelength on scattered field, $S = 0.25‰$

Surface λ (m)	Scattered Field Parameter			
	<i>Co-pol Sfc</i>	<i>Co-pol Sub</i>	<i>Cross-pol Sfc</i>	<i>Cross-pol Sub</i>
20	1.16	1.07	7.2×10^{-2}	0.13
15	1.00	0.93	0.14*	0.14*
10	1.06*	1.06*	.23*	.23*
7.5	1.34*	1.34*	0.34*	0.34*

5.4 Simulations based on Variations of Ridge-Specific Parameters

The preceding simulations were based on a single ice layer to illustrate the impacts that radar frequency and sea ice properties have on the scattered field. Sea ice ridge models have been developed to describe the structure and properties of ridges relevant to scattering at VHF and are modeled as shown in Figure 4.8. The figure shows that, in general, ridges will have a rough surface above layers. It is important to note that the field transmitted through the surface is attenuated as it penetrates the ice. The

scattered signal will be further attenuated as it travels back up through the saline ice. The challenge with observing subsurface scatter is that the surface and subsurface scatter terms are superimposed and must compete with each other. Even though peaks in the subsurface scatter occur spatially in troughs of the surface scatter, the subsurface scatter must exceed the surface scatter to be noticed at any given point. This problem may be resolved by using a pulsed source and observing the echoes in time, similar to the operation of a ground penetrating radar.

The next set of simulations will consider the impact of ridge-specific parameters on the scatter. The sail structure of FY ridges, as illustrated in Figure 4.8 will be assessed along with the highly porous low salinity region at the top of the sail for MY ridges. Simulations will be carried out using an EM frequency of 300 MHz. As discussed in Chapter 4, roughness will be ignored at the bottom of the consolidated layer for FY ridges and at the bottom of the keel for MY ridges.

5.4.1 Impact of FY Sail Macro-porosity

To illustrate the impact of macro-porosity, simulations based on the parameters in Table 5.17 will be used. The ‘Sail’ parameters refer to the main body of the sail, which is below the sail blocks that comprise the roughness. Thus, the total sail height is the sum of the top of sail height and sail height in Table 5.17. It may be seen from the simulation results listed in Table 5.18 that the macro-porosity has no noticeable impact on the scattered field, due to the high salinity of the sail blocks.

5.4.2 Impact of Top of MY Sail Thickness

A high concentration of air bubbles is found in the top of the sail of MY ice, which leads to low sea ice density. The depth of that low density and low salinity layer may vary between MY ridges. Table 5.19 lists simulation parameters and Table 5.20 contains

Table 5.17: Parameters for testing impact of FY sail macro-porosity

	Parameter	Value
Sail Top	Height Variations (m)	0.2
	Height (m)	0.2
	Density (kg/L)	0.88
	Salinity (‰)	3
	Temperature (°C)	-15
Sail	Height (m)	0.4
	Density (kg/L)	0.88
	Salinity (‰)	3 (in ice)
	Macro-porosity (%)	10 to 40
	Temperature (°C)	-14
Consol.	Thickness (m)	2
	Density (kg/L)	0.90
	Salinity (‰)	4
	Macro-porosity (%)	0
	Temperature (°C)	-8

Table 5.18: Impact of FY ridge macro-porosity on scattered field

Macro-por. (%)	Scattered Field Parameter			
	<i>Co-pol Sfc</i>	<i>Co-pol Sub</i>	<i>Cross-pol Sfc</i>	<i>Cross-pol Sub</i>
10	1.34	N/A	6.1×10^{-2}	N/A
20	1.34	N/A	6.1×10^{-2}	N/A
30	1.34	N/A	6.1×10^{-2}	N/A
40	1.34	N/A	6.1×10^{-2}	N/A

results that show how the thickness of the top layer of MY ridges affects the scatter. Here the ‘Sail’ height is the total sail height, which remains fixed while the thickness of the top layer of the ice changes for the simulations. The co-polarized surface scatter remains the same since the characteristics of the ice surface were the same for all simulation runs. The subsurface scatter does not monotonically decrease, but this is because of the interplay between the low salinity and thickness of the remaining part of the sail. Simulations run with a higher sail height (results not listed) show a monotonic decrease in co-polarized subsurface scatter. These simulations illustrate that when ice is modeled as a multi-layered structure with a rough surface, it is difficult to predict

the scattering behaviour. Fortunately this does not mean that a comprehensive set of simulations must be conducted covering the full range of parameters that characterize ridges. The scattering signature may not be useful for estimating the characteristics of the top of the sail, but the simulations are consistent with previous results since the subsurface scatter is significant when the salinity of the ice is low. The presence of subsurface scatter contributes to high overall scatter which, thus far, appears to be a reliable discriminator between FY and MY ridges. The following section makes direct comparisons between scattering characteristics of FY and MY ridges.

Table 5.19: Summary of MY ridge characteristics

	Parameter	Value
Sail Top	Height Variations (m)	0.2
	Height (m)	0.2-0.8
	Density (kg/L)	0.7
	Salinity (‰)	0.25
	Temperature (°C)	-15
Sail	Height (m)	1
	Density (kg/L)	0.85
	Salinity (‰)	1
	Temperature (°C)	-14
Keel	Depth(m)	4
	Density	0.88
	Salinity (‰)	2
	Temperature (°C)	-8

Table 5.20: Impact of height of porous layer of MY ridge on scattered field

Porous Lyr (m)	Scattered Field Parameter			
	<i>Co-pol Sfc</i>	<i>Co-pol Sub</i>	<i>Cross-pol Sfc</i>	<i>Cross-pol Sub</i>
0.2	1.07	1.08	6.5×10^{-2}	0.14
0.4	1.07	1.17	6.8×10^{-2}	0.16
0.6	1.07	0.92	6.1×10^{-2}	0.11
0.8	1.07	0.80	5.7×10^{-2}	8.5×10^{-2}

5.5 Scattering Simulations of FY and MY Ridges over Ice Season

A physical representation of FY and MY sea ice ridges is shown in Figure 4.8 and parameters describing the characteristics of ridges from fall to early spring are given in Table 4.11 and 4.12. Nominal values for FY parameters are provided in Table 5.21 and for MY parameters in Table 5.22. Note that some parameters used to describe FY ridges have been omitted from Table 5.21 since they are not explicitly included in specifying ridge characteristics. Results of the simulations are given in Table 5.23.

Table 5.21: Nominal FY ridge characteristics used for simulations

	Parameter	Fall	Mid-Winter	Early Spring
Sail	Height Variations (m)	0.2	0.2	0.2
	Height (m)	0.6	0.6	0.6
	Density (kg/L)	0.87	0.86	0.85
	Salinity (‰)	4	3	2
	Macro-Porosity (%)	30	25	25
	Temperature (°C)	-8	-20	-14
Consol.	Thickness (m)	0.3	2	2.5
	Density (kg/L)	0.89	0.87	0.87
	Salinity (‰)	5.5	4	4
	Temperature (°C)	-5	-11	-8

To this point the simulations have been analyzed under the assumption that the surface and subsurface scatter may be individually identified. This identification is possible due to the assumption of a simple 1D sinusoidal surface geometry. However, during field studies the shape of the roughness profile will not be known *a priori* and the ridge surface will likely not have a sinusoidal profile so, in general, the surface and subsurface scatter may not be spatially separated. Table 5.23 suggests that it may not be necessary to identify surface and subsurface scatter. It may be observed that the co-polarized surface scatter is higher for FY ridges, largely due to the higher

Table 5.22: Nominal MY ridge characteristics used for simulations

	Parameter	Early Fall	Mid-Winter	Early Spring
Sail Top	Height Variations (m)	0.2	0.2	0.2
	Height (m)	0.2	0.2	0.2
	Density (kg/L)	0.7	0.7	0.7
	Salinity (‰)	0.25	0.25	0.25
Sail	Height (m)	0.6	0.6	0.6
	Density (kg/L)	0.8	0.8	0.8
	Salinity (‰)	1	1	1
	Temperature (°C)	-8	-20	-14
Keel	Depth (m)	4	4	4
	Density	0.88	0.88	0.88
	Salinity (‰)	2	2	2
	Temperature (°C)	-5	-11	-8

Table 5.23: Summary of scattering simulations from FY and MY ridges

	Season	Co-pol Sfc	Co-pol Sub	Cross-pol Sfc	Cross-pol Sub
FY	Fall	1.42	N/A	6.5×10^{-2}	N/A
	Winter	1.30	N/A	5.9×10^{-2}	N/A
	Spring	1.28	9.0/e-2	5.9×10^{-2}	6.7×10^{-3}
MY	Fall	1.07	0.52	6.2×10^{-2}	9.2×10^{-2}
	Winter	1.07	1.30	7.0×10^{-2}	0.18
	Spring	1.07	1.17	6.5×10^{-2}	0.15

salinity of the ice. However the co-polarized subsurface scatter is much greater for MY ridges than for FY ridges and the total co-polarized scattered field is greater for MY ridges. These same trends apply to the cross-polarized field. The results of Table 5.20 suggest that the height of the low density layer may cause unusual effects due to the competing effects of attenuation and reflection. However the total cross-polarized scatter remains greater for MY ridges. This suggests that the magnitude of the total co-polarized and cross-polarized scattered field are suitable metrics for distinguishing between FY and MY ridges. Since it is not necessary to be able to separate the surface and subsurface contributions, it should be possible to discriminate between the ridges regardless of the surface profile, provided that the surface maintains gentle roughness.

The results summarized in Table 5.23 are based on nominal characteristics of FY and MY ridges. The next section assesses how changes in ice parameters may affect the ability to discriminate between ice types.

5.6 Factors that Affect Discrimination of FY and MY Ridges

It may be expected during field studies that a pulsed impulse radar system would be used, which would make it possible to isolate the surface and subsurface scatter. For the current analysis using a uniform plane wave, only the scattering magnitude, and possibly the phase, will be available. Thus it is important to identify the factors that affect the total backscatter that may affect the ability to distinguish FY and MY ridges. The greatest scattering difference is noticed in the subsurface scatter so the emphasis is on identifying conditions that increase subsurface scatter in FY ridges and reduce subsurface scatter in MY ridges. The parameter lists of Tables 5.21 and 5.22 will be used as the default parameters, with variations of parameters specified as needed. The lowest subsurface scatter from MY ridges occurs in the fall when temperatures are warmest, so emphasis will be on this time of year. It is expected that the total scatter will drop as temperature increases further, but this will not be tested since the permittivity model being used is not valid for warmer temperatures with interconnected pores. This analysis is a sensitivity analysis to evaluate how deviations from nominal parameters affect the ability to distinguish between FY and MY ridges.

5.6.1 Top of Sail Salinity

The high subsurface scatter in MY ridges is largely due to the low salinity of the top of the ridge. But higher salinity in that layer will have an impact on magnitude of the total scattered field, for both the co-polarized and cross-polarized fields. Table 5.24 shows how higher salinity at the top of the MY sail reduces the subsurface scatter and the overall scatter, as expected. Fortunately the melt/refreeze process indicates that it is very unlikely for high salinities to be present at the top of the sail. In addition, even though the co-polarized scatter has dropped significantly, the total cross-polarized scatter is still stronger than what would be expected for FY ridges.

Table 5.24: Impact of salinity at top of sail for MY ridges, fall parameters

Salinity (‰)	Scattered Field Parameter			
	<i>Co-pol Sfc</i>	<i>Co-pol Sub</i>	<i>Cross-pol Sfc</i>	<i>Cross-pol Sub</i>
0.5	1.09	0.40	5.9×10^{-2}	7.1×10^{-2}
0.75	1.10	0.29	5.7×10^{-2}	5.0×10^{-2}
1	1.11	0.19	5.5×10^{-2}	3.3×10^{-2}

5.6.2 Top of Sail Density

The low density at the top of the ridge has opposing effects on the surface and subsurface co-polarized scatter and there is no noticeable impact on the total scatter, as shown in Table 5.25. The total cross-polarized scatter does not undergo any significant changes and changes in the density of the top of MY ridges does not affect the ability to discriminate between ice types.

5.6.3 Other Parameters

Without conducting additional simulations it is possible to use the results of Sections 5.3 and 5.4 to assess how changes in other parameters affect discrimination potential.

Table 5.25: Impact of density at top of sail for MY ridges, fall parameters

Density (kg/L)	Scattered Field Parameter			
	<i>Co-pol Sfc</i>	<i>Co-pol Sub</i>	<i>Cross-pol Sfc</i>	<i>Cross-pol Sub</i>
0.75	1.13	0.52	6.4×10^{-2}	9.1/e-2
0.80	1.19	0.52	6.7×10^{-2}	9.1/e-2
0.85	1.24	0.53	6.9×10^{-2}	9.0/e-2

Table 5.20 shows that the thickness of the top layer of MY ridges affects the total co-polarized scatter and has almost no impact on the cross-polarized scatter so ice type discrimination is not affected. Table 5.14 shows that as surface roughness height increases, the total co-polarized scatter drops significantly, but the cross-polarized scatter is only nominally affected so there is no net impact on ice type discrimination. This suggests that FY ridges with low roughness height may be distinguished from MY ridges with larger roughness heights.

5.7 Summary and Conclusions

This chapter combines the outcomes of all the previous chapters to generate simulated scattering signatures from sea ice ridge models. The initial simulations are based on a single ice layer and the impacts on the scattered field of varying a single parameter at a time are assessed. Next the impacts of changes in the source frequency and surface roughness are assessed. Using the ridge models developed in Chapter 4 the effects of varying individual ridge-specific parameters are assessed. Again using the ridge models, scatter from FY and MY ridges is simulated for nominal ridge characteristics for fall, winter and early spring and indicates there is a distinct difference between the scattering signatures for FY and MY ridges. The final set of simulations is focused on finding deviations from nominal parameters that affect the ability to discriminate between FY and MY ridges.

Although four metrics were introduced at the start of this chapter, the maximum surface and subsurface scatter for the co-polarized and cross-polarized fields, only the total co-polarized and cross-polarized fields are required. Identifying the surface and subsurface fields is dependent on the rough surface having a simple sinusoidal profile. Removing the reliance on separately identifying the surface and subsurface scatter generalizes the ability to distinguish FY and MY ridges when the surface has a general, but gently varying, profile.

All the ridge parameters evaluated had an impact on the scattered field, but salinity had the greatest impact. The very low salinity characteristically found at the top of MY sails allowed for strong scattering from the subsurface with minimal attenuation resulting in the subsurface scattered field being much stronger for MY ridges than FY ridges, although this effect is mitigated for thicker ice. Although this effect was most noticeable for the co-polarized field, it is also apparent for the cross-polarized field as well. During the sensitivity analysis it was found that the co-polarized field would reduce when the density and thickness of the top layer of the ice increased and the roughness of the surface increased, but the cross-polarized field remained virtually unchanged, which means the discrimination potential was not reduced.

While the salinity of the ice has the greatest impact on the scattered field, surface roughness height also has a significant impact. However, since the cross-polarized field is unaffected as roughness height increases, it may be possible to distinguish between FY and MY ridges when roughness heights are greater than what is accommodated by the analysis presented in Chapters 2 and 3. When the surface correlation length reduces, the strength of the co-polarized and cross-polarized scattered fields increases. In high salinity ice this increases the cross-polarized scatter to levels typically found in low salinity ice, but the co-polarized scatter is much lower for highly saline ice.

Table 5.26: Guide for discriminating between FY and MY ridges

	Co-pol Low	Co-pol High
Cross-pol Low	FY	FY
Cross-pol High	MY	MY

This suggests that when discriminating FY and MY ridges, Table 5.26 may be used as a guide. Specific values are not included since the method used in this study does not include propagation losses and the technique as presented is useful for relative comparisons. It is apparent from Table 5.26 that only the cross-polarized field is needed for discriminating between FY and MY ridges, but the stronger co-polarized field is useful when the cross-polarized field is weak.

Chapter 6

Conclusions

6.1 Summary

The goal of this research is use simulations to determine if it is possible to discriminate between FY and MY ridges using remote sensing data. The simulations operate in the frequency band from 100 to 500 MHz, which is the range frequently used for penetrating radar applications of sea ice and other materials. The scattering has been modeled using analytical methods, to make it easier to generalize the results from the specific simulations conducted. The simulations clearly indicate that FY and MY ridges have distinct scattering signatures, which makes it possible to discriminate between the two ice types.

The research goal was accomplished in three stages. In the first stage radar scattering equations were updated and an approach was developed to model scatter from sea ice ridges. In Chapter 2, Walsh's rough surface scattering equations were updated to be appropriate for EM sounding of sea ice. First, Walsh's assumption of a good conducting surface was removed, making the scattering model suitable for scattering from rough surfaces with a general permittivity. For gently varying surfaces it

was shown that the scattered field is proportional to the index of refraction of the surface. Next, the rough surface scattering model geometry was corrected, removing the implicit assumption of small surface slopes. The shape of the scattered field is modified when the small slope assumption is removed, but the peak scattered field remains unchanged. Expressions for the x -component of the scattered field were also developed to allow the work to be extended to scattering from physically realizable sources such as a horizontal dipole. In Chapter 3 sea ice ridges are presented as a rough surface over stratified media and a simple scattering approach is used in which the total scattered field is the sum of the surface and subsurface scatter. To determine the subsurface scatter the field transmitted through the surface is found using a novel interpretation of Fresnel's law in which the field reflected from a perfect electric conductor was estimated and used to determine the transmitted field. The expression for the field scattered from the layers was simplified and also expressed in terms of scattering coefficients. The expression for the field transmitted through the underside of the rough surface requires a new set of scattering equations, but those equations were shown to be closely related to the original rough surface scattering equations. The general outcome is that a means to model scattering from a rough surface over stratified media was developed.

In the second stage (Chapter 4), models for FY and MY ridges that include the main characteristics of ridges relevant for scattering at VHF were developed using knowledge of trends in sea ice and data collected during field studies of sea ice ridges. Although the physical and mechanical properties of sea ice ridges have been modeled, this is the first time, to the author's knowledge, that ridges have been modeled with respect to their scattering characteristics at VHF. It was found that the main parameters describing sea ice ridges are the salinity, density, porosity and temperature. The structure of FY ridges is defined by the sail and the consolidated layer and the

structure of MY ridges consists of the top of the sail, main part of the sail and the keel. Ranges of parameters for the ridges have been identified for fall through to early spring. The main outcome of this stage are models of FY and MY ridges suitable for modeling scatter at VHF.

The third stage of the research, described in Chapter 5, involves putting the first two stages together to model scattering from sea ice ridges. Before applying the scattering model to sea ice ridges, the impacts of varying a single parameter of sea ice, ridge property or parameter of the surface or source were evaluated. While the scattered field was affected by changes in each parameter, the salinity of the sail had the greatest impact. Due to the simple profile of the surface that was assumed, the surface and subsurface scatter are spatially separated. Simulations using ridge models show that the subsurface scatter is much stronger for MY ridges. The subsurface scatter in MY ridges generally makes the overall scattered field greater for MY ridges, suggesting that MY ridges will have stronger total scattering signatures for other surface geometries as well, provided the surface is not too rough. The main outcomes of this stage are comparisons of scattering for a wide range of sea ice parameters that show that MY ridges may be distinguished from FY ridges on the basis of total scattered field and that this result is applicable for surface profiles other than what was tested.

6.2 Limitations and Assumptions

Earlier in this thesis Walsh's scattering model was described as robust, since it does not require many assumptions to derive the expressions for the scattered field. However, to model the scatter from sea ice ridges a number of additional assumptions were made. Fortunately, it is possible to show that the assumptions are reasonable and

within the scope of the study aims. These assumptions have been described throughout the thesis and are collected in this section for convenience. The assumptions may be separated into three main categories relating to the sea ice ridge model, the scattering mechanisms and the scattering model. Brief descriptions of each assumption and its corresponding justification are outlined below.

6.2.1 Assumptions on Sea Ice Models

To determine the transmitted field, the field scattered from a rough surface is proportional to the refractive index, which means that the surface must not be very rough.

- For FY ridges the surface roughness may be described by the patterns of the ice blocks in the ridge. Individual blocks are smaller than the EM wavelength [64] and will not contribute to the roughness at VHF (see Section 4.3.1).
- Height variations on a ridge will also be moderate [7] (see Section 4.3.1).
- Ridge sails are often modeled as triangles [105] and typically have widths greater than 10 m [2]. The correlation lengths of triangles with these dimensions are several meters (see Section 4.3.1).

Other than the ice ridge surface, the other layers may be considered smooth.

- In FY ridges, the top of the consolidated layer is assumed to correspond with the level ice surface [20] (see Section 4.3.2).
- In FY ridges the bottom of the consolidated layer is rough, but the high salinity of the ice attenuates the EM field sufficiently so that the subsurface scatter is typically buried below the surface scatter making the roughness irrelevant (see Sections 4.5.6 and 4.3.2).

- The bottom of MY keels has been described as ‘bowl’-shaped [126] or rectangular [105] (see Section 4.3.2).

Snow cover may be ignored.

- Dry snow does not interact with EM fields at VHF [58] (see Section 4.5.9).
- Analysis does not include the summer melt season when the EM field interactions with snow may not be ignored (see Chapter 5).

6.2.2 Assumptions on Scattering Mechanisms

The scattered field includes contributions from the rough surface and the stratified media, but volume scatter from the top layer of the MY ridge has not been included.

- Ignoring volume scatter introduces 0.1 dB error for EM frequencies below 1.2 GHz [86] (see Section 4.5.8).
- The EM albedo of a single air bubble drops dramatically at frequencies below 4 GHz [155] (see Section 4.5.8).
- It is possible to account for volume scatter by using a modified permittivity [156], but this had negligible impacts at the frequencies of interest [58] (see Section 4.5.8).

Sea ice ridges have been modeled as being isotropic, although sea ice is generally anisotropic.

- Even though individual ice blocks will be anisotropic, the blocks will be randomly piled up [127] and there will be no net directional effects (see Section 4.5.7).

- The consolidated layer of FY ridges and the bulk of MY ridges are composed of granular ice that has smaller crystals and is isotropic [161] (see Section 4.5.7).

Only one reflection has been considered from the subsurface, but it is possible for the EM field to scatter multiple times from the ice-water interface.

- Multiple scattering will only be noticeable for low salinity ice and the salinity typical in MY ridge keels is sufficient to limit the impact of multiple reflections. The strength of multiple reflections will be low due to the ice salinity and will not affect the ability to discriminate between FY and MY ridges (see Sections 3.4 and 4.5.6).

6.2.3 Assumptions on Scattering Model

The scattered field is assumed to be spatially bandlimited and only the principal solution is found.

- For the EM interrogation geometry and surface profiles with long correlation lengths, the scattered field has been shown to be spatially bandlimited (see Appendix A).

The surface profile is sinusoidal, which is not a realistic representation of sea ice ridges.

- Since the total scattered field may be used to discriminate between FY and MY ridges, the results should not depend on the exact shape of the surface, provided the correlation length of the surface is sufficiently large (See Section 5.5).

6.3 Future Directions

This research has taken Walsh's method in a new direction and there are many ways this current work may be extended. Some ideas of future work are listed below, in the context of the chapter in which additional work is most relevant. Some of these ideas have been listed at the end of each chapter, but they are summarized in this section for convenience.

Chapter 2

- The scattering equations have been updated to be relevant for sea ice, but only when the surface profile is a 1D sinusoid. It would be useful to extend the results to be valid for a random rough surface. Walsh's method has been used to model scattering from random rough surfaces, but only for the scenario of propagation across the surface and not for penetration through the surface.
- The scattering analysis has been conducted for a plane wave at normal incidence. The analysis may be generalized by introducing physically realizable sources, such as pulsed dipoles, at general incidence angles.

Chapter 3

- The forward problem has been considered in this research with a focus on determining the scattering differences between FY and MY ridges. The inverse problem may also be considered where the scattered signal is used to retrieve ridge parameters such as salinity and sail height.
- The analysis has been developed assuming only the top surface is rough. The transmission line method may be used along with Walsh's theory to model the scattering from any number of rough surfaces. Scattering from multiple rough layers has been modeled using the perturbation method and using Walsh's

method in this way would open up new avenues of research with the potential for more accurate modeling of physical phenomena. In the context of the current research, allowing for rough layers would make it possible to model scatter from a greater range of surface roughness since the total roughness does not need to be solely due to the top layer.

Chapter 4

- Modeling sea ice ridge properties has been temporally restricted to avoid the challenging melt season, but the summer months are when Arctic transportation is most frequent and there is the greatest need for discriminating between FY and MY ridges. The sea ice model becomes much more complex during the summer since the EM properties of wet, saline snow must be modeled and the permittivity of sea ice must be determined using a model that accommodates a matrix of interconnected pores. Fortunately, the scattering model can accommodate these changes without any difficulty.

Chapter 5

- The results are based completely on simulations and a natural next step is to collect and analyze field data collections of radar scatter from sea ice ridges. Discrepancies, if any, between the field data and simulation results may be used to refine the sea ice model and question the validity of the assumptions made.

Appendices

Appendix A

Justification for Bandlimited Fields for Gently Varying Surfaces

It was necessary to make several assumptions to develop the scattering equations and apply the scattering model to sea ice ridges. One of the biggest assumptions from the early version of Walsh's approach [82] is that the scattered fields are bandlimited such that $k_x^2 + k_y^2 \leq k^2$. Using the modal form of the solution the requirement that must be satisfied is $k_x^2 + (k_y - qk_0)^2 \leq k^2$. Following this assumption it is possible to find the principal solutions for the scattered field that correspond with low spatial frequencies. One of the assumptions introduced to find the field transmitted through the rough surface is that the surface is only gently varying, which makes the scattered and transmitted fields proportional to the refractive index of the surface.

While Walsh does not provide any justification for the assumption that the scattered field is spatially bandlimited, using the geometry of the problem considered in this research it is possible to show that the assumptions of spatially bandlimited scatter and gently varying surfaces are linked. In fact, for gently varying surfaces it may be shown that the scattered field is spatially bandlimited.

In Section 3.2.1 roughness height, σ_h , and surface correlation length, l_c , are introduced as metrics to describe rough surfaces. Surfaces may be considered to be gently varying if σ_h is low and l_c is large. Figure A.1 illustrates that as the correlation length reduces, the scattered field for $n_1 = 9, \Gamma = -0.8$ is not directly proportional to the field for $n_1 = 3, \Gamma = -0.5$ for all values of q . Although it is not visible in the plots, the scattered fields are not proportionally related to the refractive index for values of q far from the central q , which is $q = 0$ in this case. However, these non-central scattering coefficients are small and have limited impact on the scattered field. The surface for $k_0 = 1.257$ corresponds to a wavelength of 5 m and it may be seen that the scattering coefficients are non-negligible for non-central q .

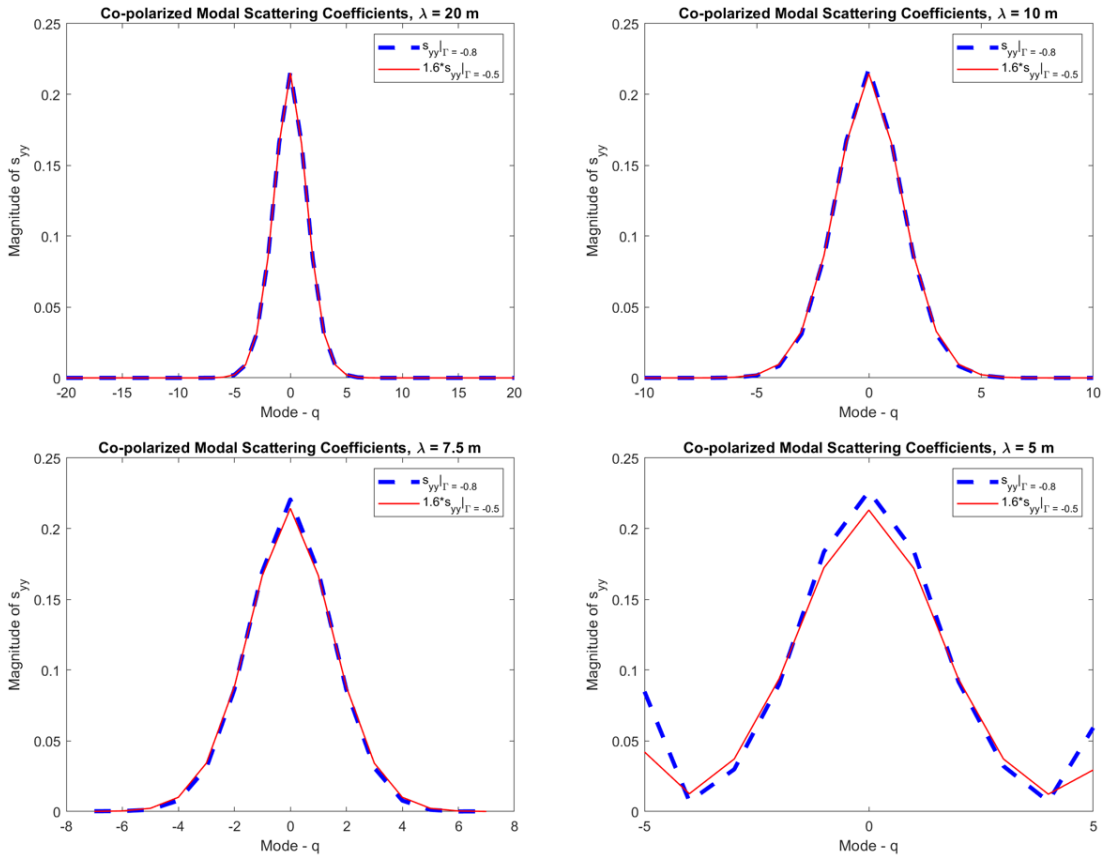


Figure A.1: Scattering coefficients for different correlation lengths

Similarly, the scattered fields are not proportionally related to the surface refractive index as the amplitude of the surface variation increases, as illustrated in Figure A.2. It may be seen that when $a = 1.1$ and $a = 1.4$ the scattering coefficients do not scale accurately for $|q| \approx 0$, but the scaling appears reasonable for lower amplitude values. As expected, since the magnitude of the scattered field will reduce as the amplitude of the surface variation increases, the magnitudes of the scattering coefficients also reduce. It is interesting to note that as the amplitude of the rough surface increases, more of the modal scattering coefficients make a significant contribution to the overall scatter.

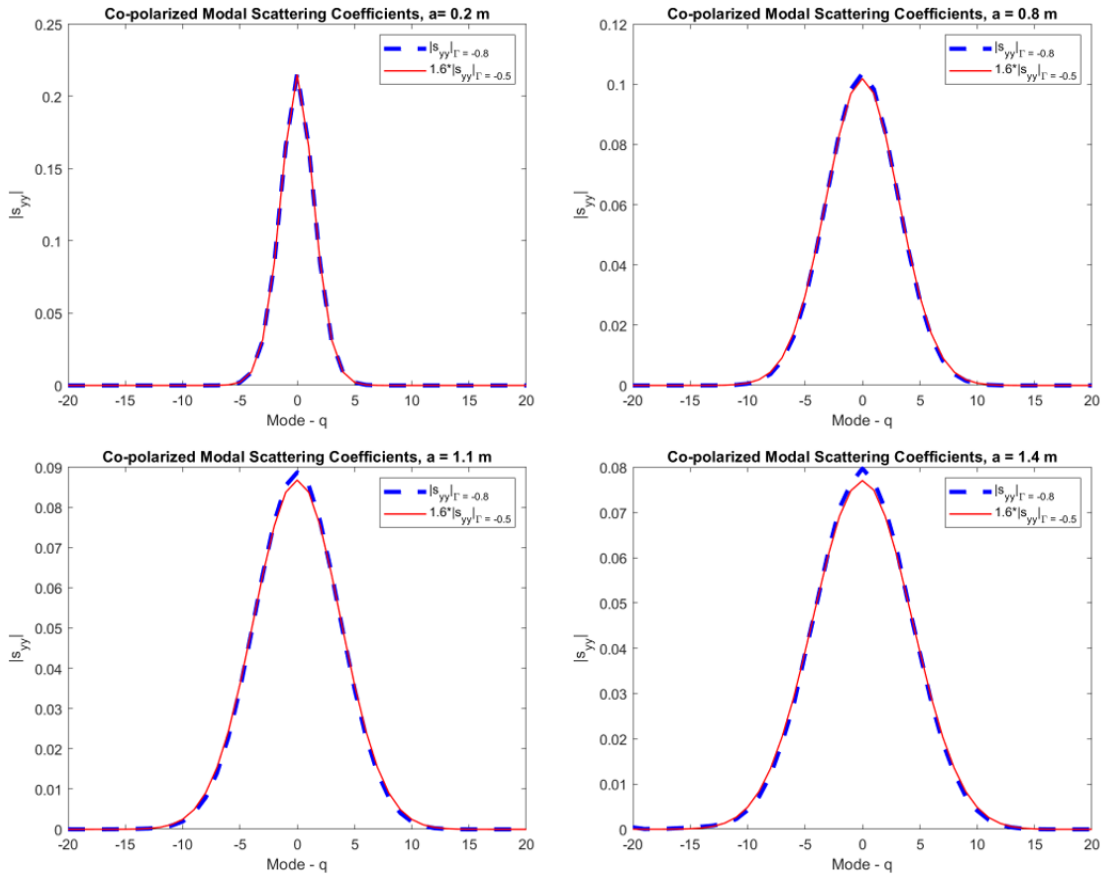


Figure A.2: Rough surface over layers

As the roughness of the surface increases, either by reducing the wavelength or

increasing the amplitude of the surface variation, non-linearities are introduced, but in different ways. As surface wavelength reduces, the scattering coefficients for large $|q|$ become more significant. The scattering coefficients for large $|q|$ are not linearly scalable and once those scattering coefficients become significant it is no longer able to accurately scale the scattering for different surface permittivity. As the surface amplitude increases, the scaling becomes less accurate for the small values of $|q|$ that make the greatest contribution to the scatter. For these reasons, the analysis requires the surface to be gently rough.

The requirement of a gently rough surface also implies that the scattered fields are spatially bandlimited. Consider again the modal criterion that the fields are spatially bandlimited: $k_x^2 + (k_y - qk_0)^2 \leq k^2$. As discussed in Chapter 3, for plane wave incidence $k_x = -k_x^\circ$ and $k_y = -(k_y - qk_0)$. For a surface varying only in the y direction, $k_x^\circ = 0$. It may be seen that large values of $|q|$ must also correspond to large values of k_y° . Since the scattering coefficients for large $|q|$ are negligible, the scattered fields are spatially bandlimited.

Appendix B

Simplification of Layer Scattering as Scattering Coefficients

Chapter 3 describes how the total scatter is the sum of the surface and subsurface scatter. The subsurface scatter involves calculating the field transmitted down through the surface, scattered from the layers and transmitted up through the rough surface in terms of scattering or reflection coefficients. The expression for the field scattered from the layers is

$$\begin{aligned} \underline{E}_y^{z^+} = & \underline{E}_{sy}^{z^+} + e^{-z^+u_0} \left[\frac{u_0 - U_{1h}}{u_0 + U_{1h}} E_{0sy} \right. \\ & \left. - jk_y \frac{2u_0 \frac{1}{n_1^2} \nu_1 + N_{10}}{(u_0 + U_{1h})(u_0 + \frac{1}{n_1^2} U_{1z})} E_{0sz} \right] \end{aligned} \quad (\text{B.1})$$

$$\underline{E}_z^{z^+} = \underline{E}_{sz}^{z^+} + e^{-z^+u_0} \frac{u_0 - \frac{1}{n_1^2} U_{1z}}{u_0 + \frac{1}{n_1^2} U_{1z}}, \quad (\text{B.2})$$

where all variables have already been defined. The z -component of the field is already in the form of a scattering coefficient, but the y -component of the field has

co-polarized and cross-polarized contributions to the field. Recall that the simulations have assumed that the incident plane wave has only a y -component, but the scattering from the rough surface and transmission through the rough surface introduces cross-polarized fields. The text in Section 3.7 indicates that for a dipole source the cross-polarized component of (B.1) is two orders of magnitude smaller than the co-polarized component. The focus of this appendix is to consider the y -component of the scattered field and justify ignoring the cross-polarized term of (B.1) for a plane wave source.

First, it is important to remember that when the source has only a y -component, the z -component of the field scattered from the surface and transmitted through the surface is approximately one order of magnitude smaller than the y -component of the field. This is demonstrated in several places such as the tables of simulation results in Chapter 5 and Figures 2.2, 2.3 and 3.14. This means the z -component of the field transmitted through the surface and incident to the subsurface is much smaller than the y -component of the transmitted field. It also confirms that cross-polarized contributions to the field are much weaker than co-polarized field contributions, again suggesting that the third term of (B.1) will be weak.

Bibliography

- [1] A. A. Petty, M. C. Tsamados, N. T. Kurtz, S. L. Farrell, T. Newman, J. P. Harbeck, D. L. Feltham, and J. A. Richter-Menge, “Characterizing arctic sea ice topography using high-resolution icebridge data,” *The Cryosphere*, 2016.
- [2] L. Strub-Klein and D. Sudom, “A comprehensive analysis of the morphology of first-year sea ice ridges,” *Cold Regions Science and Technology*, vol. 82, no. Supplement C, pp. 94 – 109, 2012.
- [3] M. Leppäranta, M. Lensu, P. Kosloff, and B. Veitch, “The life story of a first-year sea ice ridge,” *Cold Regions Science and Technology*, 1995.
- [4] A. Kovacs and R. M. Morey, “Electromagnetic measurements of multi-year sea ice using impulse radar,” *Cold Regions Science and Technology*, vol. 12, no. 1, pp. 67 – 93, 1986.
- [5] F. Malmgren, “On the properties of sea ice,” in *Scientific Results of the Norwegian North Pole Expedition with the Maud, 1918-1925*, vol. 1a, 1927.
- [6] G. W. Timco and R. M. W. Frederking, “A review of sea ice density,” *Cold Regions Science and Technology*, 1996.

- [7] K. Høyland and S. Løset, “Measurements of temperature distribution, consolidation and morphology of a first-year sea ice ridge,” *Cold Regions Science and Technology*, vol. 29, pp. 59–74, 04 1999.
- [8] M. Leppäranta and R. Hakala, “The structure and strength of first-year ice ridges in the Baltic Sea,” *Cold Regions Science and Technology*, 1992.
- [9] R. M. Morey, A. Kovacs, and G. F. N. Cox, “Electromagnetic properties of sea ice,” *Cold Regions Science and Technology*, vol. 9, no. 1, pp. 53 – 75, 1984.
- [10] R. H. Bourke and R. P. Garrett, “Sea ice thickness distribution in the Arctic Ocean,” *Cold Regions Science and Technology*, vol. 13, no. 3, pp. 259 – 280, 1987.
- [11] D. A. Rothrock, Y. Yu, and G. A. Maykut, “Thinning of the Arctic sea-ice cover,” *Geophysical Research Letters*, vol. 26, no. 23, pp. 3469–3472, 1999.
- [12] L. Pizzolato, S. E. L. Howell, C. Derksen, J. Dawson, and L. Copland, “Changing sea ice conditions and marine transportation activity in Canadian Arctic waters between 1990 and 2012,” *Climatic Change*, vol. 123, no. 2, pp. 161–173, 2014.
- [13] D. G. Barber, G. McCullough, D. Babb, A. S. Komarov, L. M. Candlish, J. V. Lukovich, and S. Rysgaard, “Climate change and ice hazards in the Beaufort Sea,” *Elem Sci Anth*, 2014.
- [14] M. Tedesco, *Remote Sensing of the Cryosphere*. Wiley Blackwell, 2015.
- [15] World Meteorological Organization, “Sea-ice information services in the world,” tech. rep., Secretariat of the World Meteorological Organization, 2006.

- [16] F. Fetterer, C. Fowler, L. M. Ballagh, T. Street, W. N. Meier, and P. Clemente-Colon, "National Ice Center Arctic Sea Ice Charts and Climatologies In Gridded and GIS Format," in *American Geophysical Union Fall Meeting 2006*, 2006.
- [17] S. Sandven, O. M. Johannessen, and K. Kloster, *Encyclopedia of Analytical Chemistry, Edition 6, Volume 6*, ch. Sea Ice Monitoring by Remote Sensing, pp. 1–43. John Wiley and Sons, 2006.
- [18] Canadian Ice Service, "Manual of Ice (MANICE)," tech. rep., Canadian Ice Service, 2005.
- [19] J. Karvonen, M. Similä, and I. Heiler, "Ice Thickness Estimation Using SAR Data and Ice Thickness History," in *IGARSS 2003*, 2003.
- [20] D. Blanchet, "Ice loads from first-year ice ridges and rubble fields," *Canadian Journal of Civil Engineering*, 1997.
- [21] W. F. Weeks, *On Sea Ice*. University of Alaska Press, 2010.
- [22] C. Haas, *Sea Ice*, ch. 2. Sea ice thickness distribution, pp. 42–65. Wiley Blackwell, 2017.
- [23] R. A. Shuchman and D. G. Flett, "SAR Measurement of Sea Ice Parameters: Sea Ice Session Overview Paper," in *Proceedings of the Second Workshop on Coastal and Marine Applications of SAR*, 2003.
- [24] A. Kendrick, "Integration of Polar Classes and Arctic Ice Regime Shipping System," tech. rep., National Research Council, 2005.
- [25] AMSD, "Arctic Ice Regime Shipping System (AIRSS) Standards," tech. rep., Transport Canada, 2018.

- [26] P. Gloersen, W. Nordberg, T. J. Schmugge, T. T. Wilheit, and W. J. Campbell, “Microwave Signatures of First-Year and Multiyear Sea (MANICE),” tech. rep., NASA, 1972.
- [27] I. Zakharov, P. Bobby, D. Power, and S. Warren, “Monitoring extreme ice features using multi-resolution RADARSAT-2 data,” in *2014 IEEE Geoscience and Remote Sensing Symposium*, pp. 3972–3975, July 2014.
- [28] B. O’connell, “Marine radar for improved ice detection,” in *Performance of Ships and Structures in Ice*, 2008.
- [29] S. Sandven and O. M. Johannessen, *Manual of Remote Sensing Volume 3*, ch. 8. Sea Ice Monitoring by Remote Sensing, pp. 1–43. John Wiley and Sons, 1999.
- [30] M. Mäkynen, B. Cheng, and M. Similä, “On the accuracy of thin-ice thickness retrieval using MODIS thermal imagery over Arctic first-year ice,” *Annals of Glaciology*, 2013.
- [31] R. G. Barry, J. Maslanik, K. Steffen, R. L. Weaver, V. Troisi, D. J. Cavalieri, and S. Martin, “Advances in sea-ice research based on remotely sensed passive microwave data,” *Oceanography*, 1993.
- [32] S. Martin, R. Drucker, R. Kwok, and B. Holt, “Estimation of the thin ice thickness and heat flux for the Chukchi Sea Alaskan coast polynya from Special Sensor Microwave/Imager data, 1990–2001,” *Journal of Geophysical Research, C: Oceans*, 2004.
- [33] L. Kaleschke, X. Tian-Kunze, N. Maaß, M. Mäkynen, and M. Drusch, “Sea ice thickness retrieval from SMOS brightness temperatures during the Arctic freeze-up period,” *Geophysical Research Letters*, vol. 39, no. 5, pp. n/a–n/a, 2012. L05501.

- [34] M. B. Rivas, I. Ootosaka, A. Stoffelen, and A. Verhoef, “A scatterometer record of sea ice extents and backscatter: 1992–2016,” *The Cryosphere Discussions*, 2018.
- [35] J. A. Casey, S. E. L. Howell, A. Tivy, and C. Haas, “Separability of sea ice types from wide swath C- and L-band synthetic aperture radar imagery acquired during the melt season,” *Remote Sensing of Environment*, 2016.
- [36] H. Melling, “Detection of features in first-year pack ice by synthetic aperture radar (SAR),” *International Journal of Remote Sensing*, 1998.
- [37] T. Markus, T. Neumann, A. Martino, W. Abdalati, K. Brunt, B. Csatho, S. Farrell, H. Fricker, A. Gardner, D. Harding, M. Jasinski, R. Kwok, L. Magruder, D. Lubin, S. Luthcke, J. Morison, R. Nelson, A. Neuenschwander, S. Palm, S. Popescu, C. Shum, B. E. Schutz, B. Smith, Y. Yang, and J. Zwally, “The Ice, Cloud, and land Elevation Satellite-2 (ICESat-2): Science requirements, concept, and implementation,” *Remote Sensing of Environment*, 2017.
- [38] J. D. Hawkins and M. Lybanon, “GEOSAT Altimeter Sea-Ice Mapping,” *IEEE Journal of Oceanic Engineering*, 1989.
- [39] S. W. Laxon, K. A. Giles, A. L. Ridout, D. J. Wingham, R. Willatt, R. Cullen, R. Kwok, A. Schweiger, J. Zhang, C. Haas, S. Hendricks, R. Krishfield, N. Kurtz, S. Farrell, and M. Davidson, “CryoSat-2 estimates of Arctic sea ice thickness and volume,” *Geophysical Research Letters*, 2013.
- [40] S. Mecklenburg, S. Dransfeld, F. Gascon, J. Nieke, C. Donlon, M. Drusch, D. Schüttemeyer, and B. Berruti, “Esa’s sentinel-3 mission - status and performance,” in *IGARSS 2018*, 2018.

- [41] R. L. Tilling, A. Ridout, and A. Shepherd, "Estimating Arctic sea ice thickness and volume using CryoSat-2 radar altimeter data," *Advances in Space Research*, 2018.
- [42] S. Kern and G. Spreen, "Uncertainties in Antarctic sea-ice thickness retrieval from ICESat," *Annals of Glaciology*, 2015.
- [43] J. Cartwright and C. J. B. adn Meric Srokosz, "Sea ice detection using gnss-r data from techdemosat-1," *Journal of Geophysical Research Oceans*, 2019.
- [44] Q. Yan and W. Huang, "Detecting sea ice from techdemosat-1 using support vector machines with feature selection," *IEEE Journal of Selected Topics in Applied Earth Observation and Remote Sensing*, 2019.
- [45] Q. Yan and W. Huang, "Sea ice concentration estimation from techdemosat-1 data using support vector regression," in *IEEE Radar Conference*, 2019.
- [46] Q. Yan and W. Huang, "Sea ice thickness measurement using spaceborne gnss-r: First results using techdemosat-1 data," *IEEE Journal in Selected Topics in Applied Earth Observation and Remote Sensing*, 2020.
- [47] M. Shokr and N. Sinha, *Sea Ice : Physics and Remote Sensing*. Wiley Interdisciplinary Reviews, 2015.
- [48] M. Studinger, L. Koenig, S. Martin, and J. Sonntag, "Operation Icebridge: Using Instrumented Aircraft to Bridge the Observational Gap between ICESat and ICESat-2," in *2010 IEEE International Geoscience and Remote Sensing Symposium*, 2010.

- [49] M. B. Rivas, J. Maslanik, J. G. Sonntag, and P. Axelrad, "Sea ice roughness from airborne LIDAR profiles," *IEEE Transactions and Geoscience and Remote Sensing*, 2006.
- [50] S. M. Hvidegaard and R. Forsberg, "Sea-ice thickness from airborne laser altimetry over the Arctic Ocean north of Greenland," *Geophysical Research Letters*, 2002.
- [51] A. Pfaffling, C. Haas, and J. E. Reid, "Key characteristics of helicopter electromagnetic sea ice thickness mapping resolution, accuracy and footprint," in *Arctic sea ice thickness: past, present and future*, 2006.
- [52] T. Toyota, *Advances in Geoscience and Remote Sensing*, ch. Application of Remote Sensing to the Estimation of Sea Ice Thickness Distribution. IntechOpen, 2009.
- [53] S. Prinsenbergh and S. Holladay, "Ice thickness measurements with a miniature electromagnetic sensor sled," in *The Nineteenth International Offshore and Polar Engineering Conference*, 2009.
- [54] H. Wakabayashi, T. Matsuoka, K. Nakamura, and F. Nishio, "Polarimetric Characteristics of sea ice in the sea of Okhotsk observed by airborne L-band SAR," *IEEE Transactions on Geoscience and Remote Sensing*, 2004.
- [55] C-CORE, "Multi-year Ice Thickness Distribution in the Beaufort Sea Determined by Airborne Impulse Radar," tech. rep., C-CORE, 1980.
- [56] T. A. Paulley, G. F. Gehrig, and G. A. Oswald, "Measurement of Arctic Sea Ice Using Impulse Radar," in *Offshore Technology Conference*, 1987.

- [57] M. Finke'shteyn and E. I. Lazarev, "A radar video pulse device for measuring the thickness of sea ice as a promising means of ice reconnaissance," tech. rep., USA Cold Regions Research and Engineering Laboratory, 1981.
- [58] B. Holt, P. Kanagaratnam, S. P. Gogineni, V. C. Ramasami, A. Mahoney, and V. Lytle, "Sea ice thickness measurements by ultrawideband penetrating radar: First results," *Cold Regions Science and Technology*, vol. 55, no. 1, pp. 33 – 46, 2009.
- [59] S. A. Proskin, N. S. Parry, and P. Finlay, "Applying GPR in Assessing the Ice Bridges, Ice Roads and Ice Platforms," in *CGU HS Committee on River Ice Processes and the Environment, 16th Workshop on River Ice*, 2011.
- [60] B. Sun, J. Wen, M. He, J. Kang, Y. Luo, and Y. Li, "Sea ice thickness measurement and its underside morphology analysis using radar penetration in the Arctic Ocean," *Science in China*, 2003.
- [61] L. Copland and M. Sharp, "Mapping thermal and hydrological conditions beneath a polythermal glacier with radio-echo sounding," *Journal of Glaciology*, 2001.
- [62] W. Tucker, D. K. Perovich, A. J. Gow, W. F. Weeks, and M. R. Drinkwater, *Physical Properties of Sea Ice Relevant to Remote Sensing*, ch. 2, pp. 9–28. American Geophysical Union, 1992.
- [63] C. Petrich and H. Eicken, *Growth, Structure and Properties of Sea Ice*, ch. 2, pp. 23–77. John Wiley and Sons, 2010.
- [64] W. F. Weeks, A. Kovacs, and I. W. D. Hibler, "Pressure ridge characteristics in the Arctic coastal environment," in *Port and Ocean Engineering under Arctic Conditions*, 1971.

- [65] J. A. Richter-Menge and G. F. N. Cox, "Structure, salinity and density of multi-year sea ice pressure ridges," *J. Energy Resour. Technol.*, vol. 107, no. 4, pp. 493–4967, 1985.
- [66] R. B. Taylor, "The Occurrence of Grounded Ice Ridges and Shore Ice Piling along the Northern Coast of Somerset Island, N. W. T.," *Arctic*, 1978.
- [67] R. R. Parmerter and M. D. Coon, "Model of pressure ridge formation in sea ice," *Journal of Geophysical Research*, vol. 77, no. 33, pp. 6565–6575, 1972.
- [68] S. O. Rice, "Reflection of electromagnetic waves from slightly rough surfaces," *Communications on Pure and Applied Mathematics*, vol. 4, no. 2-3, pp. 351–378, 1951.
- [69] W. Ament, "Forward- and back-scattering from certain rough surfaces," *IRE Transactions on Antennas and Propagation*, 1956.
- [70] K. M. Mitzner, "Effect of small irregularities on electromagnetic scattering from an interface of arbitrary shape," *Journal of Mathematical Physics* 5, 1964.
- [71] W. C. Meecham, "On the Use of the Kirchhoff Approximation for the Solution of Reflection Problems," tech. rep., Office of Naval Research, Navy Department, 1956.
- [72] K. F. Warnick and W. C. Chew, "Numerical simulation methods for rough surface scattering," *Waves in Random Media II*, 2001.
- [73] R. Garg, ed., *Analytical and computational methods in electromagnetics*. Artech House, 2008.

- [74] K. S. Yee, “Numerical solution of initial boundary value problems involving Maxwell’s equations in isotropic media,” *IEEE Trans. Antennas and Propagation*, pp. 302–307, 1966.
- [75] J. R. Wait, “Chapter II - Reflection of Electromagnetic Waves from Horizontally Stratified Media,” in *Electromagnetic Waves in Stratified Media (Revised Edition Including Supplemented Material)* (J. R. Wait, ed.), pp. 8 – 63, Pergamon, 1970.
- [76] T. Tamir, H. C. Wang, and A. A. Oliner, “Wave propagation in sinusoidally stratified dielectric media,” *IEEE Transactions on Microwave Theory and Techniques*, vol. 12, pp. 323–335, May 1964.
- [77] Y. M. Chen, “Wave propagation in stratified random media,” *Radio Science*, 1964.
- [78] R. D. Kubik, *Scattering and depolarization upon transmission across and multiple reflections from irregular multi-layered structures*. PhD thesis, University of Nebraska - Lincoln, 1993.
- [79] P. Imperatore, A. Iodice, and D. Riccio, “Transmission through layered media with rough boundaries: First-order perturbative solution,” *IEEE Transactions on Antennas and Propagation*, 2009.
- [80] A. S. Komarov, L. Shafai, and D. G. Barber, “Electromagnetic wave scattering from rough boundaries interfacing inhomogeneous media and application to snow-covered sea ice,” *Progress in Electromagnetics Research*, 2014.
- [81] X. Duan, *Three-Dimensional Electromagnetic Scattering from Layered Media with Rough Interfaces for Subsurface Radar Remote Sensing*. PhD thesis, University of Michigan, 2012.

- [82] J. Walsh, “On the theory of electromagnetic propagation across a rough surface and calculations in the VHF region,” tech. rep., Memorial University, 1980.
- [83] J. Walsh and R. Donnelly, “A general theory of the interaction of electromagnetic waves with isotropic, horizontally layered media1 (Summary),” *Radio Science*, 1987.
- [84] J. Walsh, “A general theory of the interaction of electromagnetic waves with isotropic, horizontally layered media, and applications to propagation over sea ice,” tech. rep., Memorial University, 1982.
- [85] J. Walsh and S. K. Srivastava, “Rough surface propagation and scatter: 1. General formulation and solution for periodic surfaces,” *Radio Science*, 1987.
- [86] M. R. Vant, R. O. Ramseier, and V. Makios, “The complex-dielectric constant of sea ice at frequencies in the range 0.1–40 ghz,” *Journal of Applied Physics*, 1978.
- [87] A. Stogryn and G. J. Desargant, “The dielectric properties of brine in sea ice at microwave frequencies,” *IEEE Transactions on Antennas and Propagation*, 1985.
- [88] P. Bobby and E. W. Gill, “Modeling radio wave scattering from rough, layered objects,” in *ANTEM*, pp. 465–466, 2018.
- [89] P. Bobby and E. W. Gill, “Modeling scattering differences between sea ice ridges,” in *MTS/IEEE OCEANS Conference 2019*, June 2019.
- [90] P. Bobby, E. W. Gill, and W. Huang, “Modeling vhf scatter from fy and my sea ice ridges,” in *MTS/IEEE OCEANS Conference 2020*, August 2020.

- [91] P. Bobby and E. W. Gill, “Radar scatter from layered media and rough surfaces,” *Progress in Electromagnetics Research C*, vol. 90, pp. 79–93, 2019.
- [92] P. Bobby and E. W. Gill, “Modeling electromagnetic scatter from a rough surface above stratified media - application to sea ice ridges,” *Journal of Oceanic Engineering*, In Press.
- [93] P. Beckmann and A. Spizzichino, *The scattering of electromagnetic waves from rough surfaces*. Pergamon Press, 1963.
- [94] C. V. Saldern, C. Haas, and W. Dierking, “Parameterization of Arctic sea-ice surface roughness for application in ice type classification,” *Annals of Glaciology*, 2006.
- [95] I. Hajnsek and K. Papathanassiou, “Description of natural surfaces.” Prepared for European Space Agency, 2005.
- [96] K. A. Norton and A. C. Omberg, “Maximum range of a radar set,” *Proceedings of the IRE*, 1947.
- [97] D. E. Kerr, “The propagation of short radio waves,” tech. rep., MIT Radiation Lab. Series No. 13, 1951.
- [98] N. Pinel, C. Bourlier, and J. Saillard, “Degree of Roughness of Rough Layers: Extensions of the Rayleigh Roughness Criterion and some Applications,” *Progress in Electromagnetics Research*, 2010.
- [99] P. Wadhams, “A comparison of Sonar and Laser Profiles along Corresponding Tracks in the Arctic Ocean,” in *Sea Ice Processes and Models* (R. S. Pritchard, ed.), 1980.

- [100] I. W. D. Hibler, W. F. Weeks, and S. J. Mock, “Statistical aspects of sea ice ridge distributions,” *Journal of Geophysical Research*, 1972.
- [101] R. T. Lowry and P. Wadhams, “On the statistical distribution of pressure ridges,” *Journal of Geophysical Research*, 1979.
- [102] R. R. Parmeter and M. D. Coon, “On the mechanics of pressure ridge formation in sea ice,” in *Offshore Technology Conference*, 1973.
- [103] Tucker, W. B. III, Sodhi, D. S. and Govoni, J. W., “Structure of first-year pressure ridge sails in the Prudhoe Bay region,” in *The Alaskan Beaufort Sea* (P. W. Barnes, D. M. Schell, and E. Reimnitz, eds.), pp. 115 – 135, Academic Press, 1984.
- [104] I. Kubat, D. Fowler, and M. Sayed, “Chapter 18 - Floating Ice and Ice Pressure Challenge to Ships,” in *Snow and Ice-Related Hazards, Risks and Disasters* (J. F. Shroder, W. Haeberli, and C. Whiteman, eds.), pp. 647 – 676, Boston: Academic Press, 2015.
- [105] G. W. Timco and R. P. Burden, “An analysis of the shapes of sea ice ridges,” *Cold Regions Science and Technology*, 1997.
- [106] T. Martin, “Sea ice ridge modelling: A comparison of approaches in a continuum model,” in *European Geosciences Union, General Assembly*, 2005.
- [107] V. Bonath, C. Petrich, B. Sand, L. Fransson, and A. Cwirzen, “Morphology, internal structure and formation of ice ridges in the sea around Svalbard,” *Cold Regions Science and Technology*, 2018.
- [108] *GeoScan Ground Penetrating Radar*.

- [109] S. Haykin, E. O. Lewis, R. K. Raney, and J. R. Rossiter, *Remote Sensing of Sea Ice and Icebergs*. John Wiley and Sons, 1994.
- [110] D. J. Daniels, *Ground Penetrating Radar, 2nd Edition*, ch. Chapter 3 Modelling Techniques, pp. 37–71. Institution of Engineering and Technology, 2004.
- [111] W. F. Weeks and S. F. Ackley, “The growth, structure and properties of sea ice,” tech. rep., CRREL, Nov. 1982.
- [112] D. V. Divine and C. Dick, “Historical variability of sea ice edge position in the Nordic seas,” *Journal of Geophysical Research, C: Oceans*, vol. III, 2006.
- [113] W. F. Weeks and W. D. H. III, *On Sea Ice*. Fairbanks: University of Alaska Press, 2010.
- [114] G. W. Timco and W. F. Weeks, “A review of the engineering properties of sea ice,” *Cold Regions Science and Technology*, 2010.
- [115] W. B. Tucker III and J. W. Govoni, “Morphological investigations of first-year sea ice pressure ridge sails,” *Cold Regions Science and Technology*, 1981.
- [116] W. B. Tucker III, A. J. Gow and W. F. Weeks, “Physical properties of summer sea ice in the Fram Strait,” *Journal of Geophysical Research: Oceans*, vol. 92, pp. 6787–6803, June 1987.
- [117] J. Hnatiuk, A. Kovacs, and M. Mellor, “A Study of Several Pressure Ridges and Ice Islands in the Canadian Beaufort Sea,” *Journal of Glaciology*, 1978.
- [118] E. C. Hunke, “Thickness sensitivities in the CICE sea ice model,” *Ocean Modelling*, 2010.
- [119] G. W. Timco and K. R. Croasdale, “How well can we predict ice loads,” in *Proceedings of the 18th IAHR International Symposium on Ice*, 2006.

- [120] G. W. Timco and M. Johnston, “Ice loads on the caisson structures in the Canadian Beaufort Sea,” *Cold Regions Science and Technology*, 2004.
- [121] D. Sudom and G. Timco, “Knowledge gaps in sea ice ridge properties,” in *Proceedings of the 22nd International Conference on Port and Ocean Engineering under Arctic Conditions (POAC’13)*, 2013.
- [122] UNESCO, “The practical salinity scale 1978 and the international equation of state of seawater 1980,” tech. rep., UNESCO, 1981.
- [123] E. L. Lewis and R. G. Perkin, “The practical salinity scale 1978: conversion of existing data,” *Deep-Sea Research*, 1981.
- [124] M. Johnston and R. Frederking, “Updated Temperature, Salinity and Strength Distributions for Old Ice (MANICE),” in *ICETECH’11*, 2011.
- [125] M. E. Johnston, “A decade of probing the depths of thick multi-year ice to measure its borehole strength,” *Cold Regions Science and Technology*, 2014.
- [126] A. Kovacs, W. F. Weeks, S. Ackley, and W. D. Hibler, “Structure of a multi-year pressure ridge,” *ARCTIC*, vol. 26, no. 1, 1973.
- [127] R. G. Onstott and R. A. Shuchman, *NOAA SAR User Manual*, ch. Chapter 3. SAR Measurements of Sea Ice, pp. 81–116. NOAA, 2004.
- [128] D. P. Winebrenner, J. Bredow, A. K. Fung, M. R. Drinkwater, S. Nghiem, A. J. Gow, D. K. Perovich, T. C. Grenfell, H. C. Han, J. A. Kong, J. K. Lee, S. Mudaliar, R. G. Onstott, L. Tsang, and R. D. West, *Microwave Remote Sensing of Sea Ice*, ch. Chapter 8. Microwave Sea Ice Signature Modeling, pp. 137–175. American American Geophysical Union, 1992.

- [129] K. V. Høyland, “Consolidation of first-year sea ice ridges,” *Journal of Geophysical Research: Oceans*, vol. 107, no. C6, pp. 15–1–15–16, 2002.
- [130] M. E. Johnston and G. W. Timco, “Guide for understanding and identifying old ice in summer,” in *ICETECH 2008: proceedings of the 8th International Conference and Exhibition on Performance of Ships and Structures in Ice*, 2008.
- [131] D. Sudom, G. Timco, B. Sand, and L. Fransson, “Analysis of first-year and old ice ridge characteristics,” in *Proceedings of the 21st International Conference on Port and Ocean Engineering under Arctic Conditions*, 2011.
- [132] L. Strub-Klein, S. Barrault, H. Goodwin, and S. Gerland, “Physical properties and comparison of first and second year sea ice ridges,” in *Port and Ocean Engineering under Arctic Conditions*, 2009.
- [133] Å. Ervik, K. V. Høland, A. Shestov, and T. S. Nord, “On the decay of first-year ice ridges: Measurements and evolution of rubble macroporosity, ridge drilling resistance and consolidated layer strength,” *Cold Regions Science and Technology*, 2018.
- [134] K. V. Høland, “Morphology and small-scale strength of ridges in the North-western Barents Sea,” *Cold Regions Science and Technology*, 2007.
- [135] A. Marchenko, “Thermodynamic consolidation and melting of sea ice ridges,” *Cold Regions Science and Technology*, 2008.
- [136] P. Wadhams and N. Toberg, “Changing characteristics of Arctic pressure ridges,” *Polar Science*, 2012.

- [137] A. Shestov and A. Marchenko, “Properties of Ice Ridge Keels and Sea Currents in their Vicinity in the Barents Sea,” in *22nd IAHR International Symposium*, 2014.
- [138] A. Marchenko, “Consolidation and melting of sea ice ridges,” in *Proceedings of the 18th IAHR International Symposium*, 2006.
- [139] M. Johnston and A. Barker, “Microstructure of first year sea ice ridges,” tech. rep., National Research Council of Canada, 2000.
- [140] G. F. N. Cox and W. F. Weeks, “Equations for determining the gas and brine volumes in sea-ice samples,” *Journal of Glaciology*, 1983.
- [141] M. Hallikainen and D. P. Winebrenner, *Microwave Remote Sensing of Sea Ice*, ch. Chapter 3. The Physical Basis for Sea Ice Remote Sensing, pp. 29–46. American Geophysical Union, 1992.
- [142] S. P. Beketsky, V. N. Astafiev, and P. A. Truskov, “Structure of Hummocks Offshore of Northern Sakhalin,” in *The Sixth International Offshore and Polar Engineering Conference*, 1996.
- [143] P. Kankaanpää, “Structure of First Year Pressure Ridges in the Baltic Sea,” in *POAC 89; Port and Ocean Engineering under Arctic Conditions*, 1989.
- [144] A. K. Jonscher, “Dielectric relaxation in solids,” *Journal of Physics D: Applied Physics*, 1999.
- [145] W. R. Tinga, W. A. G. Voss, and D. F. Blossey, “Generalized approach to multiphase dielectric mixture theory,” *Journal of Applied Physics*, 1973.
- [146] A. Assur, “Composition of sea ice and its tensile strength,” tech. rep., Cold Regions Research and Engineering Lab, 1960.

- [147] A. Stogryn, "Equations for calculating the dielectric constant of saline water," *IEEE Transactions on Microwave Theory and Techniques*, 1971.
- [148] B. Rudels, *Encyclopedia of Ocean Sciences (Second Edition)*. Academic Academic Press, 2008.
- [149] M. Leppäranta and T. Manninen, "The brine and gas content of sea ice with attention to low salinities and high temperatures," tech. rep., Finnish Institute of Marine Research, 1988.
- [150] G. A. Maykut and B. Light, "Refractive-index measurements in freezing sea-ice and sodium chloride brines," *Applied Optics*, 1995.
- [151] K. Golden, "Bounds on the complex permittivity of sea ice," *Journal of Geophysical Research*, 1995.
- [152] L. K. H. van Beek, "Dielectric behaviour of heterogeneous systems," *Progress in Dielectrics*, 1967.
- [153] P. N. Sen, "Grain shape effects on dielectric and electrical properties of rocks," *Journal of Geophysics*, 1984.
- [154] A. Kovacs and R. M. Morey, "Radar anisotropy of sea ice due to preferred azimuthal orientation of the horizontal c axes of ice crystals," *Journal of Geophysical Research, C: Oceans*, 1978.
- [155] Y.-S. Kim, R. K. Moore, and R. G. Onstott, "Theoretical and experimental study of backscatter from sea ice," tech. rep., Remote Sensing Laboratory, Center for Research Inc. The University of Kansas, 1984.
- [156] J. A. Kong, *Electromagnetic Wave Theory*. John Wiley and Sons, 1986.

- [157] R. J. Galley, M. Trachtenberg, A. Langlois, D. G. Barber, and L. Shafai, “Observations of geophysical and dielectric properties and ground penetrating radar signatures for discrimination of snow, sea ice and freshwater ice thickness,” *Cold Regions Science and Technology*, 2009.
- [158] T. Geldsetzer, A. Langlois, and J. Yackel, “Dielectric properties of brine-wetted snow on first-year sea ice,” *Cold Regions Science and Technology*, 2009.
- [159] I. Merkouriadi, B. Cheng, R. M. Graham, A. Rösel, and M. A. Granskog, “Critical role of snow on sea ice growth in the atlantic sector of the arctic ocean,” *Geophysical Research Letters*, 2017.
- [160] timeanddate.com, “Climate & Weather Averages in Thule Air Base, Greenland.” [Online; Accessed: 2019-06-05].
- [161] E. L. Babcock, J. H. Bradford, and C. Hall, “Electrical anisotropy in sea ice and a dual-polarization radar system to mitigate the effects of preferential attenuation in imaging sea ice,” *Cold Regions Science and Technology*, 2015.